# PLASMONIC NANOMECHANICAL TRANSDUCTION

Cover: experimental structures and setup, drawn by Barthold Thijssen.

Ph. D. thesis, University of Amsterdam, September 2014
*Plasmonic nanomechanical transduction*
Rutger Meijer Timmerman Thijssen

ISBN: 978-90-77209-82-0

A digital version of this thesis can be downloaded from http://www.amolf.nl.

# PLASMONIC NANOMECHANICAL TRANSDUCTION

Gevoelige detectie van beweging met oppervlakteplasmonen

ACADEMISCH PROEFSCHRIFT

ter verkrijging van de graad van doctor
aan de Universiteit van Amsterdam
op gezag van de rector magnificus
prof. D. C. van den Boom,
ten overstaan van een door het college voor promoties ingestelde
commissie, in het openbaar te verdedigen in de Agnietenkapel
op donderdag 4 september 2014, te 10:00 uur

door

RUTGER MEIJER TIMMERMAN THIJSSEN

geboren te New York, Verenigde Staten van Amerika

Promotiecommissie

| | |
|---|---|
| Promotor | prof. dr. A. Polman |
| Copromotores | prof. dr. T. J. Kippenberg |
| | dr. E. Verhagen |
| Overige leden | prof. dr. H. J. Bakker |
| | prof. dr. T. Gregorkiewicz |
| | prof. dr. ir. H. B. van Linden van den Heuvell |
| | prof. dr. M. Orrit |
| | prof. dr. R. Quidant |

Faculteit der Natuurwetenschappen, Wiskunde en Informatica

This work is part of the research program of the 'Stichting voor Fundamenteel Onderzoek der Materie' (FOM), which is financially supported by the 'Nederlandse Organisatie voor Wetenschappelijk Onderzoek' (NWO). This work is also supported by the European Research Council.

# Contents

# 1

# Introduction

Mechanical oscillators have long been used for measurement. Two of the most basic examples are pendulum clocks, for timekeeping, and tuning forks, for measuring frequency. This is possible because of the high mechanical quality factors $Q$ that are attainable, creating stable timekeepers and clean tones. The frequency, amplitude and phase of a mechanical oscillator can be perturbed by coupling to the environment. In some cases, this is an unwanted effect. But it also means that the mechanical oscillator can be used a sensor: detecting forces, displacements, masses and accelerations with high sensitivity. By reading out the state of the mechanical oscillator, these external influences can be detected. Nowadays, mechanical resonators with masses ranging from the $10^{-26}$ kg of a single trapped ion to the kilogram-scale mirrors in gravitational wave detectors are used, with frequencies ranging from ~Hz up to GHz.

To measure small perturbations, using smaller mechanical oscillators is benificial: as their own mass goes down, their susceptibility to perturbing forces increases. It is for this reason that over the past decades micro-electromechanical systems (MEMS) have been scaled down to nano-electromechanical systems (NEMS) [1, 2].

To create a full sensor, it is not enough to have the oscillator sense the environment: its change in oscillation must also be 'transduced' to a measurable signal. The motion of MEMS and NEMS can be transduced using a variety of techniques, for instance capacitively, magnetomotively, or piezoresistively. As the devices become smaller and the measurements more sensitive, the limitations of these electrical readout methods are becoming more and more severe, as electrical noise limits come into play.

Optical transduction has been shown to offer benefits over electrical transduction: quantum-limited optical sources (low-noise lasers) and detection techniques (interferometry) [3] are readily available, allowing new levels of sensitivity.

The most simple detection of motion using light is by reflecting photons from a mechanical oscillator, as sketched in Figure 1.1a. If the oscillator moves by $\delta x$, the phase difference $\delta\phi$ of the reflected beam will be

$$\delta\phi = k \cdot \delta x, \tag{1.1}$$

where $k \equiv \omega/c$ is the light's wavevector. Because the change in position $\delta x$ is typically small compared to the wavelength, the change in phase is also small. A solution is to use a reflecting mechanical oscillator as one of the mirrors in a Fabry-Pérot cavity, as sketched in Figure 1.1b, boosting the phase change by having the photon make multiple passes through the cavity:

$$\delta\phi = \frac{4}{\pi}\mathscr{F}\, k \cdot \delta x, \tag{1.2}$$

where $\mathscr{F}$ is the cavity finesse. The finesse is defined as $\mathscr{F} \equiv \Delta\omega_{\mathrm{FSR}}/\kappa$, with $\Delta\omega_{\mathrm{FSR}} \equiv \pi c/L$ the cavity's free spectral range, where $L$ is the length of the cavity and $\kappa$ is the loss rate. We now introduce the optomechanical frequency shift

$$G \equiv \frac{\partial\omega_c}{\partial x}, \tag{1.3}$$

with $\omega_c$ the cavity resonance frequency. For a Fabry-Pérot cavity, with $G = -\omega_c/L$, we rewrite the phase shift as

$$\delta\phi = 4\frac{G}{\kappa}\delta x, \tag{1.4}$$

expressing the transduced phase change as a change in the cavity resonance frequency.

Because photons carry momentum, they can, besides measuring the position of the mechanical oscillator, also exert a force on the oscillator. This leads to various phenomena that can be discerned in a cavity optomechanical system, such as optical bistability [4], the optical spring effect [5, 6], and optical cooling [7, 8], which can be used to reach thermal occupations close to the quantum regime [9–11].

There are many examples of Fabry-Pérot cavities with movable end mirrors, showing various implementations of the moving mirror: coated cantilevers [8, 12, 13], micropillars [14], mirror pads on cantilevers [15], and photonic crystal slabs [16, 17].

Another implementation is to use internal mechanical modes of deformable guided wave optical cavities, guiding light around the rim of a microdisk [18, 19], microtoroid [11, 20–22], or microsphere [23, 24].

However, for all these systems, the mechanical oscillator is much larger than the (optical) wavelength. Scaling down the oscillator reduces its mass and increases its frequency, which can improve sensitivity. To measure the motion of nanomechanical oscillators, where one or more dimensions of the oscillator are smaller

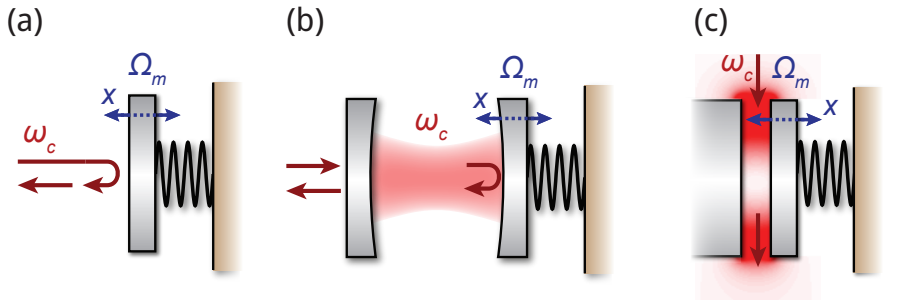


**Figure 1.1:** Schematic of different optomechanical interactions. (a): momentum transfer on reflection, (b): Fabry-Pérot optomechanical cavity, (c): plasmonic metal-insulator-metal cavity.

than the wavelength, such a mechanical oscillator can be introduced into a Fabry-Pérot cavity, modifying the cavity's optical properties either through dispersion [25] or dissipation [26]. One realization is to introduce the mechanical object directly into the (free space) cavity, using for instance silicon nitride (SiN) membranes [25] or carbon nanotubes [27] as mechanical element. Another implementation is to place the mechanical oscillator in the optical near-field of a guided mode optical microresonator, for instance using a SiN string near a microtoroid [28] or two closely spaced microdisk resonators [29–31]. A third approach in this category is to use optically levitated particles as mechanical resonators, allowing very low masses and strongly suppressed clamping losses. This has been shown with micron-sized [32, 33] and submicron [34] silica dielectric particles in an optical dipole trap in a high-vacuum chamber.

These motion-in-a-cavity systems all suffer from the imperfect overlap between the optical and mechanical modes, which leads to modest optomechanical coupling. This modest coupling is compensated by using high-$Q$ optical resonators. Stronger mode overlap, and therefore stronger coupling, can be obtained in photonic crystal cavities. By engineering photonic crystal cavities, the optical and mechanical mode can be co-localized, as has been shown for 1-dimensional [35] and 2-dimensional [36, 37] cavities, which are also known as 'optomechanical crystals'.

Finally, cavity-free implementations have also been demonstrated, with either a deformable waveguide close to a substrate or two waveguides close to each other [38–42], using the strong coupling from exponentially decaying near-fields. One of the advantages of not using a cavity is an increase in optical bandwidth, due to not having a resonant structure. A disadvantage of these systems is that they typically require a long interaction length.

In this work, we will use plasmonic resonances as an optical cavity for the transduction of mechanical motion (Figure 1.1c). As we will show, the near-field confinement in plasmonic structures can be very high, allowing very high coupling

between motion and light while using a subwavelength optical element. We will use multi-element plasmonic resonances, and place at least one element on a mechanical oscillator. Motion of the oscillator then changes the plasmonic configuration, thus changing the optical properties of the cavity.

The small size of plasmonic resonators allows high mode overlap with highly confined mechanical modes. At the same time, the free-space addressability of localized surface plasmon resonances allows the use of simple optical elements to couple light to and from the cavity, without having to resort to for instance nanoscale positioning of tapered optical fibers, as is necessary for many photonic crystal cavity and microcavity optomechanical implementations. The simple addressability also allows parallel transduction of multiple oscillators in a subwavelength area with a single laser beam, which is challenging with many other implementations.

## 1.1 Plasmonics for transduction of motion

In this thesis, we use plasmonics an an intrinsically sub-wavelength optical technique to probe mechanical motion. An interface between a metal and a dielectric supports surface plasmon polaritons, which are evanescent waves that are strongly coupled to coherent oscillations of the free electrons of the metal near the surface.

On a flat interface between a metal and a dielectric (Figure 1.2a), a propagating surface plasmon polariton is supported, with dispersion relation [43]

$$k_x = k_0 \sqrt{\frac{\epsilon \epsilon_m}{\epsilon + \epsilon_m}}, \tag{1.5}$$

where $\epsilon_m$ is the dielectric constant for the surrounding dielectric, $\epsilon$ is the dielectric constant for the metal, and $k_0$ is the free-space wavevector. We express the dielectric constant for the metal using the Drude model for a free-electron gas [44],

$$\epsilon_{\text{Drude}}(\omega) = 1 - \frac{\omega_\text{p}^2}{\omega(\omega + \text{i}\Gamma)}, \tag{1.6}$$

where $\omega_\text{p}$ is the plasma frequency and $\Gamma$ is the damping rate, which is due to electron-electron and electron-phonon scattering.

These surface plasmons are characterized by exponentially decaying optical near-fields extending into the dielectric, making them very sensitive to changes in $\epsilon_m$. By placing a mechanical oscillator in the surface plasmon near-field, we can change the surface plasmon's properties due to the mechanical oscillator's vibrations.

A surface plasmon on a (semi-infinite) surface cannot couple to free space radiation due to the momentum mismatch between $k_0$ and $k_x$. When the surface plasmon geometry is no longer infinite, $k_x$ is not conserved and the plasmon can couple to free space radiation. In a finite-sized system, this creates particle plasmon resonances, of which the most basic is the dipole mode of a metal nanoparticle (Figure 1.2b). For a spherical particle much smaller than the wavelength, the

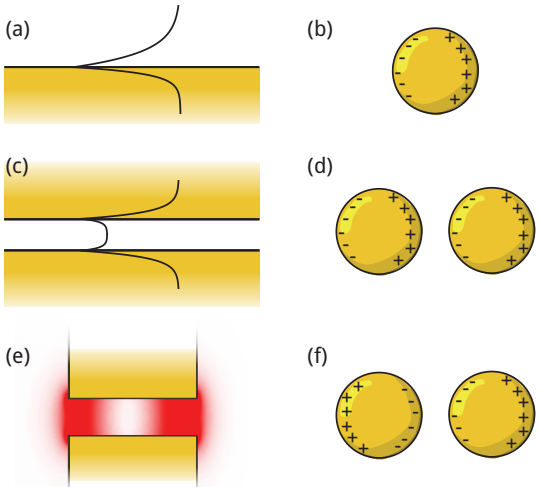


**Figure 1.2:** Sketch of different plasmonic geometries. (a): Metal-insulator surface plasmon mode. (b): Particle plasmon, showing charge distribution. (c): Metal-insulator-metal plasmon modes, showing the symmetric mode profile. (d): Dimer particle plasmon, showing the charge distribution for the bonding mode. (e): Field distribution in a truncated metal-insulator-metal waveguide. (f): Dimer particle plasmon, showing the charge distribution for the anti-bonding mode.

polarizability can be found to be [45]

$$\alpha = 4\pi\epsilon_0 a^3 \frac{\epsilon - \epsilon_m}{\epsilon + 2\epsilon_m}, \tag{1.7}$$

where $a$ is the radius of the particle.

The near-field sensitivity of surface plasmons has found wide application in sensing, both using surface plasmons [46] and particle plasmons [47–50]. The near-field intensity enhancement around particle plasmons has also found other applications, for instance for fluorescence enhancement [51], in higher harmonic generation [52], creating steam [53], or for plasmonic welding [54].

The high field enhancements and high gradients near plasmonic particles lead to strong optical gradient forces [55, 56], leading to the application of plasmonics in trapping dielectric particles, first of micron scale [57], then 100's of nanometer scale [58], and finally particles of 20- [59] and 12-nm diameter [60]. This force enhancement implies that plasmonics could also be used not only for transducing mechanical motion but also to control mechanical motion.

In this thesis, we will use coupled surface plasmons [61] for sensing displacements by displacing two plasmonic elements in each other's near-field. A metal-insulator (MI) plasmon propagating on a surface can be changed to a coupled configuration by bringing a second metal surface into its near-field. This creates a

metal-insulator-metal (MIM) plasmon (Figure 1.2c), whose propagation is strongly dependent on the spacing between the plates [62]. Again, there are two modes, this time usually referred to as the symmetric and antisymmetric mode. While the antisymmetric mode can be tuned to show negative refraction [63], we will focus on the symmetric mode, which has a higher fraction of its field intensity in the dielectric, leading to lower absorption losses in the metal. In Chapters 4 and 5, we study very short MIM waveguides. This creates a more complicated geometry, where reflections from the interfaces between the MIM and the air on both sides play a role, as sketched in Figure 1.2e. This truncation of the MIM then leads to the creation of localized resonances.

In an analogous way, the dipolar particle plasmon resonance can be converted to a coupled mode by placing a second particle nearby, creating a dimer antenna, as sketched in Figure 1.2d and f. Due to the evanescently decaying field around each of these particles, the coupled system is very sensitive to the displacement of the particles along their interparticle axis [64–66]. The individual plasmonic modes of the particles hybridize, forming a bright, dipolar, bonding mode (panel d), and a dark, quadrupolar, antibonding mode (panel f).

Multi-element plasmonic antennas of the basic geometries discussed above have found application in position sensing, using both particle plasmons [67] and metal-insulator-metal waveguides [62].

As discussed earlier, reducing the size of a mechanical oscillator can increase the sensitivity. However, for many (cavity) optomechanical implementations, the mode mismatch between the optical and mechanical modes then leads to a reduction in the transduction efficiency. The small optical mode volume of the plasmonic resonators we study here can improve this: by increasing the mode overlap, good coupling can still be achieved even for the smallest mechanical oscillators, and even with very modest quality factors.

## 1.2 This thesis

In this thesis, we study two types of plasmonic transducers for mechanical motion: metal-insulator-metal plasmonic waveguides between mechanical nanobeams, and dimer antennas with the two elements each placed on separate nanobeams, as shown in Figure 1.3a and b respectively.

In the first geometry, the entire beam is coated in a layer of gold. When measuring in transmission, this creates an intrinsic darkfield geometry, improving the signal-to-noise ratio, though at the cost of increased oscillator mass. These plasmonic transducers will be studied in Chapters 4 and 5. An SEM image of a typical double-beam plasmonic mechanical transducer as studied in Chapter 4 is shown in Figure 1.3a.

In the second, antenna, geometry, we use a plasmonic dimer antenna for transduction of mechanical motion, with Figure 1.3b showing an SEM image of a dimer antenna on a nanobeam. This implementation has the advantage of using far less

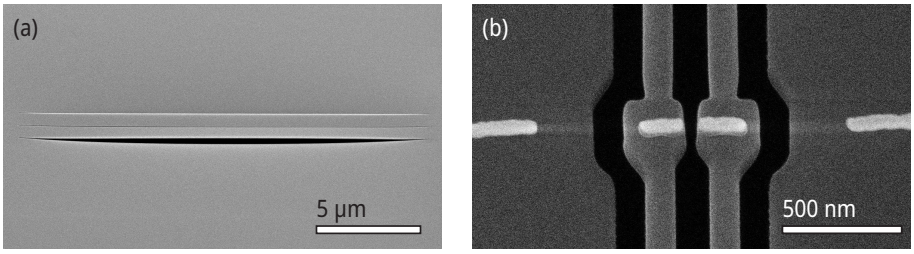


**Figure 1.3:** SEM micrographs of the structures studied in this thesis. (a): Mechanical nanobeams suspended in a $Si_3N_4$ membrane, coated with gold, with a metal-insulator-metal waveguide in the gap between the two beams. (b): Plasmonic coupled dimer antenna on freestanding nanobeams.

metal, allowing for smaller and lighter mechanical oscillators. This geometry will be studied in Chapter 6.

In Chapter 2, we introduce a scattering model to show how plasmonic scatterers transduce mechanical motion to light fields. We also calculate the thermal occupation of mechanical beams using Euler-Bernoulli beam theory. These derivations are used to calculate the attainable measurement sensitivities.

Chapter 3 will discuss the experimental setup to measure plasmonic motion transduction and the fabrication techniques used to create the structures we will study.

# 2

# Principles of plasmonic transduction

In this chapter, we will model the interaction of focused laser beams with plasmonic antennas to determine the experimental observables of scattering and extinction. More importantly in the context of motion transduction, we will determine the *change* in scattering and extinction with changes in mechanical configuration. Therefore, it is logical to use a scattering model to describe the interaction of light and matter.

First, we review the mechanical portion of our plasmo-mechanical transducer, using Euler-Bernoulli theory to derive expressions for the eigenfrequencies and mode-shapes of the doubly clamped beams in our experimental structures. We then use the fluctuation-dissipation theorem to describe the thermal displacement fluctuations of the mechanical modes.

Next, we determine the polarizability $\alpha$ of two coupled dipoles and discuss the radiation corrections to the electrostatic model. We then determine $\mathrm{Im}(\alpha)$ and $|\alpha|^2$, with which extinction and scattering, respectively, are proportional, and find expressions for the change in $\mathrm{Im}(\alpha)$ and $|\alpha|^2$ with changes $\delta x$ in mechanical configuration. We study the interaction of such a system with a focused laser beam, to find the transmittance,

$$\mathcal{T} \equiv \frac{P_{\mathrm{out}}}{P_{\mathrm{in}}}, \tag{2.1}$$

with $P_{\mathrm{in}}$ the input power and $P_{\mathrm{out}}$ the transmitted power. From $\mathcal{T}$ and the dependence of $\mathrm{Im}(\alpha)$ and $|\alpha|^2$ on changes $\delta x$ we will determine the change in transmittance $\frac{\partial \mathcal{T}}{\partial x}$. We include input- and output polarizers in this model, which we will use to study a crossed-polarizer geometry, which for some scattering parameters can be used to improve signal-to-noise ratios.

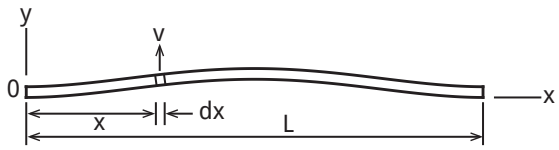


**Figure 2.1:** Sketch of beam geometry indicating relevant parameters. $L$: beam length, $v(x)$: displacement.

We illustrate the attainable measurement sensitivity with this plasmonic transduction scheme by considering two systems with mechanical properties that have been demonstrated by other groups. We also adapt this model to study transduction of motion by plasmonic metal-insulator-metal geometries and compare this to motion transduction by a geometric shadow geometry, which is relevant for the experimental structures studied in Chapters 4 and 5.

## 2.1 Mechanical modes of doubly clamped beams

In this thesis, the mechanical modes we study are those of silicon nitride beams, sometimes coated with a layer of metal. These beams have a large ratio of thickness in the direction of motion to length, such that we have to take their flexural stiffness into account [68, 69]. For the boundary conditions we assume that the beams are doubly clamped: the endpoints are constrained to have no displacement and no bending*. In the following, we will discuss the mechanical modes of these systems. We will derive the eigenfrequencies for beams governed by flexural stiffness, and show the modifications to include tensile stress and bilayer beams.

Following the derivation by Weaver, Timoshenko and Young [69], we start from the equation of motion for a beam:

$$\frac{\partial^2 v}{\partial x^2}\left(EI\frac{\partial^2 v}{\partial x^2}\right) = -\rho A\frac{\partial^2 v}{\partial t^2}, \tag{2.2}$$

with displacement $v(x,t)$, Young's modulus $E$, moment of inertia $I$, mass density $\rho$ and cross section $A = w \times h$. If the beam is prismatic, i.e. has a constant cross section along its length, Young's modulus and moment of inertia are independent of $x$, reducing the equation to

$$EI\frac{\partial^4 v}{\partial x^4} = -\rho A\frac{\partial^2 v}{\partial t^2}. \tag{2.3}$$

We rewrite this as

$$\frac{\partial^4 v}{\partial x^4} - \frac{1}{a^2}\frac{\partial^2 v}{\partial t^2} = 0, \tag{2.4}$$

*In Section 5.3, we will discuss the validity of this assumption for our experimental geometry, using finite-element simulations of the full geometry.

where we define $a = \sqrt{\frac{EI}{\rho w h}}$. If the beam is vibrating in an eigenmode, we can write $v(x,t) = X(x)(A\cos\Omega t + B\sin\Omega t)$. Substituting this in Equation (2.4) gives

$$\frac{\mathrm{d}^4 X}{\mathrm{d}x^4} - \frac{\omega^2}{a^2} X = 0, \tag{2.5}$$

and by defining $k^4 \equiv \frac{\omega^2}{a^2}$, we obtain

$$\frac{\mathrm{d}^4 X}{\mathrm{d}x^4} - k^4 X = 0. \tag{2.6}$$

If we let $X = e^{nx}$, we obtain

$$e^{nx}(n^4 - k^4) = 0, \tag{2.7}$$

which has solutions $n = (k, -k, -\mathrm{i}k, +\mathrm{i}k)$. The general solution can be written as

$$\begin{aligned} X =& C_1(\cos kx + \cosh kx) + C_2(\cos kx - \cosh kx) \\ &+ C_3(\sin kx + \sinh kx) + C_4(\sin kx - \sinh kx) \end{aligned} \tag{2.8}$$

The equation of motion being studied here is a fourth-order differential equation, and therefore requires four boundary conditions. For a doubly clamped beam, the beam displacement and bending at the endpoints are fixed to 0:

$$X|_{x=0} = 0, \qquad \left.\frac{\mathrm{d}X}{\mathrm{d}x}\right|_{x=0} = 0, \qquad X|_{x=L} = 0, \qquad \left.\frac{\mathrm{d}X}{\mathrm{d}x}\right|_{x=L} = 0. \tag{2.9}$$

The first two boundary conditions imply that $C_1 = C_3 = 0$. From the third and fourth boundary conditions we then obtain the coupled equations

$$C_2(\cos kL - \cosh kL) + C_4(\sin kL - \sinh kL) = 0 \tag{2.10}$$

$$-C_2(\sin kL + \sinh kL) + C_4(\cos kL - \cosh kL) = 0. \tag{2.11}$$

The determinant of this problem is

$$\cos(kL)\cosh(kL) - 1 = 0. \tag{2.12}$$

The zeros of this determinant can be found numerically, and determine values for $k$. Defining $\beta_n \equiv k_n / L$, we show these solutions in Table 2.1.

Using our previous definition of $k^4 = \frac{\omega^2}{a^2}$, the eigenfrequencies are

$$\omega_n = \frac{\beta_n^2}{L^2}\sqrt{\frac{EI}{\rho A}}. \tag{2.13}$$

The $\beta$ values determine the frequency spacing between the different modes. Note that the eigenfrequencies of a doubly clamped beam are not harmonically spaced.

| mode | 0 | 1 | 2 | 3 |
|---|---|---|---|---|
| $\beta_n$ | 4.73004 | 7.8532 | 10.9956 | 14.1372 |
| $C_{2,n}/C_{4,n}$ | 1.01781 | 0.999223 | 1.00003 | 0.999999 |
| $f_{n,\mathrm{in}}$ (MHz) | 14.2454 | 39.2679 | 76.9808 | 127.253 |
| $f_{n,\mathrm{in}}$ (MHz) (FEM) | 14.1988 | 38.8893 | 75.5933 | 123.644 |
| $f_{n,\mathrm{out}}$ (MHz) | 2.84907 | 7.85358 | 15.3962 | 25.4506 |
| $f_{n,\mathrm{out}}$ (MHz) (FEM) | 2.87522 | 7.97144 | 15.7509 | 26.3022 |

**Table 2.1:** Mode numbers for the first four modes of a doubly clamped flexural beam, showing $\beta$ and the ratio $C_2/C_4$. We also show, for a $Si_3N_4$ beam with parameters as given in Table 2.2, the in-plane and out-of-plane eigenfrequencies in MHz. These eigenfrequencies are both calculated, using Equation (2.13), and extracted from FEM simulations.

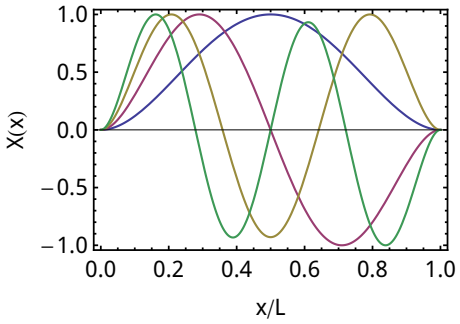


**Figure 2.2:** Mode shapes for the first four eigenmodes of a doubly clamped beam, from Equation (2.8) and with parameters $\beta_n$ and $C_{2,n}/C_{4,n}$ from Table 2.1, with the maximum mode amplitude $\max(X_n(x))$ normalized to 1.

| | | silicon nitride | gold |
|---|---|---|---|
| Young's modulus | $E$ | 250 GPa | 70 GPa |
| density | $\rho$ | 3100 kg/m$^3$ | 19300 kg/m$^3$ |
| thickness | $h$ | 50 nm | 100 nm |
| width | $w$ | 500 nm | 500 nm |
| length | $L$ | 18 µm | 18 µm |

**Table 2.2:** Parameters for silicon nitride and gold beams used in this section.

Again using the boundary conditions for a doubly clamped beam given in Equation (2.9) we can solve for $C_{2,n}/C_{4,n}$. This parameter determines the shape of the eigenmodes. We find the values in shown in Table 2.1 by solving

$$\frac{\mathrm{d}X(L)}{\mathrm{d}x} = 0. \tag{2.14}$$

The resulting mode shapes are plotted in Figure 2.2.

Using relevant experimental parameters, which we show in Table 2.2, we can calculate the in-plane and out-of-plane eigenfrequencies for silicon nitride nanobeams. These frequencies are shown in Table 2.1, together with values extracted from FEM simulations with identical geometrical and material parameters.

The values extracted from FEM are slightly different than the analytical results, with FEM underestimating the in-plane eigenfrequency and overestimating the out-of-plane eigenfrequency by less than 1%. We attribute this difference to inaccuracies in meshing the beam, mainly around the clamping points.

### 2.1.1 Effective mass calculation

The maximum potential energy of a harmonic oscillator is given by

$$U_{\mathrm{pot,max}} = \frac{1}{2} k v_{\mathrm{max}}^2 = \frac{1}{2} m_{\mathrm{eff}} \Omega_{\mathrm{m}}^2 v_{\mathrm{max}}^2, \tag{2.15}$$

where the spring constant is determined by $\Omega_{\mathrm{m}}^2 = \frac{k}{m_{\mathrm{eff}}}$ and $v_{\mathrm{max}}$ is the oscillator's maximum displacement. For the doubly clamped beams under consideration here, the maximum displacement is not constant along the beam: it is determined by the mode profile $X(x)$. We account for this by introducing the effective mass $m_{\mathrm{eff}}$ [70, 71]. We integrate the potential energy over the volume elements $\mathrm{d}V$ of the beam, normalized to the displacement at the center, as this is where we will generally probe the motion [72]:

$$U_{\mathrm{pot}} = \frac{1}{2} \Omega_{\mathrm{m}}^2 \int_0^L \mathrm{d}V \rho \Omega_{\mathrm{m}}^2 X(x)^2 = \frac{1}{2} m_{\mathrm{eff}} \Omega_{\mathrm{m}}^2 \max(X(x))^2. \tag{2.16}$$

The effective mass for the fundamental mode is then, with the maximum displacement $\max(X(x)) = X(L/2)$,

$$m_{\mathrm{eff}} = \int_0^L \mathrm{d}V \rho \frac{[X(x)]^2}{[X(L/2)]^2}. \tag{2.17}$$

Performing the integration for the fundamental mode, using the mode shape from Equation (2.8) and the parameters from Table 2.1, we obtain:

$$m_{\mathrm{eff}} = 0.39 whL\rho = 0.39 m_{\mathrm{phys}}, \tag{2.18}$$

where $m_{\mathrm{phys}} = whL\rho$ the physical mass of the beam.

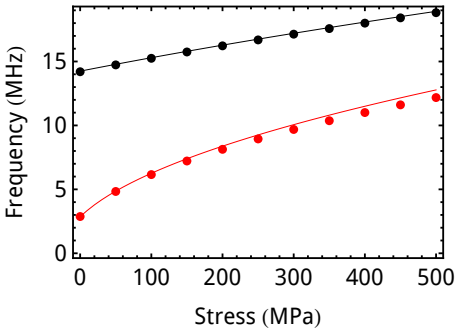


**Figure 2.3:** Eigenfrequencies for in-plane (black) and out-of-plane (red) mechanical modes of a silicon nitride beam. Dots are values extracted from FEM simulations, lines are analytical calculations using Equation (2.22). Parameters used are from Tables 2.1 and 2.2.

### 2.1.2 Flexural beams under the influence of axial tension

So far, we have only included flexural restoring forces. There can also be axial tension in a beam, causing an additional restoring force. This modifies the governing differential equation as follows [73]:

$$EI\frac{\mathrm{d}^4X}{\mathrm{d}X^4} - S\frac{\mathrm{d}^2X}{dx^2} = \rho A\omega^2 X, \tag{2.19}$$

where $S = \sigma A$ is the tension in the beam, calculated as the axial stress $\sigma$ times the cross-sectional area $A$. Using Rayleigh's method, equating the maximum kinetic energy and the maximum potential energy in the beam, we can solve for the eigenfrequencies of the beam:

$$\Omega^2 = \frac{EI}{L^4}\left(\frac{\int_0^1 \left(X''(\bar{x})\right)^2 \mathrm{d}\bar{x}}{\int_0^1 (X(\bar{x}))^2\,\mathrm{d}\bar{x}} + \frac{\sigma AL^2}{EI}\frac{\int_0^1 \left(X'(\bar{x})\right)^2 \mathrm{d}\bar{x}}{\int_0^1 (X(\bar{x}))^2\,\mathrm{d}\bar{x}}\right), \tag{2.20}$$

where $\bar{x} = x/L$, the (rescaled) position along the beam's length, and the prime ($'$) denotes differentiation with respect to $\bar{x}$.

We can then find the leading order stress dependence of the frequency by filling in the deflection function $X(x)$ for a beam in the absence of stress, as given in Equation (2.8), which we can rewrite for the fundamental mode (with $\beta = \beta_0$),

$$X(\bar{x}) = \cosh\beta_0\bar{x} - \cos\beta_0\bar{x} + \frac{\cosh\beta_0 - \cos\beta_0}{\sinh\beta_0 - \sin\beta_0}\left(\sin\beta_0\bar{x} - \sinh\beta_0\bar{x}\right), \tag{2.21}$$

finding the frequency $f$:

$$f = \frac{1}{2\pi}\frac{\beta_0^2}{L^2}\sqrt{\frac{EI}{\rho wh} + \frac{12.30\sigma L^2}{\rho\beta_0^4}}. \tag{2.22}$$

We can rewrite this as a function of the unstressed frequency $f_0$, shown in Equation (2.13), to emphasize the contribution of axial stress to the eigenfrequency:

$$f(\sigma) = f_0 \sqrt{1 + \frac{\sigma L^2}{3.4 E h^2}}. \tag{2.23}$$

Figure 2.3 plots the resulting eigenfrequencies for a silicon nitride beam with parameters given in Table 2.2, and compares these analytical results with values extracted from FEM simulations. The agreement for the in-plane mode is very good. However, for high stress we see that the FEM simulations predict a slightly lower eigenfrequency than the analytical calculation. We attribute this to not having enough mesh points in the out-of-plane direction in the FEM simulations, thereby not modeling the geometry accurately enough. As the out-of-plane thickness is 10 times smaller than the the in-plane width, this direction is easily under-meshed.

### 2.1.3 Bilayer beams

In Chapters 4 and 5 we study beams made of silicon nitride covered with a layer of gold. To model these bilayer beams, the values for the Young's modulus, density and stress must be replaced with effective parameters that represent the weighted average of the two materials, each with cross-section area $A_m = w_m h_m$:

$$E_e = \frac{E_{\mathrm{Si_3N_4}} A_{\mathrm{Si_3N_4}} + E_{\mathrm{Au}} A_{\mathrm{Au}}}{A_{\mathrm{Si_3N_4}} + A_{\mathrm{Au}}} \tag{2.24}$$

$$\rho_e = \frac{\rho_{\mathrm{Si_3N_4}} A_{\mathrm{Si_3N_4}} + \rho_{\mathrm{Au}} A_{\mathrm{Au}}}{A_{\mathrm{Si_3N_4}} + A_{\mathrm{Au}}} \tag{2.25}$$

$$\sigma_e = \frac{\sigma_{\mathrm{Si_3N_4}} A_{\mathrm{Si_3N_4}} + \sigma_{\mathrm{Au}} A_{\mathrm{Au}}}{A_{\mathrm{Si_3N_4}} + A_{\mathrm{Au}}}, \tag{2.26}$$

as shown by Su *et al.* [74] and Bose *et al.* [75]. We use this to modify Equation (2.22), and compare the result to values extracted from FEM simulations for a bilayer beam in Figure 2.4, and observe a good match. Due to the added layer of gold, the eigenfrequencies are lower when compared to the silicon-nitride-only beam eigenfrequencies shown in Figure 2.3.

## 2.2 Spectral density

To study the (very small) mechanical motion of the beams, and to determine the sensitivity with which this can be done, it is useful to define noise spectral densities. For a review of noise spectral densities, we refer to the appendices of Clerk *et al.* [76].

#### Wiener–Khinchin theorem

A measurement of an observable $X(t)$ is typically performed during a finite time $T$. The gated Fourier transform $X_T(\Omega)$ of $X(t)$ respresents the spectral content of a

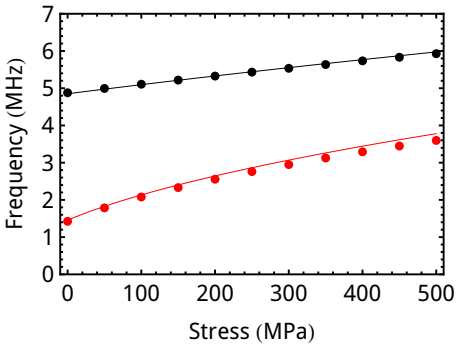


**Figure 2.4:** Eigenfrequencies for in-plane (black) and out-of-plane (red) mechanical modes of a bilayer silicon nitride and gold beam. Dots are values extracted from FEM simulations. Lines are an analytical model using Equation (2.22) with Equations (2.24)–(2.26). Parameters used are from Tables 2.1 and 2.2.

single observed trace:

$$X_{\mathrm{T}}(\Omega) = \frac{1}{\sqrt{T}} \int_{-T/2}^{T/2} X(t) e^{\mathrm{i}\Omega t} \mathrm{d}t. \tag{2.27}$$

By repeating the measurement over (individual) runs, we can obtain the spectral density $\left\langle |X(\Omega)|^2 \right\rangle$.

We can also define the noise power spectral density of the process $X(t)$ as the Fourier transform* of the autocorrelation function:

$$S_{\mathrm{XX}}(\Omega) \equiv \int_{-\infty}^{\infty} \langle X(t)X(0) \rangle e^{\mathrm{i}\omega t} \mathrm{d}t \tag{2.28}$$

In most cases we are dealing with *stationary* processes, for which the autocorrelation function $\left\langle X(t+t')X(t) \right\rangle$ does not depend on $t$ and can therefore be given by $\langle X(t)X(0) \rangle$. In these cases, the Wiener–Khinchin theorem links the measured spectral density to the noise power spectral density:

$$S_{\mathrm{XX}}(\Omega) = \lim_{T\to\infty} \left\langle |X_T(\Omega)|^2 \right\rangle = \lim_{T\to\infty} \langle X_T(\Omega) X_T(-\Omega) \rangle, \tag{2.29}$$

Note that this is a "two-sided" spectral density, defined for positive and negative frequencies $\Omega$. We also define a "single-sided" spectral density, for $\Omega \geq 0$, as

$$S_{\mathrm{X}}(\Omega) = 2S_{\mathrm{XX}}(\Omega), \tag{2.30}$$

if we assume $X(t)$ is a real-valued and classical variable ($X(t)$ and $X(t')$ commute for all $\{t, t'\}$). The units of both $S_{\mathrm{X}}$ and $S_{\mathrm{XX}}$ are $[X]^2/\mathrm{Hz}$. Note that the square root of a spectral density $\sqrt{S_{\mathrm{XX}}}$ is also often quoted, with units $[X]/\sqrt{\mathrm{Hz}}$.

*We define the Fourier transform of a function $f(x)$ as $\tilde{f}(\omega) = \int_{-\infty}^{\infty} f(x) e^{\mathrm{i}\omega t} \mathrm{d}t$.

By integrating the spectral density in Equation (2.29), we obtain:

$$\int_{-\infty}^{\infty} S_{XX}(\Omega)\frac{d\Omega}{2\pi} = \langle X^2 \rangle. \tag{2.31}$$

As such, the integral over a spectral density is the variance of the signal.

#### Transfer function

If two processes $X$ and $Y$ are linearly related through

$$Y(\Omega) = g(\Omega)X(\Omega), \tag{2.32}$$

the spectral densities $S_{YY}$ and $S_{XX}$ are related as

$$S_{YY}(\Omega) = \left|g(\Omega)\right|^2 S_{XX}(\Omega). \tag{2.33}$$

The function $\left|g(\Omega)\right|^2$ is called a transfer function.

### 2.2.1 Spectral displacement density

The mechanical modes of the beams we study can be characterized by their susceptibility, which depends on their eigenfrequency $\Omega_m$, damping rate $\Gamma_m$ and effective mass $m_{eff}$. In Section 2.1, we used Euler-Bernoulli beam theory to determine $\Omega_m$ and $m_{eff}$. Here, we will derive the susceptibility and determine the thermal fluctuations of the eigenmodes of a mechanical system. Assuming that the different modes of the system are sufficiently separated in frequency ($(\Omega_2 - \Omega_1) \gg \Gamma_1, \Gamma_2$), where $\Gamma_1$, $\Gamma_2$ are the loss rates of the modes, we can describe the different modes independently. Then, we can describe the time evolution of the position $x(t)$ for one of the modes by the equation of motion for a harmonic oscillator:

$$m_{eff}\frac{\mathrm{d}x^2(t)}{\mathrm{d}t^2} + m_{eff}\Gamma_m\frac{\mathrm{d}x(t)}{\mathrm{d}t} + m_{eff}\Omega_m^2 x(t) = F_{ext}(t), \tag{2.34}$$

where $F_{ext}$ is the sum of all the forces acting on the system. If there are no external driving forces, only the stochastic thermal Langevin force contributes. In frequency space, the solution can be written as $\delta x(\Omega) = \chi_{xx}(\Omega)F_{ext}(\Omega)$. This defines the mechanical susceptibility, connecting the driving force to the response of the mechanical oscillator:

$$\chi_{xx}(\Omega) = \frac{1}{m_{eff}(\Omega_m^2 - \Omega^2) - \mathrm{i}m_{eff}\Gamma_m\Omega}, \tag{2.35}$$

#### Fluctuation-dissipation theorem

With the equation for the susceptibility given in Equation (2.35), the fluctuation-dissipation theorem relates the thermal displacement spectral density to the

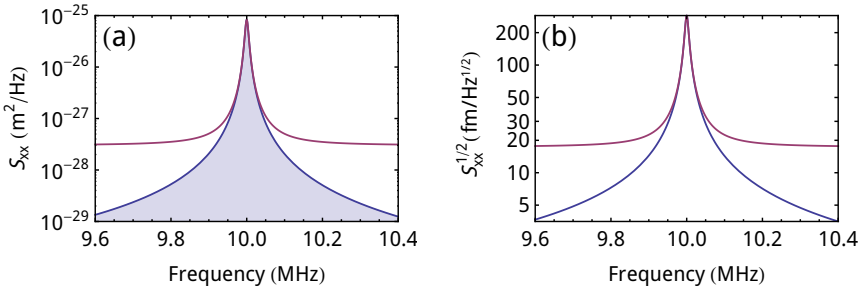


**Figure 2.5:** Spectral displacement density of a mechanical oscillator with $\Omega_m = 2\pi \times 10$ MHz, $Q = 1000$, $m_{eff} = 160$ fg. (a): Spectral displacement density (blue line), and spectral displacement density with added imprecision level $S_{xx}^{imp} = 3 \times 10^{-28}$ m$^2$/Hz (purple line). Integration of the spectral displacement density $S_{xx}^{th}(\Omega)$ (indicated by the blue shading) gives the variance of the displacement $\langle x^2 \rangle = 1.6 \times 10^{-20}$ m$^2$, using Equation (2.31). (b): Same data as (a), but plotted as $\sqrt{S_{xx}(\Omega)}$, as is often seen in the literature, with units of fm/Hz$^{1/2}$.

mechanical susceptibility [68]:

$$\begin{aligned} S_{xx}^{th}(\Omega) &= 2\frac{k_B T}{\Omega}\mathrm{Im}\chi_{xx} \\ &= \frac{1}{m_{eff}}\frac{2\Gamma_m}{(\Omega^2-\Omega_m^2)^2+\Gamma_m^2\Omega^2}k_B T, \end{aligned} \tag{2.36}$$

which is plotted in Figure 2.5 for the experimental parameters of the nanomechanical systems studied in Chapter 6: $\Omega_0 = 2\pi \times 10$ MHz, $m_{eff} = 160$ fg, $Q = \Omega_0/\Gamma_m = 1000$, $T = 300$ K.

Integrating $S_{xx}^{th}(\Omega)$ according to Equation (2.31) yields the variance, which for weak damping is given by the equipartition theorem [68]:

$$\langle x^2 \rangle = \frac{k_B T}{m_{eff}\Omega_m^2}, \tag{2.37}$$

finding $\sqrt{\langle x^2 \rangle} = 1.26 \times 10^{-10}$ m for the spectral displacement density shown in Figure 2.5. Here, we see an advantage of high-$Q$ oscillators: because $\langle x^2 \rangle$ does not depend on $Q$, having a higher $Q$ leads to a higher peak displacement.

## 2.3 Dipolar scattering

Now we have determined the mechanical properties of the system, we turn to the optical properties. To model plasmonic transduction of motion, we will consider

how a dipolar scatterer, which has a polarizability that is a function of some mechanical degree of freedom characterized by position coordinate $x$, can be used to transduce the mechanical motion $x(t)$. First, we discuss how a conformational change, caused by mechanical displacement, affects the polarizability of the scattering system, while properly taking into account radiation reaction.

### 2.3.1 Coupled-dipole polarizability

As an example of a system that can show a strongly changing optical response upon nanoscale displacements, let's consider a scatterer consisting of two particles that we will treat as point dipoles, separated by a distance $d$ which is much smaller than the wavelength of light. The total dipole moment of the system is then given by

$$\mathbf{p} = \mathbf{p}_1 + \mathbf{p}_2. \tag{2.38}$$

If the total scattering system is sufficiently small, i.e. much smaller than the wavelength, its interaction with a light beam can be described in the dipolar approximation: an incident light field $\mathbf{E}_{\text{in}}$ induces a dipole moment

$$\mathbf{p} = \boldsymbol{\alpha} \cdot \mathbf{E}_{\text{in}}, \tag{2.39}$$

where $\boldsymbol{\alpha}$ is the 3×3 polarizability tensor associated with the scatterer (we neglect magnetic interactions here). The induced dipole at position $\mathbf{r}_0$ gives rise to a scattered field

$$\mathbf{E}_{\text{dip}}(\mathbf{r}) = \frac{k^2}{4\pi\epsilon_0 r} e^{\mathrm{i}kr} \left( \left(\hat{\mathbf{r}} \times \mathbf{p}\right) \times \hat{\mathbf{r}} + \left(3\hat{\mathbf{r}}\left(\hat{\mathbf{r}} \cdot \mathbf{p}\right) - \mathbf{p}\right) \left( \frac{1}{(kr)^2} - \frac{\mathrm{i}}{kr} \right) \right) \tag{2.40}$$

in free space, where $r = |\mathbf{r} - \mathbf{r}_0|$ and $k = \omega/c$.

Neglecting radiation for the moment, the equation of motion of dipole 1 in the electrostatic limit can be expressed to first order as

$$\ddot{\mathbf{p}}_1 + \gamma_{\text{i}} \dot{\mathbf{p}}_1 + \omega_0^2 \mathbf{p}_1 = f_1 \mathbf{E}_1, \tag{2.41}$$

where $\mathbf{p}_1$ is the induced dipole moment, $\gamma_{\text{i}}$ the internal dissipation rate (i.e., absorption), $\omega_0$ the resonance frequency, and $f_1$ the oscillator strength of the individual particle. Note that the definition of $f$ here is different from the usual definition of atomic oscillator strength expressed in units of $e^2/m_e$, with $e$ and $m_e$ the electron charge and mass, respectively. We can however still interpret its magnitude as $q^2/m$, where $q$ is the induced charge and $m$ its effective mass. In the case of our dimer, the dipole is driven by the field $\mathbf{E}_1$ consisting of the incident field, with strength $E_{\text{in}}$, and the field of the second dipole. For small $d$, and for an incident field aligned along the line connecting both particles (which we define as the $x$ axis), the magnitude $E_1$ of the field can be found from Equation (2.40) as

$$E_1 = E_{\text{in}} + \frac{p_2}{2\pi\epsilon_0 d^3} \tag{2.42}$$

where we have now changed to scalar notation as we are considering only fields and dipole moments along the $x$ direction. Since $p_1 = p_2$ and $f_1 = f_2$ we can write the equation of motion for the dipole moment of particle 1:

$$\ddot{p}_1 + \gamma_i \dot{p}_1 + \left(\omega_0^2 - \frac{f_1}{2\pi\epsilon_0 d^3}\right) p_1 = f_1 E_{in}, \tag{2.43}$$

The above equation can be written in the Fourier domain as

$$\left(\omega_0^2 - \frac{f_1}{2\pi\epsilon_0 d^3} - \omega^2 - i\gamma_i\omega\right) p_1 = f_1 E_{in}. \tag{2.44}$$

As such we can identify the electrostatic polarizability of the first dipole (responding to $E_{in}$ and in the presence of particle 2):

$$\alpha_1(\omega) = \frac{f_1}{\omega_{es}^2 - \omega^2 - i\gamma_i\omega}, \tag{2.45}$$

writing

$$\omega_{es} = \sqrt{\omega_0^2 - \frac{f_1}{2\pi\epsilon_0 d^3}}. \tag{2.46}$$

We will consider the effect of small variations $\delta x$ of $d$ on the resonance frequency $\omega_n$. We write $d = \bar{d} + \delta x$. Approximating $\omega_{es}$ as $\omega_{es}(\delta x) = \bar{\omega}_{es} + G\delta x$ by taking the first term in the Taylor expansion, we obtain for the polarizability:

$$\alpha_1(\omega) = \frac{f_1}{\bar{\omega}_{es}^2 + 2G\bar{\omega}_{es}\delta x - \omega^2 - i\gamma_i\omega}, \tag{2.47}$$

with coupling strength

$$G = \frac{3f_1}{4\pi\epsilon_0\bar{\omega}_{es}\bar{d}^4} \tag{2.48}$$

This parameter, the frequency shift per unit displacement, is a measure for the strength of the optomechanical interaction. To make an estimate for its magnitude, let's consider each dipole to be a small spherical particle with electrostatic polarizability [45]:

$$\alpha_0(\omega) = 4\pi\epsilon_0 V\left(\frac{\epsilon - \epsilon_m}{\epsilon + 2\epsilon_m}\right), \tag{2.49}$$

where $\epsilon$ is the dielectric constant of the metal, $\epsilon_m$ is the dielectric constant of the surrounding medium and $V = \frac{4}{3}\pi a^3$ is the particle's volume. For a metallic particle in vacuum ($\epsilon_m = 1$), using the Drude model for the metal permittivity,

$$\epsilon_{Drude} = 1 - \frac{\omega_p^2}{\omega(\omega + i\gamma_i)}, \tag{2.50}$$

we can obtain for the polarizability

$$\alpha_0(\omega) = 4\pi\epsilon_0 V\frac{\omega_0^2}{\omega_0^2 - \omega^2 - i\gamma_i\omega}, \tag{2.51}$$

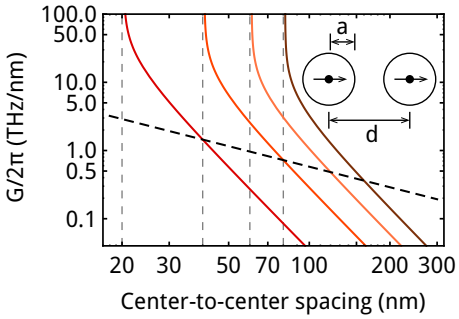


**Figure 2.6:** Dependence of coupling strength $G$ on interparticle spacing $\bar{d}$, for gold nanoparticle dimers, with particle diameters of 20, 40, 60, and 80 nm (red to brown). The dashed black line indicates $\bar{d} = 4a$ (particles spaced by one diameter). The coupling strength diverges for touching particles ($\bar{d} = 2a$).

with $\omega_0 = \omega_p/\sqrt{3}$ for a spherical particle. We can then recognize the oscillator strength $f_1$ in Equation (2.45) as

$$f_1 = 4\pi\epsilon_0 V\omega_0^2, \tag{2.52}$$

and rewrite the electrostatic resonance frequency (Equation (2.46)) as:

$$\omega_{es} = \sqrt{\omega_0^2\left(1 - 2\frac{V}{d^3}\right)}. \tag{2.53}$$

As a result, the coupling strength (Equation (2.48)) for two spherical nanoparticles is

$$G = \frac{3V\omega_0^2}{\bar{\omega}_{es}\bar{d}^4}, \tag{2.54}$$

where $G$ has units of [frequency]/[distance]. Figure 2.6 shows $G$ for gold nanoparticles of radius 10 nm, 20 nm, 30 nm, and 40 nm (red to brown), using a plasma frequency for gold of $\omega_p = 2\pi \times 476$ THz [77]. We can see that for particles spaced by about 1 particle diameter, marked by the dashed black line, this dipole–dipole model predicts a coupling strength of $G \approx 2\pi \times 1$ THz/nm. When the particles touch ($\bar{d} = 2a$), the coupling strength diverges. In this regime, this dipole–dipole model will have lost its validity, as higher order modes will start playing an important role.

### 2.3.2 Radiation reaction

We can now express the polarizability of the total system of two coupled dipoles as

$$\alpha(\omega) = \frac{f}{\omega_{es}^2 - \omega^2 - i\gamma_i\omega}, \tag{2.55}$$

using $f = f_1 + f_2 = 2f_1$. At this point, it is crucial to correctly take into account the effect of radiation reaction, which we have omitted up to now: we need to acknowledge the action of the scattered field on the scatterer itself [78, 79]. The electrostatic polarizability should be corrected as

$$\boldsymbol{\alpha}^{-1} = \boldsymbol{\alpha}_{\mathrm{es}}^{-1} - \overleftrightarrow{\mathbf{G}}(\mathbf{r}_0, \mathbf{r}_0). \tag{2.56}$$

In this correction, $\overleftrightarrow{\mathbf{G}}(\mathbf{r}_1, \mathbf{r}_0) = \frac{\omega^2 \mu_0}{4\pi r} e^{ikr}$ is the Green's function, with $r = |\mathbf{r}_1 - \mathbf{r}_0|$, that describes the electric field at position $\mathbf{r}_1$ produced by a dipole at position $\mathbf{r}_0$ through

$$\mathbf{E}(\mathbf{r}_1) = \overleftrightarrow{\mathbf{G}}(\mathbf{r}_1, \mathbf{r}_0) \cdot \mathbf{p}. \tag{2.57}$$

The real and imaginary part of $\overleftrightarrow{\mathbf{G}}(\mathbf{r}_0, \mathbf{r}_0)$ cause a frequency shift and radiation damping, respectively. We take the first order expansion of $\overleftrightarrow{\mathbf{G}}$:

$$\mathrm{Re}(\overleftrightarrow{\mathbf{G}}(\mathbf{r}_1, \mathbf{r}_0)) \approx \frac{1}{2\pi\epsilon_0 |\mathbf{r}_1 - \mathbf{r}_0|^3} \tag{2.58}$$

$$\mathrm{Im}(\overleftrightarrow{\mathbf{G}}) \approx \frac{\omega^3}{6\pi\epsilon_0 c^3} \tag{2.59}$$

The real part of $\overleftrightarrow{\mathbf{G}}(\mathbf{r}_0, \mathbf{r}_0)$ diverges for a point dipole, an issue that is usually treated by introducing an effective cutoff radius $r_c$ (motivated by the reasoning that realistic charge distributions have some finite size) such that the phenomenological resonance frequency $\omega_{\mathrm{n}}$ is obtained:

$$\omega_{\mathrm{n}}^2 = \omega_{\mathrm{es}}^2 - \frac{f}{2\pi\epsilon_0 r_c^3}. \tag{2.60}$$

The imaginary part leads to an effective total damping

$$\gamma = \gamma_{\mathrm{i}} + \frac{f\omega^2}{6\pi\epsilon_0 c^3}. \tag{2.61}$$

Properly taking into account radiation reaction therefore leads to a polarizability for the dimer system:

$$\alpha(\omega) = \frac{f}{\omega_{\mathrm{n}}^2 - \omega^2 - \mathrm{i}\omega\gamma}. \tag{2.62}$$

We can rewrite the electrostatic coupling strength $G$ from Equation (2.54) in terms of the electrodynamic variables:

$$G = \frac{3f}{2\pi\epsilon_0 \bar{\omega}_{\mathrm{n}} \bar{d}^4} \tag{2.63}$$

leading to the polarizability

$$\alpha(\omega) = \frac{f}{\bar{\omega}_{\mathrm{n}}^2 + 2G\bar{\omega}_{\mathrm{n}}\delta x - \omega^2 - \mathrm{i}\gamma\omega}. \tag{2.64}$$

#### Change in particle radius

Up to now, we have discussed changing the center-to-center distance between two particles. As the plasmon resonance frequency depends on the radius of a single particle, internal mechanical modes of a plasmonic particle can also lead to changes in scattering [80]. Typically, these internal modes have frequencies in the GHz range, with gold nanoparticles measured to have stretch vibrations between 3 and 7 GHz [81, 82], and radial breathing modes up to 100 GHz [83, 84]. These high frequencies make measuring the scattering in the time domain challenging, and therefore these modes are often studied with for instance Raman scattering [85, 86] or time-resolved pump-probe measurements [87, 88]. Due to the high frequencies involved, we will not observe these effects in this thesis.

### 2.3.3 Determining $\partial\alpha(\omega)/\partial x$

We are modeling a scattering system with a transmittance $\mathscr{T}$, that depends on scattered power and extinct power, as observables. The scattered power scales with $|\alpha|^2$, and the power extinct from the beam scales with $\mathrm{Im}(\alpha)$ [45]. It is therefore useful to determine expressions for $|\alpha|^2$ and $\mathrm{Im}(\alpha)$. From Equation (2.62), we can find the following expressions:

$$\mathrm{Im}(\alpha) = \frac{f\omega\gamma}{\left(\omega_\mathrm{n}^2-\omega^2\right)^2+\omega^2\gamma^2} \qquad |\alpha|^2 = \frac{f^2}{\left(\omega_\mathrm{n}^2-\omega^2\right)^2+\omega^2\gamma^2}. \tag{2.65}$$

For the transduction of motion, it is not the value of the transmittance that is of paramount importance, but the change in transmittance with a mechanical change, expressed as the partial derivative $\frac{\partial\mathscr{T}}{\partial x}$. This change in transmittance then depends on $\frac{\partial|\alpha|^2}{\partial x}$ and $\frac{\partial\mathrm{Im}(\alpha)}{\partial x}$.

We therefore calculate the derivatives of $\mathrm{Im}(\alpha)$ and $|\alpha|^2$ with respect to $x$ from Equation (2.65):

$$\frac{\partial\mathrm{Im}(\alpha)}{\partial x} = -4G\frac{f\omega\gamma\bar{\omega}_\mathrm{n}(\bar{\omega}_\mathrm{n}^2-\omega^2)}{\left((\bar{\omega}_\mathrm{n}^2-\omega^2)^2+\omega^2\gamma^2\right)^2} \tag{2.66}$$

$$\frac{\partial|\alpha|^2}{\partial x} = -4G\frac{f^2\bar{\omega}_\mathrm{n}(\bar{\omega}_\mathrm{n}^2-\omega^2)}{\left((\bar{\omega}_\mathrm{n}^2-\omega^2)^2+\omega^2\gamma^2\right)^2}. \tag{2.67}$$

In Figure 2.7a and b, we show $\mathrm{Im}(\alpha)$ and $|\alpha|^2$ as a function of changing center frequency, choosing center frequencies 350, 375, 400 and 425 THz. The albedo, which is defined as

$$\mathscr{A} \equiv \frac{\gamma-\gamma_\mathrm{i}}{\gamma} = \frac{f\omega^2}{6\pi\epsilon_0 c^3\gamma} \tag{2.68}$$

is $\mathscr{A}\approx 0.85$ for these scatterers, and they have quality factor $Q_\mathrm{opt}\equiv\omega_0/\gamma\approx 6$. We see the effect of changing the center frequency, showing the effect of radiation reaction

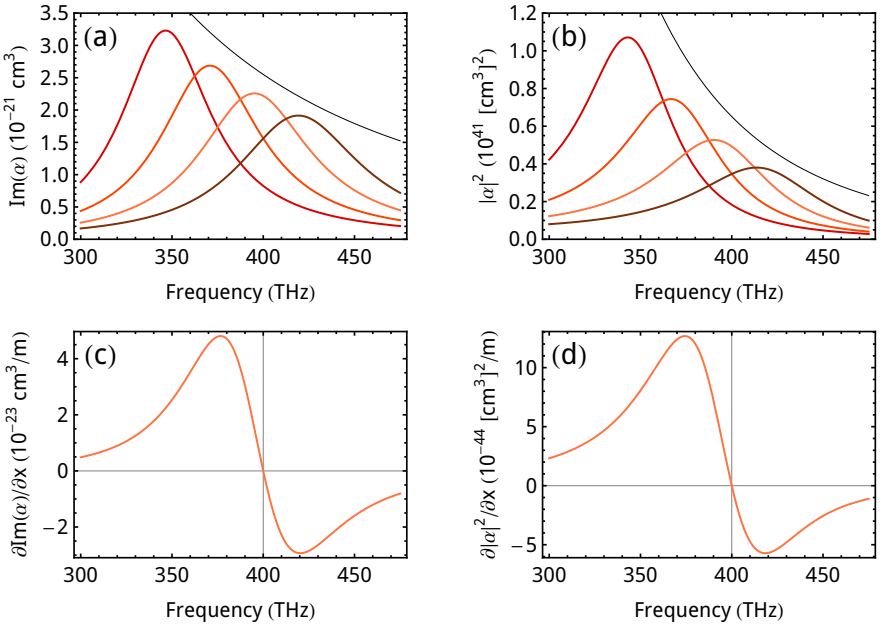


**Figure 2.7:** Dispersive change in polarizability. (a): Imaginary part of polarizability $\mathrm{Im}(\alpha)$, for center frequencies $\omega_0 = 2\pi \times 350, 375, 400, 425$ THz (from red to brown), with optical quality factor $Q_{\mathrm{opt}} \approx 6$, albedo $\mathscr{A} \approx 0.85$. Data is plotted in units of [cm$^3$], which is equal to $\mathrm{Im}(\alpha)/(4\pi\epsilon_0)$ in SI units. The black line is the imaginary part of the unitary limit shown in Equation (2.73). (b): $|\alpha|^2$ for scatterers identical to those in (a). (c): Change in $\mathrm{Im}(\alpha)$ for the scatterer with $\omega_0 = 2\pi \times 400$ THz, with $G = 2\pi \times 1$ THz/nm and a change in interparticle spacing $\delta x = 1$ nm. (d): Change in $|\alpha|^2$, for parameters identical to those in (c).

on the polarizabilities. For higher center frequencies, the radiation reaction lowers the quality factor and slightly increases the albedo. In Figure 2.7c and d, we plot the change in polarizability for a change in particle spacing of $\delta x = 1$ nm with a coupling strength $G = 2\pi \times 1$ THz/nm. We see that the red side of the resonance shows a stronger change in polarizability, due to radiation reaction. Therefore, choosing a red detuning to measure small mechanical changes in such a scattering system will be more sensitive.

In many realistic systems, it will however not only be the resonance frequency that changes upon a displacement $\delta x$. In the example of the dimer, the fact that the particles will have finite size, comparable to their separation, will establish a contribution of higher order multipoles to the interparticle coupling. For coupled dipolar particles, this leads to an increased induced charge to compensate for the field gradient experienced by the finite-sized particle. As such, also the oscillator

strength $f$ can change with the distance $d$. We will write $f(\delta x) = \bar{f} + F\delta x$. By filling in Equation (2.62), this leads to:

$$\alpha(\omega) = \frac{(\bar{f} + F\delta x)}{\omega_{\mathrm{es}}^2 - \frac{\bar{f}+F\delta x}{2\pi\epsilon_0 \bar{d}^3\left(1+\frac{\delta x}{\bar{d}}\right)^3} - \frac{\bar{f}+F\delta x}{2\pi\epsilon_0 r_c^3} - \omega^2 - \mathrm{i}\omega\left(\gamma_{\mathrm{i}} + \frac{\omega^2(\bar{f}+F\delta x)}{6\pi\epsilon_0 c^3}\right)}, \tag{2.69}$$

which reduces to

$$\alpha(\omega) \approx \frac{(\bar{f} + F\delta x)}{\bar{\omega}_{\mathrm{n}} - 2G\bar{\omega}_{\mathrm{n}}\delta x - F\delta x\left(\frac{1}{2\pi\epsilon_0 \bar{d}^3} + \frac{\omega_{\mathrm{es}}^2 - \omega_{\mathrm{n}}}{f}\right) - \omega^2 - \mathrm{i}\omega\left(\bar{\gamma} + \frac{\omega^2 F\delta x}{6\pi\epsilon_0 c^3}\right)} \tag{2.70}$$

where we see that the (radiative) damping rate is affected when the oscillator strength varies with displacement, leading to a natural appearance of dissipative optomechanical coupling alongside dispersive coupling. In Chapter 6, in Figure 6.2b, we will show finite-difference-time-domain simulations of the scattering cross section of coupled dipolar gold nanoparticles, showing both a frequency shift $G$ and change in oscillator strength $F$ with changing separation $\bar{d}$.

From Equation (2.70), it is straightforward to derive $\mathrm{Im}(\alpha)$ and $|\alpha|^2$ as well as $\partial\mathrm{Im}(\alpha)/\partial x$ and $\partial|\alpha|^2/\partial x$. In Figure 2.8a and b, we show $\mathrm{Im}(\alpha)$ and $|\alpha|^2$, applying a large dissipative coupling strength $F$. Figure 2.8c and d show the derivatives of $\mathrm{Im}(\alpha)$ and $|\alpha|^2$ with $F = 0.1$, for a change in interparticle spacing of 1 nm. Note that due to the change in oscillator strength, the transduction is stronger on the red side of the resonance, as was also observed for dispersive coupling in Figure 2.7. We note that the magnitude of $F$ is not predicted by the model shown in this section and must therefore still be determined from e.g. FDTD simulations for experimental geometries.

### 2.3.4 Cross sections

With expressions for $\mathrm{Im}(\alpha)$ and $|\alpha|^2$, we can calculate the extinction and scattering cross sections [45]. These observable quantities express how much light is extinct or scattered by a polarizable particle from an incident plane wave:

$$C_{\mathrm{ext}} = \frac{\omega}{\epsilon_0 c}\mathrm{Im}(\alpha) \tag{2.71}$$

$$C_{\mathrm{sca}} = \frac{\omega^4}{6\pi\epsilon_0^2 c^4}|\alpha|^2. \tag{2.72}$$

Using these cross sections, we can determine that for the polarizability shown in Figure 2.7, we have $C_{\mathrm{ext}} = 0.178\ \mu\mathrm{m}^2$, $C_{\mathrm{sca}} = 0.153\ \mu\mathrm{m}^2$, and the relative change in both $C_{\mathrm{ext}}$ and $C_{\mathrm{sca}}$ for $\delta x = 1$ nm is 2.7%/nm. We can also calculate the albedo, using $\mathscr{A} \equiv C_{\mathrm{sca}}/C_{\mathrm{ext}}$, evaluated at resonance. In Figures 2.7 and 2.8, the scatterer has $\mathscr{A} = 0.87$.

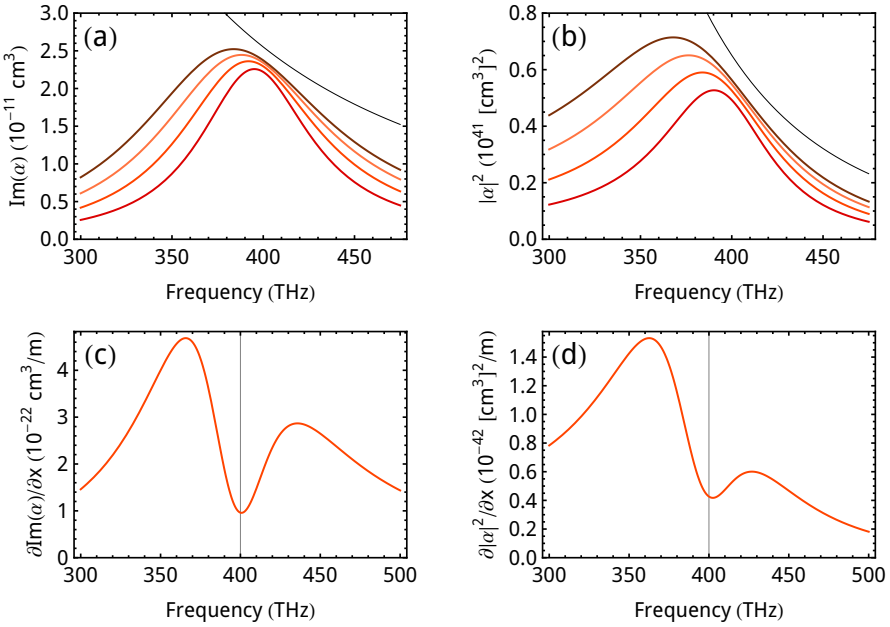


**Figure 2.8:** Dissipative change in polarizability. (a): Imaginary part of polarizability $\mathrm{Im}(\alpha)$, with dissipative coupling strength $F = (0, 0.2, 0.4, 0.6)$ (from red to brown), with center frequency $\omega_0 = 2\pi \times 400$ THz, optical quality factor $Q_{\mathrm{opt}} \approx 6$ and albedo $\mathscr{A} \approx 0.85$. Data is plotted in units of [cm$^3$], which is equal to $\mathrm{Im}(\alpha)/(4\pi\epsilon_0)$ in SI units. The black line is the imaginary part of the unitary limit shown in Equation (2.73). (b): $|\alpha|^2$ for scatterers identical to those in (a). (c): Change in $\mathrm{Im}(\alpha)$ for the scatterer with $\omega_0 = 2\pi \times 400$ THz, with $F = 0.2$ and a change in interparticle spacing $\delta x = 1$ nm. (d): Change in $|\alpha|^2$, for parameters identical to those in (c).

With the inclusion of radiation reaction in the polarizability, we can also calculate the unitary limit. This is the polarizability for a scatterer with no intrinsic loss $\gamma_{\mathrm{i}}$, so that all energy is reradiated: such a particle has an albedo $\mathscr{A} = 1$. Setting $\gamma_{\mathrm{i}} = 0$ and assuming resonance, $\omega_{\mathrm{n}} = \omega$, Equation (2.62) reduces to

$$\alpha_{\mathrm{uni}} = \frac{6\pi \mathrm{i} \epsilon_0 c^3}{\omega^3}. \tag{2.73}$$

Calculating the extinction cross section for this unitary limit gives:

$$C_{\mathrm{uni}} = \frac{3\lambda^2}{2\pi}, \tag{2.74}$$

where $\lambda = \frac{2\pi c}{\omega}$ is the free-space wavelength. We can then also express the albedo as $\mathscr{A} = \mathrm{Im}(\alpha)/\mathrm{Im}(\alpha_{\mathrm{uni}})$.

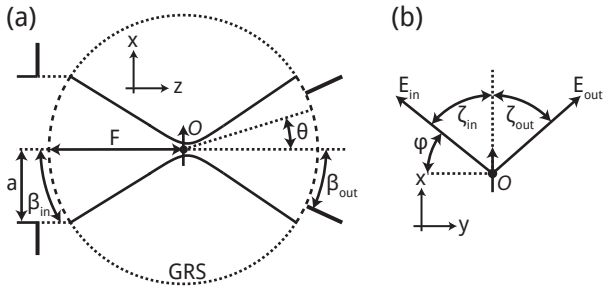


**Figure 2.9:** Schematic of the coordinates used in Section 2.3.5. (a): Reference sphere for focusing. (b): Angles for input and output polarization, as used in Section 2.3.6. The scatterer is at the origin, marked by $O$.

These cross sections are useful, as they give physical intuition, expressing the interaction of a scatterer with light as an area, which can be related to the particle size. They are however only valid for interaction with a plane wave, and do not describe the interaction of a scatterer with a focused beam. Therefore, in the next section, we will determine the electric field at the focus of a laser beam, and determine the interaction of a scatterer with this field, using $\alpha$, $\mathrm{Im}(\alpha)$ and $|\alpha|^2$ as derived in this section.

### 2.3.5 Interaction with a focused beam

We will now consider the situation where the scatterer is illuminated with a beam that is focused using an input lens with opening angle $\beta_{\mathrm{in}}$, and light is collected through a second lens with opening angle $\beta_{\mathrm{out}}$* (see Figure 2.9a). We follow here the treatment of Novotny and Hecht [78]. It has been shown before that for plasmonic particles near-unity extinction can be obtained using tightly focused beams [89–92].

We will assume that the lenses have unity transmission coefficients and the medium surrounding the scatterer is air. For a given input field $\mathbf{E}_{\mathrm{in}}(\theta,\phi) = \left(E_{x,\mathrm{in}}(\theta,\phi), E_{y,\mathrm{in}}(\theta,\phi), 0\right)$, the field just to the right of the reference sphere of the focusing lens, with focal length $F$, is

$$\mathbf{E}_{\infty,\mathrm{in}}(\theta,\phi) = \sqrt{\cos\theta}\begin{pmatrix} \sin^2\phi + \cos^2\phi\cos\theta & \sin\phi\cos\phi(\cos\theta-1) \\ \sin\phi\cos\phi(\cos\theta-1) & \cos^2\phi + \sin^2\phi\cos\theta \\ -\cos\phi\sin\theta & \sin\phi\sin\theta \end{pmatrix}\begin{pmatrix} E_{x,\mathrm{in}}(\theta,\phi) \\ E_{y,\mathrm{in}}(\theta,\phi) \end{pmatrix}. \tag{2.75}$$

*We will also express the opening angle of objectives as a numerical aperture (NA), where NA $\equiv n\sin\beta$, with $n$ the refractive index of the medium surrounding the lens.

The focal field can be derived from this far field through

$$\mathbf{E}(\rho,\phi,z) = -\frac{\mathrm{i}kFe^{-\mathrm{i}kF}}{2\pi}\int_0^{\beta_{\mathrm{in}}}\int_0^{2\pi}\mathbf{E}_{\infty,\mathrm{in}}(\theta,\phi)\,e^{-\mathrm{i}kz\cos\theta}\,e^{\mathrm{i}k\rho\sin\theta\cos(\varphi-\phi)}\sin\theta\,\mathrm{d}\varphi\mathrm{d}\theta. \tag{2.76}$$

In the following, we will assume the incident field is a plane wave polarized at angle $\zeta_{\mathrm{in}}$ with respect to the $x$ axis, i.e. $\mathbf{E}_{\mathrm{in}}(\theta,\phi) = (E_{\mathrm{in}}\cos\zeta_{\mathrm{in}}, E_{\mathrm{in}}\sin\zeta_{\mathrm{in}}, 0)$, and the total incident power is $P_{\mathrm{in}} = \pi F^2 E_{\mathrm{in}}^2 \sin^2\beta_{\mathrm{in}}$. We furthermore assume the scatterer is placed at the origin, and thus driven by the field

$$\mathbf{E}_{0,\mathrm{in}} = -\frac{\mathrm{i}4\pi\epsilon_0 Fe^{-\mathrm{i}kF}}{k^2}\mathscr{A}_0 E_{\mathrm{in}}\begin{pmatrix}\cos\zeta_{\mathrm{in}}\\ \sin\zeta_{\mathrm{in}}\\ 0\end{pmatrix}, \tag{2.77}$$

where

$$\mathscr{A}_0 = \frac{k^3}{4\pi\epsilon_0}\left(\frac{8}{15} - \frac{1}{3}\cos^{3/2}\beta_{\mathrm{in}} - \frac{1}{5}\cos^{5/2}\beta_{\mathrm{in}}\right). \tag{2.78}$$

We consider a scatterer with a highly polarization-dependent response that is maximum along the $x$ axis. In other words, all tensor elements of $\boldsymbol{\alpha}$ except $\alpha_{xx} = \alpha(\omega)$ vanish. Taking the dipolar far field and including the collection angle of the collection lens, we find the scattered field in the output beam:

$$\mathbf{E}_{\mathrm{out,sca}}(\theta,\phi) = \begin{cases}\mathrm{i}\alpha e^{-2\mathrm{i}kF}\mathscr{A}_0 E_{\mathrm{in}}\cos\zeta_{\mathrm{in}}\sqrt{\cos\beta_{\mathrm{in}}}\begin{pmatrix}\sin^2\phi+\cos^2\phi\cos\theta\\ \sin\phi\cos\phi(\cos\theta-1)\\ 0\end{pmatrix}, & \theta\le\beta_{\mathrm{out}}\\ 0, & \theta>\beta_{\mathrm{out}}.\end{cases}$$

Of course, the electric field transmitted through both lenses is simply

$$\mathbf{E}_{\mathrm{out,in}}(\theta,\phi) = \begin{cases}e^{-2\mathrm{i}kF}\mathbf{E}_{\mathrm{in}}(\theta,\phi), & \theta\le\min\{\beta_{\mathrm{in}},\beta_{\mathrm{out}}\}\\ 0, & \theta>\min\{\beta_{\mathrm{in}},\beta_{\mathrm{out}}\},\end{cases} \tag{2.79}$$

and hence the total power in the output beam can be found by integrating the intensity in the output beam as

$$P_{\mathrm{out}} = \frac{1}{2}c\epsilon_0\int_0^{\beta_{\mathrm{out}}}\int_0^{2\pi}\left|\mathbf{E}_{\mathrm{out}}(\theta,\phi)\right|^2 F^2\sin\theta\cos\theta\,\mathrm{d}\phi\mathrm{d}\theta, \tag{2.80}$$

where $\mathbf{E}_{\mathrm{out}}(\theta,\phi) = \mathbf{E}_{\mathrm{out,sca}}(\theta,\phi) + \mathbf{E}_{\mathrm{out,in}}(\theta,\phi)$. The result for $\beta_{\mathrm{out}}\le\beta_{\mathrm{in}}$ is

$$\begin{aligned}P_{\mathrm{out}} = P_{\mathrm{in}}\Big[&\frac{\sin^2\beta_{\mathrm{out}}}{\sin^2\beta_{\mathrm{in}}}\\ &-\mathrm{Im}(\alpha)\mathscr{A}_0\frac{4}{15}\frac{8-5\cos^{3/2}\beta_{\mathrm{out}}-3\cos^{5/2}\beta_{\mathrm{out}}}{\sin^2\beta_{\mathrm{in}}}\cos^2\zeta_{\mathrm{in}}\\ &+|\alpha|^2\mathscr{A}_0^2\left(3+\frac{2}{3}\cos\beta_{\mathrm{out}}+\frac{1}{3}\cos 2\beta_{\mathrm{out}}\right)\frac{\sin^2(\beta_{\mathrm{out}}/2)}{\sin^2\beta_{\mathrm{in}}}\cos^2\zeta_{\mathrm{in}}\Big],\end{aligned} \tag{2.81}$$

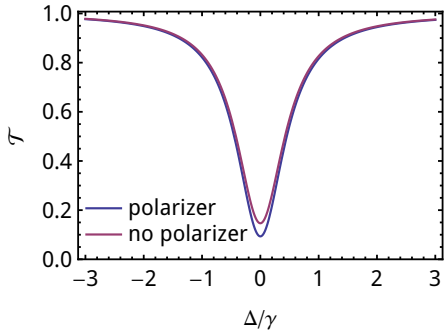


**Figure 2.10:** Transmittance $\mathcal{T}$ for a scatterer with albedo $\mathcal{A} = 1$ and lenses with $\mathrm{NA} = 1$, showing the increase in contrast when adding an analyzer after the collection objective. Red line: no output polarizer. Blue line: with output polarizer. The curves are plotted as a function of detuning $\Delta = \omega - \omega_0$, normalized to linewidth $\gamma$. The beam incident on the first lens is a plane wave.

where we recognize an extinction term scaling linearly with $\mathrm{Im}(\alpha)$ and a scattering term scaling linearly with $|\alpha|^2$. Together with $\partial \mathrm{Im}(\alpha)/\partial x$ and $\partial |\alpha|^2 /\partial x$, which were found in Section 2.3.3, one can now predict the transduction of displacement to optical output power $\frac{\partial P_{\mathrm{out}}}{\partial x}$ by the scatterer.

### 2.3.6 Using an output polarizer

We furthermore consider the scenario where a polarizer is added in the output beam, and the intensity is recorded after this analyzer. By choosing the angles between input polarization, scatterer and analyzer, we can achieve strong suppression of the portion of the transmitted power that does not interact with the scatterer. If the albedo is low, suppressing this background can improve the signal-to-noise ratio.

For input polarization angle $\zeta_{\mathrm{in}}$ between the input field polarization and the $x$ axis, and analyzer angle $\zeta_{\mathrm{out}}$ with respect to the $x$ axis, as shown in Figure 2.9b, the output power is given by

$$P_{\mathrm{out}} = \int_0^{\beta_{\mathrm{out}}} \int_0^{2\pi} \left| \mathbf{E}_{\mathrm{out}}(\theta,\phi) \cdot \left( \hat{x}\cos\zeta_{\mathrm{out}} + \hat{y}\sin\zeta_{\mathrm{out}} \right) \right|^2 F^2 \sin\theta\cos\theta \mathrm{d}\phi \mathrm{d}\theta. \tag{2.82}$$

We again give the result for $\beta_{\text{out}} \leq \beta_{\text{in}}$:

$$\begin{aligned}
P_{\text{out}} = P_{\text{in}}\Big[ & \frac{\sin^2\beta_{\text{out}}}{\sin^2\beta_{\text{in}}}\cos^2(\zeta_{\text{in}}-\zeta_{\text{out}}) \\
& -\text{Im}(\alpha)\mathscr{A}_0\frac{4}{15}\frac{8-5\cos^{3/2}\beta_{\text{out}}-3\cos^{5/2}\beta_{\text{out}}}{\sin^2\beta_{\text{in}}}\cos\zeta_{\text{in}}\cos\zeta_{\text{out}}\cos(\zeta_{\text{in}}-\zeta_{\text{out}}) \\
& +|\alpha|^2\mathscr{A}_0^2\frac{\sin^2(\beta_{\text{out}}/2)}{\sin^2\beta_{\text{in}}}\Big(\frac{3}{2}+\frac{1}{3}\cos\beta_{\text{out}}+\frac{1}{6}\cos 2\beta_{\text{out}}+\frac{5}{4}\cos 2\zeta_{\text{out}} \\
& \quad +\frac{1}{3}\cos(\beta_{\text{out}}-2\zeta_{\text{out}})+\frac{1}{3}\cos(\beta_{\text{out}}+2\zeta_{\text{out}}) \\
& \quad +\frac{1}{24}\cos(2\beta_{\text{out}}-2\zeta_{\text{out}})+\frac{1}{24}\cos(2\beta_{\text{out}}+2\zeta_{\text{out}})\Big)\Big].
\end{aligned} \tag{2.83}$$

We note that for $\zeta_{\text{out}} = 0$ and $\zeta_{\text{in}} = 0$, the resulting transmitted power is marginally different from that without an analyzer: for large albedo and strong focusing, the extinction is increased by a few percent by adding the analyzer. This result is shown in Figure 2.10, which shows the transmittance for a scatterer with albedo $\mathscr{A} = 1$ and lenses with NA = 1, both without output analyzer (Equation (2.81)) and including an output analyzer (Equation (2.83)), which is aligned with the input polarization and scatterer ($\zeta_{\text{in}} = \zeta_{\text{out}} = 0$). This change in transmittance through adding an analyzer is caused by high-angle components of the scattered dipole field that are not polarized along $\hat{x}$. The extinction dip does not go to 1 (both with and without output polarizer) due to the non-dipolar components of the incident light field at the scatterer's position.

Of course, for other angles the effect is pronounced: the two polarizers can strongly suppress either the non-scattered background field or the scattered field, leading to a strongly polarizer-angle dependent transmittance. Figure 2.11a shows the transmittance as a function of detuning for scatterers with an albedo of 1. The crossed-polarizer transmission is at $\zeta_{\text{in}} = -\pi/4$, $\zeta_{\text{out}} = +\pi/4$. At $\zeta = 0.20\pi$, the scattering and extinction are exactly matched, so neither an extinction dip nor a scattering peak are visible. The height of the scattering peak for $\zeta_{\text{out}} = -\zeta_{\text{in}} = \pi/4$ is exactly four times smaller than the depth of the extinction dip for $\zeta_{\text{out}} = \zeta_{\text{in}} = 0$. In the situation we are describing now, a factor of 2 is due to the 45° angle between input polarizer and scatterer, and another factor of 2 is due to the 45° between the scattered light and the analyzer. We see that $\mathscr{T}$ and $|\partial\mathscr{T}/\partial x|$ show different scaling with polarizer angles, indicating that, depending on the properties of the scatterer, carefully choosing polarizer angles can improve the sensitivity of motion transduction, as the measured *signal* will scale with $\partial\mathscr{T}/\partial x$ but various *noise* contributions with $\mathscr{T}$.

In Figure 2.11b, we show the change in transmittivity $\mathscr{T}$ and the absolute value of the change in transmittivity $|\partial\mathscr{T}/\partial x|$ for $\delta x = 1$ nm as a function of polarizer angles $-\zeta_{\text{in}} = \zeta_{\text{out}}$, for a scatterer with $\mathscr{A} = 1$ at optimum detuning $\Delta = \frac{1}{2\sqrt{3}}\gamma$, with $G = 2\pi \times 1$ THz/nm and NA = 1. In Figure 2.11c, we again plot $\mathscr{T}$ and $|\partial\mathscr{T}/\partial x|$, this time for a scatterer with a low albedo $\mathscr{A} = 0.05$. We can see that $|\partial\mathscr{T}/\partial x|$ has a

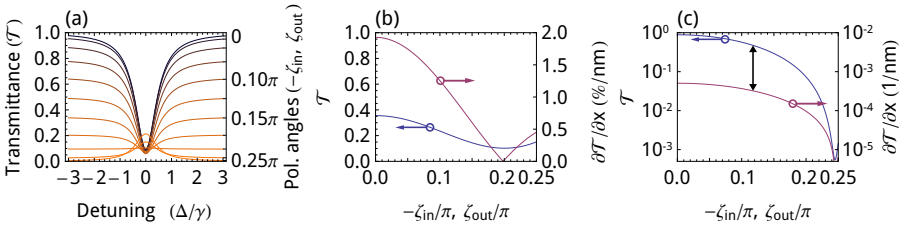


**Figure 2.11:** (a): Transmittance as a function of detuning for a range of polarizer angles, indicated along the right vertical axis. Albedo $\mathscr{A} = 1$, polarizer angles range from 0 to $\pm\pi/4$ in steps of $0.05\pi$. The top dark blue curve is for $\zeta_{in} = \zeta_{out} = 0$, the bottom orange line is for crossed polarizers with $\zeta_{in} = -\pi/4$ and $\zeta_{out} = \pm\pi/4$. (b): Transmittance $\mathcal{T}$ (blue) and derivative $\frac{\partial\mathcal{T}}{\partial x}$ (purple) for a scatterer with $\mathscr{A} = 1$ and optimum detuning. (c): Transmittance $\mathcal{T}$ (blue) and derivative $\left|\frac{\partial\mathcal{T}}{\partial x}\right|$ (purple) plotted on a logarithmic scale, for $\mathscr{A} = 0.05$ and optimum detuning. Note the different scaling of $\mathcal{T}$ and $\left|\frac{\partial\mathcal{T}}{\partial x}\right|$ with polarizer angles: for the low albedo scatterer, $|\partial\mathcal{T}/\partial x|$ has a much slower decrease with increasing $\zeta$ than the transmittivity $\mathcal{T}$.

weaker reduction with increasing polarizer angle $\zeta$ than $\mathcal{T}$: the difference between $|\partial\mathcal{T}/\partial x|$ and $\mathcal{T}$, indicated by the black arrow, becomes smaller. Therefore, for scatterers with low albedo, using crossed polarizers can increase sensitivity. We will also later show, in Figure 2.16, that measuring transduction from scatterers with non-optimal detuning can benefit from using crossed polarizers.

## 2.4 Transduction & conversion

We next calculate how the spectral density of motion, $S_{xx}^{th}$, is converted to $P_{ESA}$, the power we measure on an electronic spectrum analyzer, and describe the various noise sources that are added to this signal. These noise sources, taken together, cause an imprecision background, which imposes a limit on the sensitivity of the measurement. In this section, we will identify the relevant contributions to the imprecision in this implementation of motion transduction and the scaling of these contributions with optical power.

The laser beam that is modulated by the plasmon-mechanical transducer is not free of noise: it has laser classical noise and quantum shot noise components. The total optical signal, modulated by mechanical fluctuations and noise fluctuations, is converted to a photocurrent in a photodiode, amplified in a transimpedance amplifier, where electronic amplifier noise is added to the total signal, and then converted to an electronic power in an electronic spectrum analyzer. In this section, we will show the transfer functions for each of these steps and determine the noise power spectral densities.

### 2.4.1 Transduction of mechanical motion

To convert the displacement spectral density to an (optical) power spectral density, we have to find the transduction function as defined in Equation (2.33). This transduction function is determined by the change in transmittance as a function of $x$:

$$\delta P_{\text{out}} = P_{\text{in}} \frac{\partial \mathcal{T}}{\partial x} \delta x. \tag{2.84}$$

The power spectral density of the transmitted light due to mechanical fluctuations is thus:

$$S_{\text{PP}}^{\text{x}} = P_{\text{in}}^2 \left( \frac{\partial \mathcal{T}}{\partial x} \right)^2 S_{\text{xx}}^{\text{th}}(\Omega), \tag{2.85}$$

where the subscript P refers to (fluctuations of) the optically transmitted power $P_{\text{out}}$. To calculate $\frac{\partial \mathcal{T}}{\partial x}$, we start from Equation (2.83). The only terms that have a dependence on $x$ in this equation are the $\text{Im}(\alpha)$ and the $|\alpha|^2$ terms. By replacing these with their derivatives, which are shown in Equations (2.66) and (2.67), we obtain $\frac{\partial \mathcal{T}}{\partial x}$.

### 2.4.2 Noise sources

We identify three major sources of noise in our experiment: electrical noise, classical laser noise and quantum shot noise of the detected laser light. These have different power and frequency depencies, which implies that there is an optimum choice for detection schemes to reduce the noise contributions. We will add the three contributions in the optical power spectral density, as

$$S_{\text{PP}}^{\text{tot}}(\Omega) = \sum_i S_{\text{PP}}^i(\Omega) \tag{2.86}$$

$$= S_{\text{PP}}^{\text{x}}(\Omega) + S_{\text{PP}}^{\text{SN}} + S_{\text{PP}}^{\text{class}}(\Omega) + S_{\text{PP}}^{\text{el}}. \tag{2.87}$$

In this section, we will determine the magnitude of these noise contributions.

#### Shot noise

Shot noise is an intrinsic effect related to quantum fluctuations of the light field. We can quantify its amplitude by considering a stream of photons arriving at random times:

$$\dot{N}(t) = \sum_j \delta(t - t_j) \tag{2.88}$$

where $t_j$ are the random arrival times of the photons. If we detect $N$ photons in a time $T$:

$$N = \int_0^T \mathrm{d}t \dot{N}(t), \tag{2.89}$$

defining an average number arriving per unit time as $\bar{\dot{N}}$, the autocorrelation function of the photon flux $\dot{N}$ is

$$\left\langle \dot{N}(t)\dot{N}(0)\right\rangle = \lim_{T\to\infty}\frac{1}{T}\sum_j\sum_{j'}\int_{-T/2}^{T/2}\mathrm{d}t'\delta(t'-t_j)\delta(t'-t_{j'}+t) \tag{2.90}$$

$$= \lim_{T\to\infty}\frac{1}{T}\sum_j\sum_{j'}\delta(t_j-t_{j'}+t). \tag{2.91}$$

If $T$ is large, the autocorrelation becomes $\left\langle \dot{N}(t)\dot{N}(0)\right\rangle = \bar{\dot{N}}\delta(t)$: only those terms for which $j = j'$ contribute to the summation, for a total of $N\delta(t) = \bar{\dot{N}}T\delta(t)$. The Wiener–Khinchin theorem then gives the spectral density of photon numbers:

$$S_{\dot{N}\dot{N}} = \bar{\dot{N}}, \tag{2.92}$$

with units $\mathrm{Hz}^2/\mathrm{Hz}$, which we can convert to a power $P(t) = \hbar\omega\dot{N}(t)$. We then obtain a shot noise power spectral density:

$$S_{\mathrm{PP}}^{\mathrm{SN}} = (\hbar\omega)^2 S_{\dot{N}\dot{N}}(\Omega) = \hbar\omega P_{\mathrm{out}}. \tag{2.93}$$

#### Electrical noise

Electrical noise is generated in the photodiode's transimpedance amplifier, and is independent of optical power and detection frequency. The amplifier noise is defined as a noise-equivalent-power: $\mathrm{NEP} \equiv \sqrt{S_{\mathrm{P}}^{\mathrm{el}}} = \sqrt{2S_{\mathrm{PP}}^{\mathrm{el}}}$. $S_{\mathrm{PP}}^{\mathrm{el}}$ is the optical power spectral density which, after conversion to electrical current spectral density, is equal in amplitude to the electrical noise (signal-to-noise ratio is 1). For the photodiode we use (Femto HCA-S-200M-IN) we determined a NEP of -138.5 dBm/Hz on the electronic spectrum analyzer.

Using the inverse of equations (2.102) and (2.104) along with the experimental parameters $\xi_{\mathrm{det}}$ and $\xi_{\mathrm{amp}}$ we can determine a NEP of $4.38\,\mathrm{pW}/\sqrt{\mathrm{Hz}}$, to get a power spectral density

$$S_{\mathrm{PP}}^{\mathrm{el}} = 2\,\mathrm{NEP}^2. \tag{2.94}$$

Note that while this is expressed as an optical power spectral density, the electronic noise is not actually present until after the transimpedance amplifier.

#### Laser classical noise

The laser classical noise can be split into two contributions: intensity fluctuations and phase fluctuations. While the intensity fluctuations can be directly measured, the phase fluctuations require e.g. an optical cavity or a scatterer to be converted to observable intensity fluctuations.

The main source of classical intensity laser noise in the laser used for most of the experiments (NKT Koheras E15 EDFL) is relaxation oscillations in the laser, where power is exchanged between the laser cavity and the gain medium. This noise is

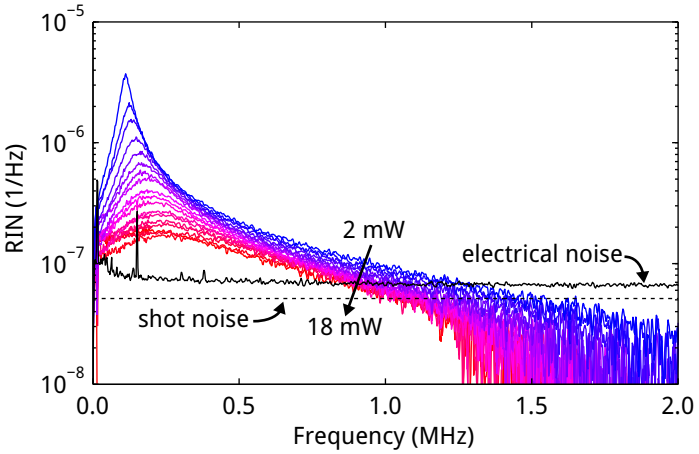


**Figure 2.12:** Measured laser classical noise caused by relaxation oscillations between the gain medium ($Er^{3+}$ ions) and the laser fiber cavity. The laser classical noise is expressed as relative intensity noise (RIN). The different curves are for different drive powers. An attenuator was used to keep the laser power on the photodiode constant at 50 μW. The black solid line indicates the electrical noise, the dashed black line indicates the shot noise.

strongly peaked around 300 kHz, tailing off at higher frequencies. This also drove the choice of length of our oscillators: we designed the length to give a mechanical resonance frequency much higher than the typical laser noise band. The classical noise on the spectrum analyzer scales as $P_{\text{out}}^2$:

$$S_{\text{PP}}^{\text{class}} = (P_{\text{out}}\text{RIN})^2 = P_{\text{in}}^2 \mathscr{T}^2 \text{RIN}^2, \tag{2.95}$$

where RIN is the relative intensity noise, with units of 1/Hz. The RIN can also be converted to a log scale, and then has units of dBc/Hz (decibels relative to the carrier per Hertz bandwidth).

The laser classical noise is also dependent on the drive power of the laser [3]. The measured laser classical noise for our laser is shown in Figure 2.12. The figure also shows the electrical noise caused by the amplifier and the photon shot noise. The electrical noise was measured by blocking the laser beam from the photodiode. The shot noise has an optical power spectral density $\sqrt{S_{\text{PP}}^{\text{SN}}} = \sqrt{\hbar\omega P_{\text{out}}}$, which for the detected power of 50 μW is calculated to be $\sqrt{S_{\text{PP}}^{\text{SN}}} = 2.58 \times 10^{-12}\ \text{W}/\sqrt{\text{Hz}}$. The resulting noise floor of $S_{\text{PP}}^{\text{SN}} + S_{\text{PP}}^{\text{el}}$ was subtracted from the other traces. For all the measurements, the drive power was attenuated by rotating a linear polarizer to achieve a detected power of 50 μW. Note that for constant detector power it is better to have the laser running at full power with an attenuator rather than setting a lower power on the laser.

### Laser classical phase noise

The laser also has phase fluctuations. We can express the laser light field as [93],

$$a(t) = \sqrt{I(t)}e^{\mathrm{i}(\omega t+\phi(t))}, \tag{2.96}$$

where $I(t)$ is the fluctuating intensity and $\phi(t)$ is the fluctuating phase, where we set $\langle\phi(t)\rangle = 0$. Then the spectral density of phase fluctuations is, by the Wiener–Khinchin theorem,

$$S_{\phi\phi} = \frac{1}{2\pi}\int_{-\infty}^{\infty} e^{\mathrm{i}\omega t}\langle\phi(t)\phi(0)\rangle\,\mathrm{d}t. \tag{2.97}$$

The instantaneous laser frequency can be determined from the instantaneous phase:

$$\omega(t) = \frac{\mathrm{d}\left[\phi_0+\phi(t)\right]}{\mathrm{d}t} = \dot{\phi}(t), \tag{2.98}$$

leading to an expression for the frequency noise spectral density:

$$S_{\omega\omega}(\Omega) = S_{\dot{\phi}\dot{\phi}}(\Omega) = \omega^2 S_{\phi\phi}(\Omega) \tag{2.99}$$

This expresses the frequency noise as an angular frequency. The equivalent expression for frequency, expressed in Hertz, is $S_{\nu\nu} = S_{\phi\phi}/(4\pi^2)$. The frequency noise is converted to optical power spectral density by the scatterer:

$$S^{\omega}_{\mathrm{PP}}(\Omega) = P^2_{\mathrm{in}}\left(\frac{1}{G}\frac{\partial\mathcal{T}}{\partial x}\right)^2 S_{\omega\omega}(\Omega). \tag{2.100}$$

The factor of $1/G$ is included due to our definition of $\frac{\partial\mathcal{T}}{\partial x}$, with $P^2_{\mathrm{in}}\left(\frac{\partial\mathcal{T}}{\partial x}\right)^2$ the transduction function between $S_{\mathrm{xx}}$ and $S_{\mathrm{PP}}$. The optomechanical frequency shift $G$ links the displacement spectral density to the scatterer's central frequency spectral density: $S_{\mathrm{xx}} = G^2 S_{\omega\omega}$. Therefore, we divide by $1/G^2$ in Equation (2.100) to calculate the transduction function between $S_{\omega\omega}$ and $S_{\mathrm{PP}}$.

This also allows us to calculate the imprecision spectral density due to laser phase fluctuations:

$$S^{\mathrm{imp},\phi}_{\mathrm{xx}}(\Omega) = \frac{1}{G^2}S_{\omega\omega}(\Omega) = \frac{\Omega^2}{G^2}S_{\phi\phi}(\Omega). \tag{2.101}$$

By using the parameters shown in Table 2.3, we can compare the power spectral density of transduced phase noise to the electrical noise of the photodiode. We will assume optimal detuning for the optimal scatterer defined earlier, and find $\sqrt{S^{\phi}_{\mathrm{PP}}} = 6.6\ \mathrm{fW}/\sqrt{\mathrm{Hz}}$ for an input power $P_{\mathrm{in}} = 500\ \mu\mathrm{W}$. This is 3 orders of magnitude smaller than the electrical noise-equivalent-power (see Table 2.3). Therefore, we will in the remainder of this thesis assume that laser phase noise can be neglected compared to the other noise sources described in this section.

We note that for many cavity optomechanical experiments, laser phase noise can be a limiting factor [22, 94, 95]. In these experiments, $G$ is much smaller, but the cavity loss rate $\kappa$ is also much smaller, leading to a much stronger transduction of frequency fluctuations.

In other words, our experimental geometry strongly transduces mechanical displacements to frequency fluctuations, while having a much weaker transduction of frequency fluctuations to intensity fluctuations. In the cavity optomechanical case, this is usually reversed, with much weaker transduction from displacement to frequency, and very strong transduction of frequency fluctuations to intensity fluctuations. This strong frequency-to-intensity transduction necessarily also transduces the laser phase noise.

### 2.4.3 Electrical conversion

The photodiode converts the optical power to a photocurrent, $I_{\mathrm{out}} = \xi_{\mathrm{det}} P_{\mathrm{out}}$. The conversion efficiency $\xi_{\mathrm{det}}$ (in A/W) includes the quantum efficiency and the photon energy, and is therefore wavelength dependent. The total current spectral density is then

$$S_{\mathrm{II}}(\Omega) = \xi_{\mathrm{det}}^2 \left[ S_{\mathrm{PP}}^{\mathrm{x}}(\Omega) + S_{\mathrm{PP}}^{\mathrm{SN}} + S_{\mathrm{PP}}^{\mathrm{class}}(\Omega) + S_{\mathrm{PP}}^{\mathrm{el}} \right].$$

The photodiode has a built-in transimpedance amplifier, which converts the photocurrent to a voltage:

$$S_{\mathrm{VV}}(\Omega) = \xi_{\mathrm{amp}}^2 S_{\mathrm{II}}(\Omega),$$

in $\mathrm{V}^2/\mathrm{Hz}$. Finally, the voltage spectral density is read out on a spectrum analyzer with impedance $R$ to produce power

$$P_{\mathrm{ESA}} = \frac{V^2}{R} = \frac{\xi_{\mathrm{amp}}^2 \xi_{\mathrm{det}}^2}{R} S_{\mathrm{PP}}. \tag{2.102}$$

This electrical power $V(t)$ is filtered around $\Omega$ by the ESA's resolution bandwidth (RBW). If the signal is flat on the scale of the RBW, the displayed power is

$$P_{\mathrm{ESA}} = \mathrm{RBW} \frac{S_{\mathrm{V}}^{\mathrm{total}}}{R} = \mathrm{RBW} \frac{2 S_{\mathrm{VV}}^{\mathrm{total}}}{R}. \tag{2.103}$$

This is typically displayed on a dBm scale:

$$P_{\mathrm{ESA}}(\mathrm{dBm}) = 10 \log_{10} \left( P_{\mathrm{ESA}}(W) \cdot 1000 \right). \tag{2.104}$$

Table 2.3 shows the relevant parameters for equipment used in the experiments described in this thesis.

| device | parameter | symbol | value | units |
|---|---|---|---|---|
| laser: NKT Koheras Adjustik E15 | relative intensity noise | RIN | $7.4 \times 10^{-8}$ | 1/Hz (@ 10 MHz) |
| | frequency noise spectral density | $S_{\nu\nu}^{1/2}(\Omega)$ | 13 | Hz/$\sqrt{\text{Hz}}$ (@ 1 MHz) |
| photodiode: Femto HCA-S-200M-IN | conversion efficiency | $\xi_{\text{det}}$ | 0.95 | A/W ($\lambda$ = 1550 nm) |
| | transimpedance gain | $\xi_{\text{amp}}$ | $2 \times 10^4$ | V/A |
| | noise-equivalent-power | NEP | 4.38 | pW/$\sqrt{\text{Hz}}$ |
| ESA: Rohde & Schwarz FSV-3 | impedance | $R$ | 50 | $\Omega$ |
| | resolution bandwidth | RBW | 300 (typ) | Hz |

**Table 2.3:** Experimental parameters for conversion of power spectral density $S_{\text{PP}}$ to electronic spectrum analyzer power $P_{\text{ESA}}$.

## 2.5 Displacement sensitivity

We can now compare the tranduced signal to the various noise sources. We can define the imprecision displacement spectral density:

$$\begin{aligned} S_{\text{xx}}^{\text{imp}}(\Omega) &= \frac{1}{P_{\text{in}}^2(\partial\mathcal{T}/\partial x)^2} S_{\text{PP}}^{\text{imp}}(\Omega) \\ &= \frac{1}{P_{\text{in}}^2(\partial\mathcal{T}/\partial x)^2} \left(2\text{NEP}^2 + \hbar\omega P_{\text{in}}\mathcal{T} + \text{RIN}^2 P_{\text{in}}^2 \mathcal{T}^2\right) + \frac{1}{G^2} S_{\omega\omega}(\Omega) \end{aligned} \tag{2.105}$$

which is the imprecision added to the motion transduction by the various noise sources. This forms a limit to the sensitivity with which we can measure $S_{\text{xx}}^{\text{th}}(\Omega)$. We can identify two major power regimes: one where the input power $P_{\text{in}}$ is fixed and one where the power at the detector $P_{\text{out}}$ is fixed.

The input power can be limited because of for instance demands on the laser power or a limited damage threshold power at the scatterer.

In other cases, one is instead constrained by the power at the detector rather than by $P_{\text{in}}$, for instance due to photodiode or transimpedance amplifier saturation. Then, the imprecision for a given value of $P_{\text{out}}$ is the proper figure of merit for the transducer's performance.

In the figures in this section, we will not plot the phase noise imprecision contribution, as shown in Equation (2.101). For the phase noise as given in Table 2.3, with $S_{\nu\nu}^{1/2} = 13\ \text{Hz}/\sqrt{\text{Hz}}$, we can find an imprecision $\sqrt{S_{\text{xx}}^{\text{imp},\phi}} = 1.3 \times 10^{-20}\ \text{m}/\sqrt{\text{Hz}}$. This is much smaller than the thermal occupation of a typical mechanical oscillator we will use, as shown for instance in Figure 2.5, and also much smaller than the other imprecision contributions, as will be shown in the remainder of this section.

We will investigate the imprecision levels for two cases: a high-albedo scatterer and a low-albedo scatterer. Figure 2.13 shows the scattering and extinction cross sections for these scatterers. Both scatterers have optical quality factor $Q_{\text{opt}} = 10$ and will be used at optimum detuning $\Delta = \omega - \omega_0 = \frac{1}{2\sqrt{3}}\gamma$, with $G = 2\pi \times 1$ THz/nm. For the high-$\mathscr{A}$ scatterer we will use an excitation and collection NA = 1 and albedo

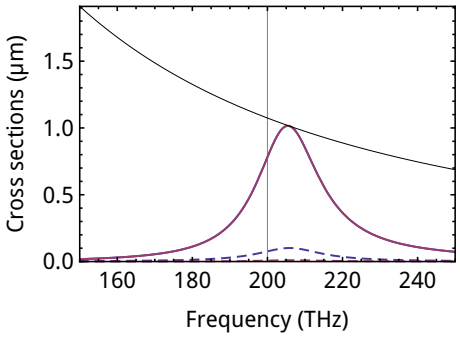


**Figure 2.13:** Extinction (blue) and scattering (purple) cross sections for a high-$\mathscr{A}$ scatterer (albedo $\mathscr{A} = 1$, solid line) and a bad scatterer (albedo $\mathscr{A} = 0.1$, dashed lines), with the unitary limit plotted in black. Note that for the scatterer with albedo $\mathscr{A} = 1$ the extinction and scattering cross section are identical. Both scatterers have $Q_{\text{opt}} = 10$. The gray vertical line indicates the laser frequency $\omega = 2\pi \times 200$ THz.

$\mathscr{A} = 1$, for the low-$\mathscr{A}$ scatterer we will use a limited numerical aperture of NA = 0.4 and $\mathscr{A} = 0.1$.

### 2.5.1 Imprecision for limited input power $P_{\text{in}}$

For fixed input power $P_{\text{in}}$, the imprecision is determined by Equation (2.105). Figure 2.14 shows this fixed-input-power imprecision $S_{xx}^{\text{imp}}(\Omega)$ as a function of polarizer angles, using the noise parameters tabulated in Table 2.3 and an input power of 500 μW. The different noise contributions to the imprecision are also plotted. Figure 2.14a shows the data for the scatterer with $\mathscr{A} = 1$, while Figure 2.14b shows the data for the scatterer with $\mathscr{A} = 0.1$. First, it is obvious that the total imprecision is much lower for the good scatterer.

Second, both scatterers show an angle where the imprecision diverges. This is the angle where the scattering peak is exactly equal to the extinction dip, leading to a net 0 transduction, as shown in Figure 2.11 for the high-$\mathscr{A}$ scatterer, where in Figure 2.11a the line for $\zeta = \pm 0.2\pi$ is flat, and in Figure 2.11b the change in transmittivity $\frac{\partial \mathscr{T}}{\partial x}$ is equal to 0. As this angle depends on the scattering properties, it is shifted for the low-$\mathscr{A}$ scatterer shown in Figure 2.14b, moving closer to $\zeta = \pm\pi/4$.

For the high-$\mathscr{A}$ scatterer, using crossed polarizers does not improve sensitivity: the reduction in detected power by using crossed polarizers due to Malus' law increases the classical and shot noise contributions.

Near the crossed-polarizer angle ($\zeta = \pm\pi/4$), the laser classical noise contribution to the imprecision for the low-$\mathscr{A}$ scatterer is strongly suppressed, leading to a reduction in imprecision. At these angles, the bad-scatterer-imprecision is dominated by the electrical contribution, as this does not scale with the transmittance

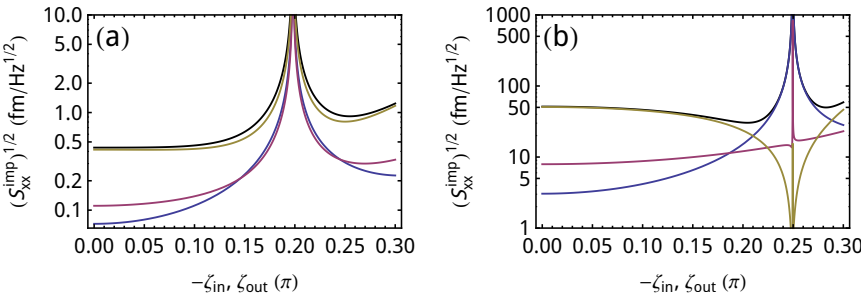


**Figure 2.14:** Imprecision for constant input power $P_{in}$ as a function of polarizer angles, with $\zeta_{in} = -\zeta_{out}$. (a): Imprecision for a scatterer with $\mathscr{A} = 1$ and NA = 1. (b): Imprecision for a scatterer with $\mathscr{A} = 0.1$ and NA = 0.4. Lines indicate the various imprecision contributions (Equation (2.105)); black: total imprecision; blue: electrical imprecision; purple: shot noise imprecision; gold: classical noise imprecision. For both panels, $Q_{opt} = 10$, $G = 2\pi \times 1$ THz/nm, $\omega_0 = 2\pi \times 210$ THz, $\omega = 2\pi \times 200$ THz, to achieve optimum detuning of $\Delta = \omega - \omega_0 = \frac{1}{2\sqrt{3}}\gamma$. Imprecisions are calculated for $P_{in} = 500$ μW.

$\mathscr{T}$, which is strongly reduced at crossed polarizer angles. We note however that with proper optical amplification (either using an EDFA or beating with a local oscillator) could reduce its contribution significantly.

### 2.5.2 Imprecision for limited output power $P_{out}$

For the limited output power regime, we can rewrite Equation (2.105) to reflect the limiting output power:

$$\begin{aligned} S_{xx}^{imp}(\Omega) &= \frac{2\,\mathrm{NEP}^2}{P_{out}^2}\frac{\mathscr{T}^2}{(\partial\mathscr{T}/\partial x)^2} + \frac{\hbar\omega}{P_{out}}\frac{\mathscr{T}^2}{(\partial\mathscr{T}/\partial x)^2} + \mathrm{RIN}^2\frac{\mathscr{T}^2}{(\partial\mathscr{T}/\partial x)^2} \\ &= \frac{\mathscr{T}^2}{(\partial\mathscr{T}/\partial x)^2}\left[\frac{2\,\mathrm{NEP}^2}{P_{out}^2} + \frac{\hbar\omega}{P_{out}} + \mathrm{RIN}^2\right], \end{aligned} \tag{2.106}$$

separating out $\mathscr{T}$ and $\frac{\partial\mathscr{T}}{\partial x}$ from the noise parameters.

Figure 2.15 shows the fixed-output-power imprecision for a detected power of 50 μW. As can be seen from Equation 2.106, all three imprecision contributions have the same scaling with polarizer angles, as these angles only enter into $\mathscr{T}$ and $\frac{\partial\mathscr{T}}{\partial x}$. Again, as in Figure 2.14, we plot data for an $\mathscr{A} = 1$ and for an $\mathscr{A} = 0.1$ scatterer. For limiting $P_{out}$, as for limiting $P_{in}$ crossed polarizers do not increase the sensitivity for the high-$\mathscr{A}$ scatterer. For the low-$\mathscr{A}$ scatterer however, we see that the imprecision is greatly reduced near the crossed-polarizer angle.

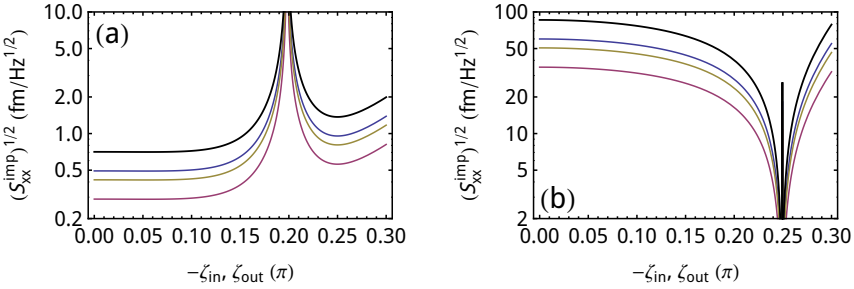


**Figure 2.15:** Imprecision for constant output power $P_{\mathrm{out}}$ as a function of polarizer angles, with $\zeta_{\mathrm{in}} = -\zeta_{\mathrm{out}}$. (a): Imprecision for a scatterer with $\mathscr{A} = 1$ and NA = 1. (b): Imprecision for a scatterer with $\mathscr{A} = 0.1$ and NA = 0.4. Lines indicate the various imprecision contributions (Equation (2.106)); black: total imprecision; blue: electrical imprecision; purple: shot noise imprecision; gold: classical noise imprecision. For both panels, $Q_{\mathrm{opt}} = 10$, $G = 2\pi \times 1$ THz/nm, $\omega_0 = 2\pi \times 210$ THz, $\omega = 2\pi \times 200$ THz, to achieve optimum detuning of $\Delta = \omega - \omega_0 = \frac{1}{2\sqrt{3}}\gamma$. Imprecisions are calculated for $P_{\mathrm{out}} = 50$ μW.

### 2.5.3 Imprecision as a function of detuning

So far, we have only studied the polarizer-angle dependence of the imprecision, while setting the laser at the optimum detuning on the slope of the resonance. In Figure 2.16, we calculate the imprecision as a function of detuning relative to the peak resonance frequency. We compare the total imprecision $S_{xx}^{\mathrm{imp}}$ for scatterers with $\mathscr{A} = 1$ both with constant $P_{\mathrm{in}}$ (Figure 2.16a) and with constant $P_{\mathrm{out}}$ (Figure 2.16b), for $\zeta_{\mathrm{in}} = \zeta_{\mathrm{out}} = 0$ and $\zeta_{\mathrm{in}} = \zeta_{\mathrm{out}} = \pi/4$, finding that for larger detunings, using crossed polarizers has a lower imprecision than using aligned polarizers. The crossing points are at $\Delta/\gamma = -0.4, +0.49$ for constant $P_{\mathrm{in}}$, and at $\Delta/\gamma = -0.45, +0.55$ for constant $P_{\mathrm{out}}$.

We see that for good scattering and optimal detuning, a very low imprecision can be achieved without using crossed polarizers. However, when the scattering is small or the detuning is large, the crossed polarizers can be a useful way to suppress noise sources that scale with the transmittance $\mathscr{T}$.

### 2.5.4 Experimental techniques to reduce noise

There are other experimental techniques to reduce noise levels and thereby improve sensitivity. A commonly used technique is homodyne interferometry [3]. Instead of the direct transduction used in this thesis, the laser is tuned to the center of the optical resonance. The mechanical oscillations then imprint phase fluctuations onto the transmitted laser beam. This light is then interfered with a

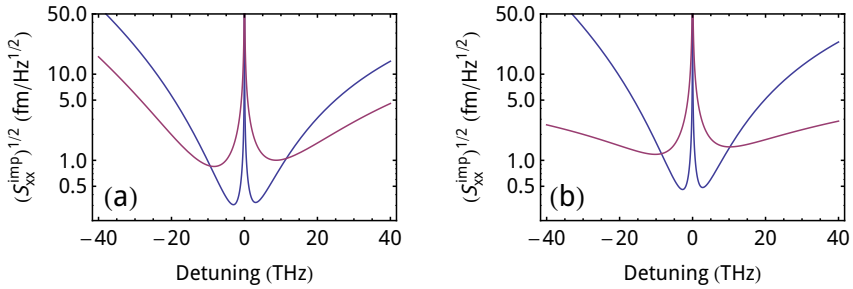


**Figure 2.16:** Imprecision for an $\mathscr{A} = 1$, NA = 1, $G = 2\pi \times 1$ THz/nm scatterer as a function of detuning. (a): Imprecision for constant $P_{\text{in}} = 500$ μW. (b): Imprecision for constant $P_{\text{out}} = 50$ μW. Blue: $\zeta_{\text{in}} = \zeta_{\text{out}} = 0$, purple: $-\zeta_{\text{in}} = \zeta_{\text{out}} = \pi/4$.

much stronger homodyne reference branch and split to two balanced photodiodes, and the difference signal is monitored. The interference with the strong local oscillator can effectively amplify weak signals, and the interferometer suppresses common-mode classical noise. However, it does require a properly stabilized and arm-length-matched Mach–Zender interferometer.

If the imprecision is limited by electrical or shot noise, an optical amplifier (for instance an erbium-doped fiber amplifier (EDFA) when working at telecom wavelengths) can be used after the scatterer and before the photodiode to amplify the signal, increasing the total power at the photodiode, and thereby reducing the electrical and shot noise imprecision. The EDFA will not improve the classical noise imprecision, as this has the same scaling with optical power as the signal. An EDFA also adds noise itself, with this "excess amplifier noise" typically adding on the order of 6 dB of noise to the shot noise level, implying that it is dependent on the ratios of the imprecision contributions whether or not using an EDFA will improve sensitivity.

## 2.6 Transduction examples

In this section, we will calculate the sensitivity achievable using our plasmonic transducer geometry. We will assume this geometry can be realized in a system with mechanical properties demonstrated by two other groups: a low frequency, high-$Q$ silicon nitride string oscillator, demonstrated by Verbridge et al. [96], and a high frequency, low-$Q$ silicon carbide oscillator, demonstrated by Yang et al. [97]. Finally, we will investigate the properties of a beam similar to the beams we will study in Chapter 6. As many imprecision contributions scale with the optical power used, we will plot the imprecisions as a function of input power $P_{\text{in}}$.

This section will use the the high-$\mathscr{A}$ scatterer as seen in the previous section

| beam | $f$ (MHz) | $Q$ | $m_{\mathrm{eff}}$ | $L$ (μm) | $w$ (nm) | $h$ (nm) | $T$ (K) |
|---|---|---|---|---|---|---|---|
| Verbridge | 1.03 | $1.3 \cdot 10^6$ | 110 pg | 275 | 350 | 110 | 300 |
| Yang | 190 | 5000 | 96 fg | 2.3 | 150 | 100 | 4.2 |
| 10 MHz | 10 | 1000 | 160 fg | 10 | 120 | 100 | 300 |

**Table 2.4:** Parameters for the mechanical oscillators described in Section 2.6.

for transduction, with parameters: $\mathscr{A} = 1$, NA = 1, $Q_{\mathrm{opt}} = 10$, $G = 2\pi \times 1$ THz/nm, $\omega_0 = 2\pi \times 210$ THz, $\omega = 2\pi \times 200$ THz, operating at an optimum detuning of $\Delta = \omega - \omega_0 = \frac{1}{2\sqrt{3}}\gamma$.

### 2.6.1 Imprecision comparable to that at the standard quantum limit

We can also calculate the power needed to achieve an imprecision equal to that at the *standard quantum limit*.

In an ideal, lossless, quantum-limited measurement, the total noise added by the measurement (i.e. imprecision plus measurement back-action) reaches a minimum at a certain power, when

$$\bar{S}_{\mathrm{xx}}^{\mathrm{imp}} = \bar{S}_{\mathrm{xx}}^{\mathrm{qba}} = \frac{1}{2}\bar{S}_{\mathrm{xx}}^{\mathrm{ZPF}}, \tag{2.107}$$

the so-called standard quantum limit (SQL). Here, $\bar{S}_{\mathrm{XX}}(\Omega)$ denotes the symmetrized spectral density: $\bar{S}_{\mathrm{XX}}(\Omega) \equiv \left(S_{\mathrm{XX}}(\Omega) + S_{\mathrm{XX}}(-\Omega)\right)/2$. $\bar{S}_{\mathrm{xx}}^{\mathrm{ZPF}}$ is the spectral displacement density associated with the quantum-mechanical ground state. At the mechanical resonance frequency, this is equal to

$$\bar{S}_{\mathrm{xx}}^{\mathrm{ZPF}}(\Omega_{\mathrm{m}}) = \hbar \left|\mathrm{Im}\chi_{\mathrm{xx}}(\Omega_{\mathrm{m}})\right| = \frac{\hbar}{m_{\mathrm{eff}}\Omega_{\mathrm{m}}\Gamma_{\mathrm{m}}}. \tag{2.108}$$

The (quantum) back-action $\bar{S}_{\mathrm{xx}}^{\mathrm{qba}}$ is caused by the fluctuating radiation pressure force. The force spectral density of this back-action is the force per photon squared, $(\hbar G)^2$, times the photon number spectral density:

$$\bar{S}_{\mathrm{FF}}^{\mathrm{qba}} = \hbar^2 G^2 \bar{S}_{\mathrm{NN}} = \frac{4\hbar^2 G^2}{\gamma}\bar{n}_{\mathrm{phot}}, \tag{2.109}$$

where the number of photons circulating in the cavity is estimated to be

$$\bar{n}_{\mathrm{phot}} = \frac{k}{\epsilon_0}\frac{\mathrm{Im}(\alpha)}{\mathscr{A}_0}\frac{4P_{\mathrm{in}}}{\gamma\hbar\omega}, \tag{2.110}$$

where $\mathscr{A}_0$ is the effective focal area from Equation (2.78).

The back-action force spectral density causes additional displacement of the mechanical resonator:

$$\bar{S}_{xx}^{qba} = \left|\chi_{xx}(\Omega)\right|^2 \bar{S}_{FF}^{qba}, \tag{2.111}$$

where $\chi_{xx}(\Omega)$ is the mechanical susceptibility as defined in Equation (2.35). For measurement at the optical cavity resonance, the quantum back-action and the photon shot noise imprecision should be equal at the standard quantum limit in an ideal measurement.

Our measurements are not ideal, in the sense that not all scattered light is collected, we detect for non-zero detuning, and noise sources other than quantum noise contribute. Therefore, an imprecision comparable to $\bar{S}_{xx}^{ZPF}$ is obtained only at higher power. For comparison, it is still interesting to see for which power such (imprecision) noise levels can be reached. We call this power $P_{imp@SQL}$.

In Figures 2.17–2.19 we plot all noise contributions to the imprecision, including shot noise (purple line), which can be compared to the shot noise imprecision for an ideal measurement (purple dashed line).

### 2.6.2 High-$Q_m$ oscillator

In Figure 2.17, we show the spectral density of the low-frequency beam, with mechanical parameters shown in the top row of Table 2.4. Panel (a) shows the spectral displacement density $\bar{S}_{xx}^{th}(\Omega)$ and the added imprecision $\bar{S}_{xx}^{imp}$ for an input power $P_{in}$ = 10 μW. The displacement can be integrated to find a variance $\langle x^2 \rangle = 5.4 \times 10^{-20}$ m$^2$, using Equation (2.31). The imprecision was calculated using the parameters from Table 2.3, multiplying the RIN by 10 to account for the increased laser classical noise at 1 MHz (see Figure 2.12). Panel (b) shows the square root of the spectral displacement density $\sqrt{\bar{S}_{xx}^{th}(\Omega)}$.

In panel (c), we plot various imprecision and displacement spectral densities as a function of input power $P_{in}$. The red line is the total signal $\bar{S}_{xx}^{th}(\Omega_m) + \bar{S}_{xx}^{imp}$, consisting of the constant thermal displacement density (blue) and the total noise imprecision (black), which is specified in Equation (2.105). We can determine that the power for which $\bar{S}_{xx}^{th}(\Omega_m) = \bar{S}_{xx}^{imp}$, at which we can resolve the mechanical displacement with a signal-to-noise ratio of 1, is the low value of $P_{in}$ = 69 nW: this is the point where the black line crosses the blue. This panel also clearly shows the power-scaling of the different imprecisions: at low power the imprecision due to electrical noise (blue), scaling with $P_{in}^{-2}$ dominates, and at high power the classical noise imprecision, which is non-power dependent, dominates (gold). The shot noise ($\propto P_{in}^{-1}$) is shown in purple, and the shot noise limit, which would be attained for an ideal measurement on resonance (which would require interferometry to convert the resulting phase fluctuation spectral density) is shown as the dashed purple line. The quantum back-action, which scales $\propto P_{in}$, is plotted as the green dashed line.

The zero-point fluctuations are shown as the dashed black line in Figure 2.17. For this mechanical resonator, we find $P_{imp@SQL} \approx 8$ μW using plasmonic trans-

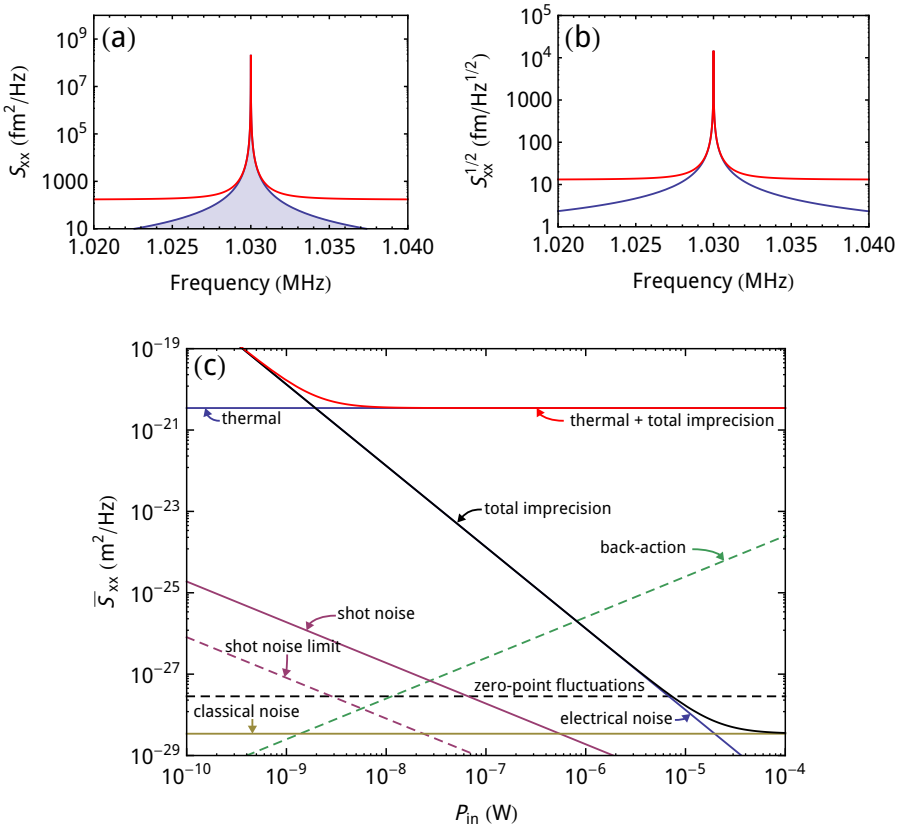


**Figure 2.17:** Calculated transduction for the plasmonic system in combination with a high-Q mechanical oscillator. (a): Spectral displacement density: $\bar{S}_{xx}^{th}(\Omega)$ (blue) and $\bar{S}_{xx}^{th}(\Omega) + S_{xx}^{imp}$ (red), for $P_{in} = 10$ μW. (b): Square root of the spectral displacement density. (c): Imprecision and displacement spectral densities as a function of input power. The solid blue line is the thermal spectral density $\bar{S}_{xx}^{th}(\Omega_m)$, the dashed black line shows the symmetrized zero point fluctuations $\bar{S}_{xx}^{ZPF}(\Omega_m)$. The imprecision contributions are electrical (blue), shot noise (red) and classical noise (gold), with the black line the total imprecision. The red line shows $\bar{S}_{xx}^{th}(\Omega_m) + \bar{S}_{xx}^{imp}$. The green dashed line is the measurement back-action $\bar{S}_{xx}^{qba}$, and the purple dashed line is the shot noise limit: the minimum possible shot noise-induced imprecision, for measurement on the optical resonance. Mechanical parameters are shown in Table 2.4, electrical parameters in Table 2.3.

duction. This is the power for which the total imprecision $\bar{S}_{xx}^{imp,tot}$ is equal to the zero-point fluctuations. This low $P_{imp@SQL}$ shows the high sensitivity that is in principle attainable with plasmonic transducers. If we calculate the shot-noise limited imprecision (setting $\bar{S}_{xx}^{class} = 0$ and $\bar{S}_{xx}^{el} = 0$), we find $P_{imp@SQL} = 66$ nW.

### 2.6.3 High-$\Omega_m$ oscillator

Next, we perform the same analysis using mechanical properties of a high-frequency oscillator such as that of Yang et al. [97], (see properties in second row of Table 2.4), with spectral densities and imprecisions shown in Figure 2.18.

First, we note that, both due to the higher frequency and the much lower temperature compared to the low-frequency beam, the thermal occupation of the mode is much smaller than for the low-frequency oscillator; integrating the spectral displacement density leads to a variance of $\langle x^2 \rangle = 5 \times 10^{-25}$ m$^2$. This reduces the sensitivity: the thermal displacement is much lower compared to the imprecision. We find that to achieve $\bar{S}_{xx}^{imp} = \bar{S}_{xx}^{th}(\Omega_m)$ (i.e. a signal-to-noise ratio of 1), we need an input power $P_{in} = 64$ μW. This situation is plotted in panels a and b, for $\bar{S}_{xx}$ and $\sqrt{\bar{S}_{xx}}$ respectively. In panel c, we again plot the power-dependence of the imprecision. For this oscillator, we see that the classical noise imprecision $\bar{S}_{xx}^{imp,class} \gg \bar{S}_{xx}^{ZPF}(\Omega_m)$. We can however calculate that the shot-noise limited imprecision is equal to the SQL ($\bar{S}_{xx}^{imp} = \bar{S}_{xx}^{ZPF}$) for an input power $P_{imp@SQL} = 5$ mW.

### 2.6.4 10 MHz oscillator

Finally, we also plot the sensitivity curves for the 10 MHz beam, whose spectral density is shown in Figure 2.5. This beam is representative of the beams we will study in Chapter 6. The sensitivity curves are plotted in Figure 2.19, for both a high-$\mathscr{A}$ and a low-$\mathscr{A}$ scatterer. Because the NA in Figure 2.19b is smaller (NA = 1 in panel (a) vs NA = 0.4 in panel (b)), the difference between the shot noise imprecision and the shot noise limit is much larger in panel (b) than it is in panel (a): fewer photons are detected due to the smaller numerical aperture.

To obtain an imprecision equal to the thermally driven displacement, $\bar{S}_{xx}^{imp} = \bar{S}_{xx}^{th}(\Omega_m)$, we require 250 nW of power for the high-$\mathscr{A}$ scatterer and 22 μW for the low-$\mathscr{A}$ scatterer. For the current parameters, we can not attain an imprecision equal to that at the SQL: the laser classical noise imprecision is larger than the zero-point fluctuations. If we were to perform a shot-noise limited measurement, $P_{imp@SQL}$ would be approximately 120 μW for the good scatterer, and approximately 900 mW for the bad scatterer.

In this section, we have investigated the different noise imprecisions as a function of measurement power, using three different mechanical systems. In all three cases, the laser classical noise is the limiting factor in achieving measurement imprecisions at the standard quantum level. For the 10 MHz beam, the classical laser noise imprecision is larger than the spectral density of the zero-point fluctuations.

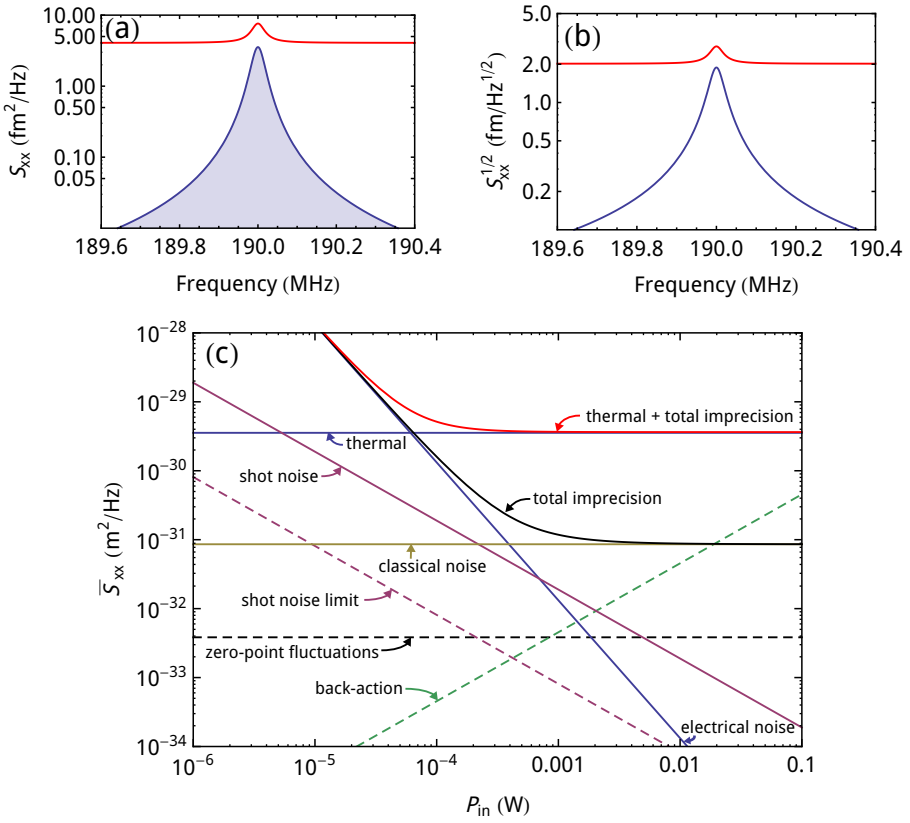


**Figure 2.18:** Calculated transduction for the plasmonic system in combination with a high-frequency mechanical oscillator. (a): Spectral displacement density: $\bar{S}_{xx}^{th}(\Omega)$ (blue) and $\bar{S}_{xx}^{th}(\Omega) + S_{xx}^{imp}$ (red), for $P_{in} = 65$ µW, attaining a signal-to-noise ratio of 1. (b): Square root of the spectral displacement density. (c): Imprecision and displacement spectral densities as a function of input power. The solid blue line is the thermal spectral density $\bar{S}_{xx}^{th}(\Omega_m)$, the dashed black line shows the symmetrized zero point fluctuations $\bar{S}_{xx}^{ZPF}(\Omega_m)$. The imprecision contributions are electrical (blue), shot noise (red) and classical noise (gold), with the black line the total imprecision. The red line shows $\bar{S}_{xx}^{th}(\Omega_m) + \bar{S}_{xx}^{imp}$. The green dashed line is the measurement back-action $\bar{S}_{xx}^{qba}$, and the purple dashed line is the shot noise limit: the minimum possible shot noise-induced imprecision, for measurement on the optical resonance. Mechanical parameters are shown in Table 2.4, electrical parameters in Table 2.3.

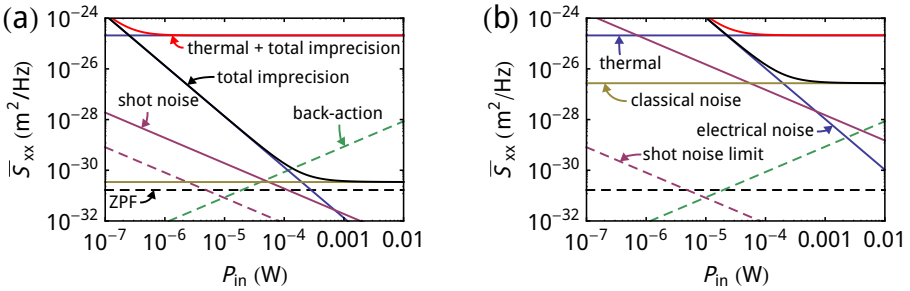


**Figure 2.19:** Calculated transduction for the plasmonic system in combination with a 10 MHz mechanical oscillator with $Q_m = 1000$. (a): Transduction by $\mathscr{A} = 1$, NA = 1 scatterer. (b): Transduction by $\mathscr{A} = 0.1$, NA = 0.4 scatterer. The solid blue line is the thermal spectral density $\bar{S}_{xx}^{th}(\Omega_m)$, the dashed black line shows the symmetrized zero point fluctuations $\bar{S}_{xx}^{ZPF}(\Omega_m)$. The imprecision contributions are electrical (blue), shot noise (red) and classical noise (gold), with the black line the total imprecision. The red line shows $\bar{S}_{xx}^{th}(\Omega_m) + S_{xx}^{imp}$. The green dashed line is the measurement back-action $\bar{S}_{xx}^{qba}$, and the purple dashed line is the shot noise limit: the minimum possible shot noise-induced imprecision, for measurement on the optical resonance. Mechanical parameters are shown in Table 2.4, electrical parameters in Table 2.3.

Because the classical laser noise has the same scaling with input power as the transduction of mechanical fluctuations, increasing the measurement power does not reduce the relative contribution of the classical laser noise to the imprecision. We do note that the classical laser noise is a technical limitation, and there are several methods to reduce this noise, several of which are described in Section 2.5.4.

For the good scatterer, very low powers to measure at the SQL are obtained, especially for the high-$Q_m$ beam. We do note that the good scatterer is the ultimate limit, using two NA = 1 objectives and a non-absorbing scatterer. Therefore, we have also plotted the sensitivity for the low-$\mathscr{A}$ scatterer for the 10 MHz beam, showing a more experimentally feasible scenario.

## 2.7 Plasmonic metal-insulator-metal transduction

In Chapters 4 and 5, we measure plasmonic transduction using gold-coated beams (Figure 1.3a), where the sidewalls of the gold layer support a plasmonic metal-insulator-metal (MIM) resonance. The geometry is effectively reversed from that of a dipolar scatterer: the gold covering layer creates a dark-field geometry, where the only light that is transmitted is light that has been scattered through the plasmonic aperture. In cavity optomechanics, this is equivalent to a two-sided Fabry-Pérot cavity, where transmission is monitored.


**Figure 2.20:** Geometry for plasmonic metal-insulator-metal (left) and geometric toy model (right) transduction.

In this section, we will show how the plasmonic MIM geometry is similar to using crossed polarizers, and compare it to a simple geometric shadowing toy model [98]. Figure 2.20 sketches the plasmonic metal-insulator-metal and toy model configurations.

## 2.7.1 Plasmonic darkfield transduction

For the transduction by the plasmonic metal-insulator-metal resonance, we use the focused scattering model derived in Section 2.3, starting from Equation (2.81). Because the metal covering on the beams rejects all the direct transmission (reflecting it instead); we set two of the three terms to 0: the direct transmission term and the $\mathrm{Im}(\alpha)$ term, which represents the extinction, leaving only the scattered field:

$$P_{\mathrm{out}} = P_{\mathrm{in}} \left[ |\alpha|^2 \mathscr{A}_0^2 \left( 3 + \frac{2}{3}\cos\beta_{\mathrm{out}} + \frac{1}{3}\cos 2\beta_{\mathrm{out}} \right) \frac{\sin^2\left(\beta_{\mathrm{out}}/2\right)}{\sin^2\beta_{\mathrm{in}}} \cos^2\zeta_{\mathrm{in}} \right]. \quad (2.112)$$

For the comparison of the MIM geometry with the geometric toy model, we assume a dipole scattering at the unitary limit, with $\gamma_{\mathrm{i}} = 0$ and $Q = \gamma/\omega_0 = 12$. We use $G = 2\pi \times 1$ THz/nm, which is a reasonable value for a width of the gap between the MIM sidewalls of 30 nm, a typical value used in the experiments in Chapters 4 and 5. The transmittance $\mathscr{T}$ and the change in transmittance $\frac{\partial \mathscr{T}}{\partial x}$ are plotted for these parameters in Figure 2.21, as a function of focusing angle $\beta$ and frequency $\omega$. Both $\mathscr{T}$ and $\frac{\partial \mathscr{T}}{\partial x}$ are strongly dependent on these parameters, with both improving for increasing numerical aperture. At the optimum detuning and NA = 1, a transduction of $\frac{\partial \mathscr{T}/\partial x}{\mathscr{T}} = \frac{0.05}{\mathrm{nm}}$ is calculated.

## 2.7.2 Geometric model transduction

We compare the resonant MIM transmission to a geometric toy model, as sketched in Figure 2.20. We assume that in the focal plane, the beam has a circular effective area $\mathscr{A}_{\mathrm{eff}}$, with a power density $\mathscr{P} = P_{\mathrm{in}}/\mathscr{A}_{\mathrm{eff}}$, and integrate this power density over the opening area given by the opening width $x$. For the area of the focused laser beam in the focal plane, we will extract the effective area $\mathscr{A}_{\mathrm{eff}}$ [78, 89] from the

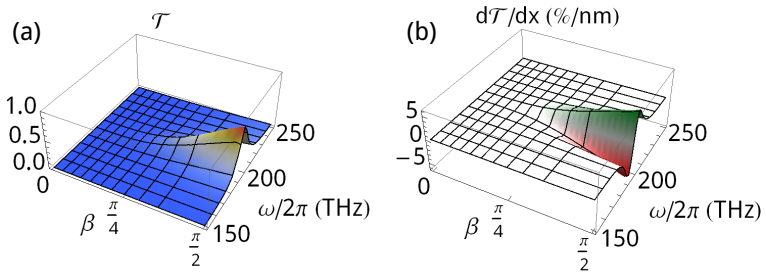


**Figure 2.21:** Transmittivity for the MIM darkfield geometry as a function of focusing angle $\beta$ and laser frequency $\omega$. Left panel: transmittance $\mathcal{T}$ (as shown in Equation (2.112), right panel: derivative of transmittance $\frac{\partial \mathcal{T}}{\partial x}$. The mesh lines normal to the $\beta$ axis indicate NA = $(0.1, 0.2, \ldots, 0.9)$.

focusing analysis in Section 2.3.5 as

$$\begin{aligned} \mathscr{A}_{\text{eff}} &= \frac{P_{\text{in}}}{2cW_{\text{inc}}^{\text{el}}(O)} \\ &= \frac{\lambda^2 \sin^2 \beta_{\text{in}}}{\pi \mathscr{I}_0(O)^2} \end{aligned} \tag{2.113}$$

using

$$P_{\text{in}} = \frac{1}{2}\epsilon_0 c E_0^2 \pi a^2, \tag{2.114}$$

$$W_{\text{inc}}^{\text{el}}(O) = \left(\frac{\pi F E_0 \left|\mathscr{I}_0(O)\right|}{2\lambda}\right)^2, \text{ and} \tag{2.115}$$

$$\mathscr{I}_0(O) = 2\left(\frac{8}{15} - \frac{1}{3}\cos^{3/2}\beta_{\text{in}} - \frac{1}{5}\cos 5/2\beta_{\text{in}}\right), \tag{2.116}$$

where $P_{\text{in}}$ is the incident power, $W_{\text{inc}}^{\text{el}}(O)$ is the electromagnetic energy density at the origin and $\mathscr{I}_0(O)$ is a diffraction integral, evaluated at the origin.

We will take the power density $\mathscr{P}$ in the focal plane to be constant, as $\mathscr{P} = P_{\text{in}}/\mathscr{A}_{\text{eff}}$ for radial distances $r$ within the effective focal area, $r \leq \sqrt{\mathscr{A}_{\text{eff}}/\pi}$. To find the transmitted power we integrate this power density over the opening width $x$, finding the transmittance:

$$\mathscr{T}_{\text{geom}} = \frac{P_{\text{out}}}{P_{\text{in}}} = \int_{\infty}^{\infty}\int_{-x/2}^{x/2} \mathscr{P}\,\mathrm{d}x'\mathrm{d}y \tag{2.117}$$

$$\approx \frac{2x}{\sqrt{\mathscr{A}_{\text{eff}}\pi}} + O(x^2), \tag{2.118}$$

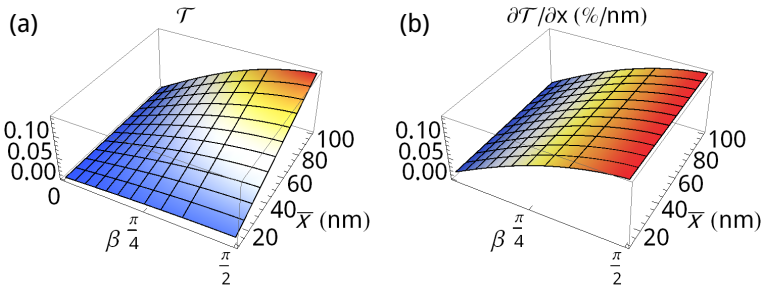


**Figure 2.22:** Left panel: transmittance $\mathcal{T}$ (Equation (2.118)), right panel, change in transittance $\frac{\partial\mathcal{T}}{\partial x}$ (Equation (2.119))for the geometric model, as a function of slot width $\bar{x}$ and focusing angle $\beta$. The mesh lines normal to the $\beta$ axis indicate NA = $(0.1, 0.2, \ldots, 0.9)$.

assuming $x \ll r$. In this limit, we can find the change in transmittance due to a change in gap width:

$$\frac{\partial\mathcal{T}_{\text{geom}}}{\partial x} = 2\sqrt{\frac{\mathcal{A}_{\text{eff}}}{\pi}}. \tag{2.119}$$

In Figure 2.22, we plot $\mathcal{T}_{\text{geom}}$ and $\frac{\partial\mathcal{T}_{\text{geom}}}{\partial x}$, as a function of $x$ and $\beta_{\text{in}}$. The geometric toy model transduction is a non-resonant effect. It is however weakly dependent on the laser frequency in that the size of the focal spot depends on the frequency, with higher frequencies leading to more tightly focused spots and therefore more transmittance. We note that for very small gaps, the output power modulation can be high:

$$\delta P_{\text{out}} = P_{\text{in}}\mathcal{T}_{\text{geom}}\frac{\partial\mathcal{T}_{\text{geom}}}{\partial x}\delta x. \tag{2.120}$$

The change in transmittance does not depend on the unmodulated gap width $\bar{x}$. However, the DC transmittance $P_{\text{in}}\mathcal{T}_{\text{geom}}$ can be very small (as shown in Figure 2.22), leading to high modulation. We note that this model is a fairly simple approximation. The full analysis requires calculating the transmittance through a slit in a perfectly conducting screen, as discussed by Born & Wolf in §11.8.3 of *Principles of Optics* [99].

We can now compare the imprecision attainable for the MIM transduction and the geometric toy model transduction. We repeat Equation (2.105):

$$S_{\text{xx}}^{\text{imp}} = \frac{2\,\text{NEP}^2}{P_{\text{in}}^2}\frac{1}{(\partial\mathcal{T}/\partial x)^2} + \frac{\hbar\omega}{P_{\text{in}}}\frac{\mathcal{T}}{(\partial\mathcal{T}/\partial x)^2} + \text{RIN}^2\frac{\mathcal{T}^2}{(\partial\mathcal{T}/\partial x)^2}, \tag{2.121}$$

filling in $\mathcal{T}_{\text{MIM}}$ and $\frac{\partial\mathcal{T}_{\text{MIM}}}{\partial x}$ and $\mathcal{T}_{\text{geom}}$ and $\frac{\partial\mathcal{T}_{\text{geom}}}{\partial x}$, plotting the result in Figure 2.23.

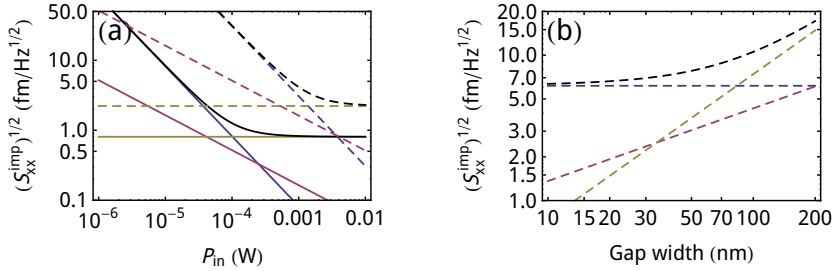


**Figure 2.23:** Comparison of the imprecision level for MIM transduction and geometric transduction. (a): comparison as a function of input power $P_{\text{in}}$ for a gap width of 30 nm. Solid lines: imprecisions for MIM geometry; dashed lines: imprecisions for geometric model. Black: total; blue: electrical; purple: shot noise; gold: classical laser imprecision. (b): Geometric model imprecision as a function of gap width $\bar{x}$, at power $P_{\text{in}} = 500$ μW, showing low imprecision for very narrow gaps.

For the MIM transduction, we use the good-scattering parameters, as discussed in Section 2.5: $Q_{\text{opt}} = 10$, $G = 2\pi \times 1$ THz/nm, $\omega_0 = 2\pi \times 210$ THz, $\omega = 2\pi \times 200$ THz, to achieve optimum detuning of $\Delta = \omega - \omega_0 = \frac{1}{2\sqrt{3}}\gamma$. The gap width for the geometric model was set to $\bar{x} = 30$ nm, with $\omega = 2\pi \times 200$ THz. The solid lines show the imprecision contributions for the MIM geometry, the dashed lines those for the geometric model. Clearly, the plasmonic geometry has a lower imprecision for all input powers.

We can compare the sensitivity obtained at $P_{\text{in}} = 500$ μW to that for the scattering plasmonic dimer as shown in Figure 2.14, and see a very similar imprecision level for plasmonic dimer and MIM geometry: $\sqrt{S_{\text{xx,MIM}}^{\text{imp}}} = 8 \times 10^{-16}$ m/$\sqrt{\text{Hz}}$, $\sqrt{S_{\text{xx,dimer}}^{\text{imp}}} = 5 \times 10^{-16}$ m/$\sqrt{\text{Hz}}$ at $\zeta = 0$. The geometric transduction for a 30 nm-wide gap is $\sqrt{S_{\text{xx,geom}}^{\text{imp}}} = 1 \times 10^{-14}$ m/$\sqrt{\text{Hz}}$.

In Figure 2.23b, we show the geometric toy model imprecision levels as a function of gap width. Increasing the gap width increases the power transmitted through the slot, while keeping the change in transmittance $\frac{\partial \mathcal{T}}{\partial x}$ constant. Therefore, we see that increasing the gap width increases the shot noise and classical noise imprecision contributions. For narrow gaps, the transmittance goes down. This leaves the geometric transduction limited by the electrical noise contribution to the imprecision, estimated here for the detector used in our experiments.

## 2.8 Radiation pressure force & the optical spring effect

Up to now, we have only discussed how light can be used to detect mechanical motion. However, because photons carry momentum, they can exert a force. By exerting forces, the light field can influence the mechanical properties of the system. In this section, we will discuss the radiation pressure force. As we will see in Section 5.4, there is also another way a photon can exert a force: through absorption, light can cause heating, which can then drive the mechanical system.

In cavity optomechanics, the radiation pressure force is characterized by the coupling factor $G$ and the number of photons circulating in the cavity $\bar{n}_{\mathrm{cav}}$:

$$F(x) = \hbar G \bar{n}_{\mathrm{cav}}. \tag{2.122}$$

This equation shows both the strength and the weakness of the plasmonic system under study here. Because $G$ is large, around $2\pi \times 1$ THz/nm, the force per photon is high. However, due to the low optical quality factor of plasmonic systems, the number of circulating photons $\bar{n}_{\mathrm{phot}}$ is relatively low. We assume dynamic phenomena due to retarded radiation pressures, such as cooling and heating, are limited, as the photon lifetime is much smaller than the mechanical oscillation period: $1/\gamma \ll 1/\Omega_{\mathrm{m}}$. This implies that an individual photon does not 'see' the cavity oscillating, but instead sees a 'snapshot' of the optical cavity configuration. Therefore, we will not study these effects.

We restrict ourselves to determining static phenomena, and focus on the optical spring effect: the radiation pressure mediated stiffening or softening of the mechanical oscillator. We use the properties of scattering dipoles calculated in this chapter to determine the optical force between the two dipoles of the dimer antenna, and determine the magnitude of the optical spring effect.

The radiation pressure force can be derived from a potential, following the derivation by Aspelmeyer *et al.* [100]:

$$F(x) = -\frac{\partial V_{\mathrm{rad}}(x)}{\partial x}. \tag{2.123}$$

The total potential for the mechanical oscillator is then:

$$V(x) = \frac{m_{\mathrm{eff}}\Omega_{\mathrm{m}}}{2} x^2 + V_{\mathrm{rad}}(x). \tag{2.124}$$

This modified potential creates a new equilibrium position, $x_0 \neq 0$, and changes the effective spring constant to a new value:

$$k_{\mathrm{eff}} = V''(x_0) = m_{\mathrm{eff}}\Omega_{\mathrm{m}}^2 + V''_{\mathrm{rad}}(x_0), \tag{2.125}$$

where the prime ($'$) indicates differentiation with respect to $x$. This leads to an expression for the change in mechanical frequency :

$$\delta\Omega_{\mathrm{m}} = 8\Delta \frac{G}{\gamma} \sqrt{\frac{\hbar}{2m_{\mathrm{eff}}\Omega_{\mathrm{m}}}} \frac{\bar{n}_{\mathrm{cav}}^{\mathrm{max}}}{\left[1 + (2\Delta/\gamma)^2\right]^2}. \tag{2.126}$$

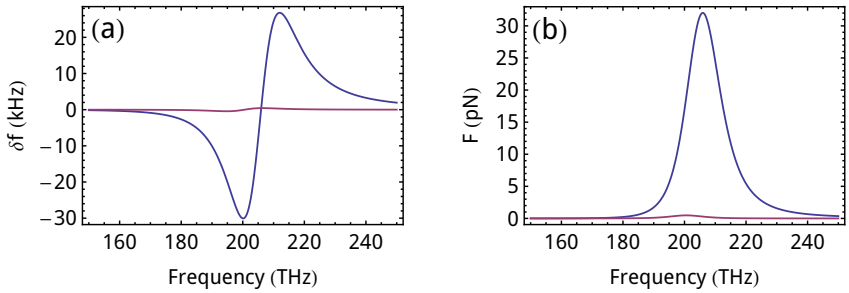


**Figure 2.24:** (a): Frequency shift and (b) optical force as a function of frequency for the good and bad scatterer. The scatterer is excited with 500 μW of optical power through an NA = 1 objective for the $\mathscr{A}$ = 1 scatterer, and through an NA = 0.4 objective for the $\mathscr{A}$ = 0.1 scatterer, with coupling rate $G = 2\pi \times 1$ THz/nm. The beam has a resonant frequency of 9 MHz, with $Q$ = 1000.

We now need to determine the number of photons circulating in our plasmonic cavity. Using the expressions derived for the transmittance, we set the photon number to be:

$$\bar{n}_{\text{phot}} = \frac{k}{\epsilon_0} \frac{\text{Im}(\alpha)}{\mathscr{A}_0} \frac{4P_{\text{in}}}{\gamma \hbar \omega}, \tag{2.127}$$

which is equal to the extinction term in Equation (2.81), where we have defined $\bar{n}_{\text{cav}}^{\text{max}} \equiv \bar{n}_{\text{phot}}(\Delta = 0)$. The resulting frequency shift and optical force, $F_{\text{opt}} = \hbar G \bar{n}_{\text{phot}}$ are shown in Figure 2.24a and b respectively, as a function of optical detuning. For the dimer antennas studied in Chapter 6, we have $f_{\text{m}} \approx 9$ MHz and $Q \approx 1000$. The results in Chapter 6 show an albedo worse than that of the low-$\mathscr{A}$ scatterer studied in this chapter. This implies that we will not observe an optical spring effect in Chapter 6. However, the calculations shown in Figure 2.24 show that, if we improve the experimentally observed albedo, an optical spring effect should be observable, as the frequency shift $\delta f$ calculated in Figure 2.24 is more than 2 times larger than the mechanical loss rate $\Omega_{\text{m}}/Q \approx 9000$ rad/s measured in Chapter 6.

## 2.9 Conclusion

In this chapter, we have shown the theoretical properties of the systems we will study in the remaining chapters, investigating both the mechanical and optical properties.

First, we derived the mechanical properties of doubly clamped beams. The model for a uniform doubly clamped beam was expanded to include bilayer beams and the effect of axial stress. Next, we used the fluctuation-dissipation theorem to

| $\sqrt{S_{xx}^{imp}}$ (m/$\sqrt{\text{Hz}}$) | high-$\mathscr{A}$ | low-$\mathscr{A}$ |
|---|---|---|
| constant $P_{in}$ | $5 \times 10^{-16}$ | $4 \times 10^{-14} (\zeta \approx \pi/5)$ |
| constant $P_{out}$ | $6 \times 10^{-16}$ | $1 \times 10^{-15} (\zeta \approx \pi/4)$ |
| MIM | $8 \times 10^{-16}$ | |
| geometric | $1 \times 10^{-14}$ | |

| oscillator | $\sqrt{S_{xx}^{th}}$ (m/$\sqrt{\text{Hz}}$) | $P_{imp@SQL}$ |
|---|---|---|
| high-$Q$ | $5.9 \times 10^{-11}$ | 66 nW |
| high-$\Omega_m$ | $1.9 \times 10^{-15}$ | 5 mW |
| 10 MHz | $1.7 \times 10^{-14}$ | 113 µW |

**Table 2.5:** Calculated imprecision and thermal displacement spectral densities for the various transduction models and beams described in this chapter. The terms "high-$\mathscr{A}$" and "low-$\mathscr{A}$" refer to the different scatterer parameters as defined in Section 2.5. Mechanical parameters for the different beams are given in Table 2.4. The 10 MHz beam is typical for the beams we will study in Chapter 6. Its spectral density is plotted in Figure 2.5. $P_{SQL}$ refers to the power needed to perform a measurement with a shot-noise limited imprecision $\bar{S}_{xx}^{imp,SN} = \bar{S}_{xx}^{ZPF}$, as discussed in Section 2.6.

calculate the displacement spectral density caused by the thermal occupation of beams.

To investigate the optical properties of plasmonic antennas, we started by analyzing the scattering properties of two coupled particles, calculating the interparticle-spacing-dependent scattering properties of such a system. Next, we calculated the excitation of such a system by a focused light field. We included polarization, which allowed the investigation of the use of crossed polarizers to improve signal-to-noise ratios. In Chapters 4 and 5, a different plasmonic transducer is used, using not a scattering particle but an MIM slot. A model for this system was created, and we compared this to a geometric transduction model.

The noise in the measurements is due to the fact that the laser beam and detector used to measure are not noise free. We showed typical noise parameters for the laser and detector we used in most of the experiments performed in this thesis, and calculated how the noise spectral densities propagate through the system, allowing a comparison of signal and noise. This is conveniently expressed as displacement imprecision spectral densities $S_{xx}^{imp}(\Omega)$, which can be compared to a (nano)beam's thermal spectral displacement density $S_{xx}^{th}(\Omega)$. We calculated imprecisions both for constant input power $P_{in}$ and constant output power $P_{out}$, for both an ideal and a more realistic scatterer. We then compared these imprecisions to thermal displacements for several different mechanical systems, and introduced the standard quantum level as a measure for sensitivity. Table 2.5 gives an overview

of these calculated values, showing the low imprecisions obtainable with optimized plasmonic systems.

# 3

# Methods

Measuring the nanomechanical motion of plasmonic nanostructures requires several components, which we will describe in this chapter. First, in Section 3.1, we describe the vacuum microscope used for measurements, including the vacuum chamber, scanning stages, optics, electronics, and software control. Section 3.2 describes the fabrication process for creating gold-coated silicon-nitride nanobeams using sputter coating and focused ion beam (FIB) milling. In Section 3.3, we describe the fabrication processes used to create individual plasmonic antennas on nanobeams. We used two fabrication protocols: the first uses sputter coating of gold and FIB milling. The second uses electron-beam lithography (EBL) to pattern antennas, followed by a FIB step to define the nanobeams around the antennas.

## 3.1 Measurement setup

In this section, we will discuss the optical setup used to accurately focus and scan laser spots on samples containing plasmonic transducers and to measure the optomechanical response. A schematic of the setup is shown in Figure 3.1. First, we discuss the design of the vacuum chamber. As the motion of the mechanical oscillators is damped by ambient air pressures (a measurement is shown in Chapter 4, Figure 4.7), the samples must be placed in a vacuum environment.

Figure 3.2 shows the nano-optomechanical vacuum system that was designed and constructed at AMOLF. Photographs of the completed system are shown in Figure 3.3. A square aluminum chamber was mechanically milled from a solid aluminum block. A PMMA lid was placed on top, with a rubber O-ring for sealing. A turbomolecular pump was used to pump to a typical vacuum pressure of

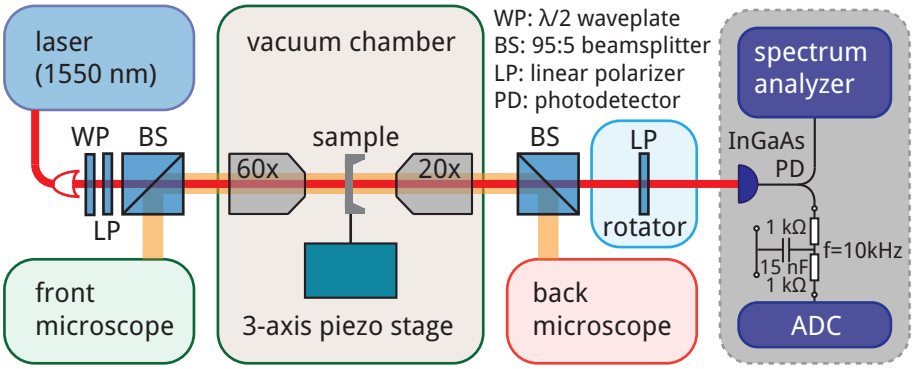


**Figure 3.1:** Schematic of the nano-optomechanical measurement setup.

$\sim 10^{-3}$ mbar, limited by the outgassing of the PMMA lid. The vacuum chamber floor was made 20 mm thick for mechanical rigidity. A thinner floor (10 mm), used in an initial design, was measured to bend by 20 µm in the center when under vacuum, leading to a defocusing of the microscope objectives.

The sample and the incoupling objective are placed on five-axis stip-slick motor-driven stages (New Focus 8081-M) to allow 3 mm of motion control. The outcoupling objective is placed in a micrometer-driven translation mount (Thorlabs ST1-XY/M) to allow alignment of this objective onto the optical axis. The sample stage includes a three-axis capacitive-feedback piezo stage (PiezoJena Tritor 40) to allow for high-resolution raster scanning of the sample. The objectives are placed inside the vacuum chamber to allow the use of high-NA short working distance objectives.

In most experiments we use an erbium-doped-fiber laser (NKT Photonics Koheras) operating at 1550 nm (linewidth < 100 kHz), in combination with a DC-coupled InGaAs photodiode for detection (Femto HCA-S-200M-IN-FC). A 633 nm HeNe laser (Melles Griot) and a 780 nm external cavity diode laser (New Focus SWL-7500) were also used, in combination with an AC-coupled silicon photodiode (New Focus 1801-FC). Waveplates, polarizers and polarizing beamsplitters are used to control the polarization states of the input and output beams. The output polarizer is placed in a motorized rotation stage (Newport NSR-1). Pellicle beamsplitters are used to divert light to front and back microscopes equipped with CMOS cameras and white-light LED illumination sources, to image input and output spots on the sample.

The photodiode signal is analyzed on an electronic spectrum analyzer (Rohde & Schwarz FSV-3), and passed through a low–pass filter to an oscilloscope (Tektronix TEK-200) and DAQ card (National Instruments USB-6229), with the low-pass filter blocking high-frequency noise from the DAQ card. This card is also used as a digital-to-analog converter to control the piezo stage, and TTL lines are used to control the illumination LEDs. The entire experiment is controlled

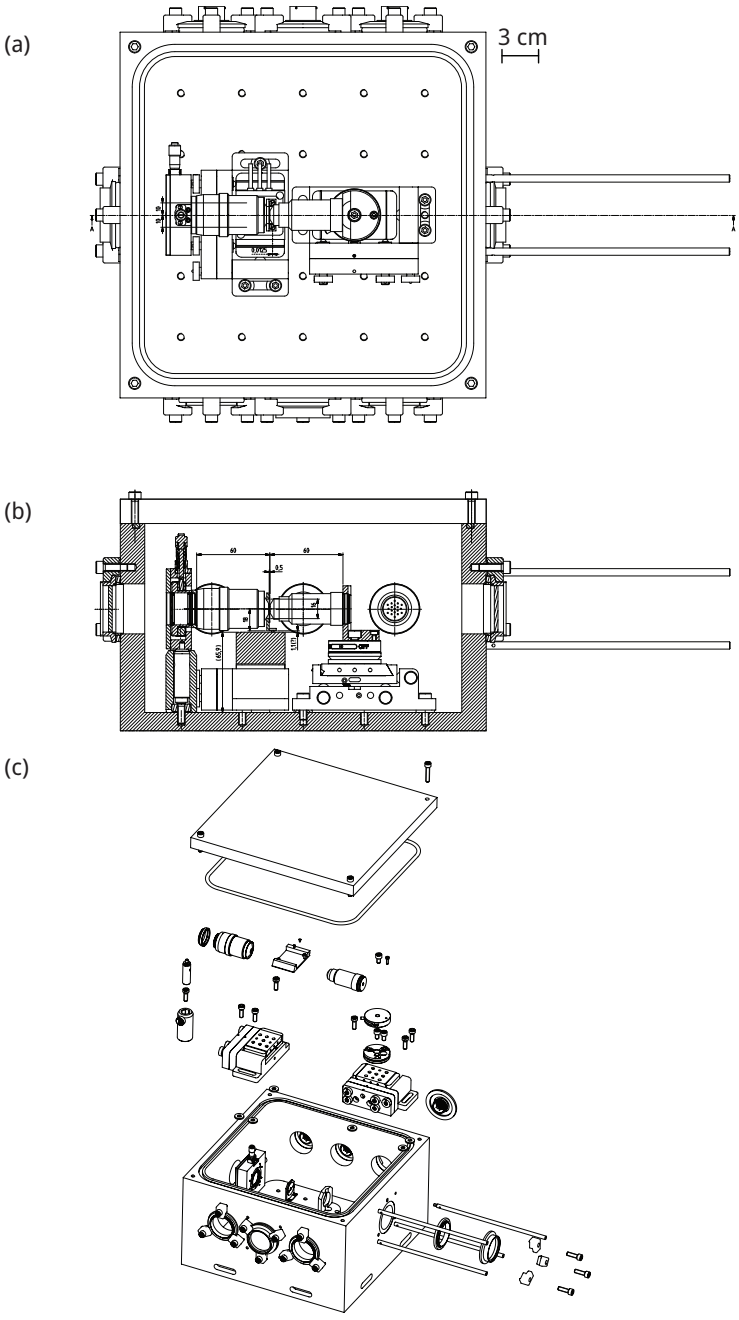


**Figure 3.2:** Design drawing of vacuum chamber (design: Iliya Cerjak, AMOLF). (a): top view, (b): side view, (c): exploded view.

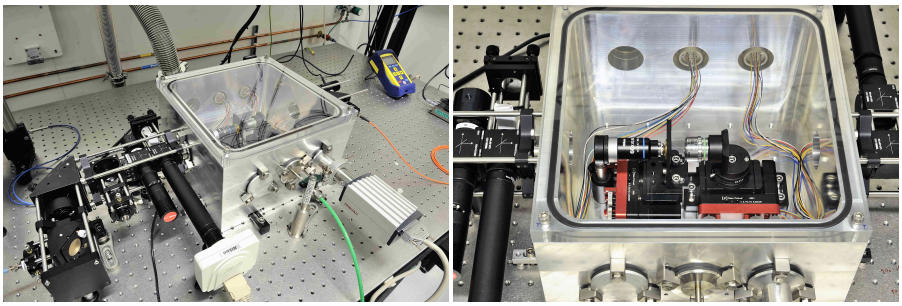

(a) (b)

**Figure 3.3:** (a): Nano-optomechanical measurement setup photographed from the side, showing incoupling microscope and (b) from the top, showing the inside of the vacuum chamber. Photography: Henk-Jan Boluijt.

by a specially designed LabView program, controlling the motion of the 5-axis translation stages and piezo stage, polarization rotator, microscope illumination lamps, electronic spectrum analyzer and analog-to-digital-converter.

## 3.2 Fabrication of linear arrays of micromechanical oscillators

Gold-coated nanomechanical oscillators, measurements on which are described in Chapters 4 and 5, were made using high-stress ($\sigma = 800$ MPa) stoichiometric silicon nitride membranes, with $0.5 \times 0.5$ mm square windows on 200-µm-thick $5 \times 5$-mm-square frames (Norcada, Canada), shown in Figure 3.4a. We use sputter coating, at a base pressure of $10^{-3}$ mbar of Ar gas, to deposit 100 nm of gold on the back side of the membrane, and 3 nm of gold on the top side, using an Emitech 575DX sputter coater.

Focused ion beam milling was used to create linear slots in the metal-coated membranes to form the mechanical oscillators. A 30 keV gallium ion beam was used in a FEI Helios-600 dual beam system. Using a beam current of 9.7 pA, two types of samples were made: with two parallel mechanical beams in which light is coupled to the slit between the two beams, and arrays composed of 8 parallel mechanical beams. In these array structures, we can either probe the beams separately, using a tightly focused laser beam, or collectively, using a laser spot defocused to cover the entire array.

We mill from the top side, as sketched in Figure 3.4b. The 3-nm-thin gold top layer keeps the silicon nitride from charging, greatly reducing sample drift during milling. By milling from the top side, the tapering inherent in focused ion beam milling is used in our favor: the taper in the silicon nitride beams acts as an etch mask for the softer gold behind it, leading to narrower slits in the gold layer, allow-

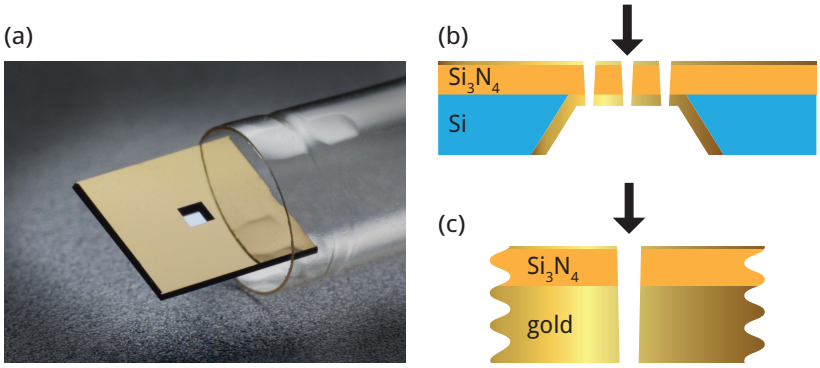


**Figure 3.4:** (a): Photo of a 50-nm-thick 0.5-mm-square silicon nitride membrane in a 5-mm-square silicon frame (photo credit: Anneke Thijssen). (b): Schematic cross section of membrane geometry, with the arrow indicating the direction of ion beam incidence. (c): Zoom of one of the milled slits. Layer thicknesses and slit width are to scale.

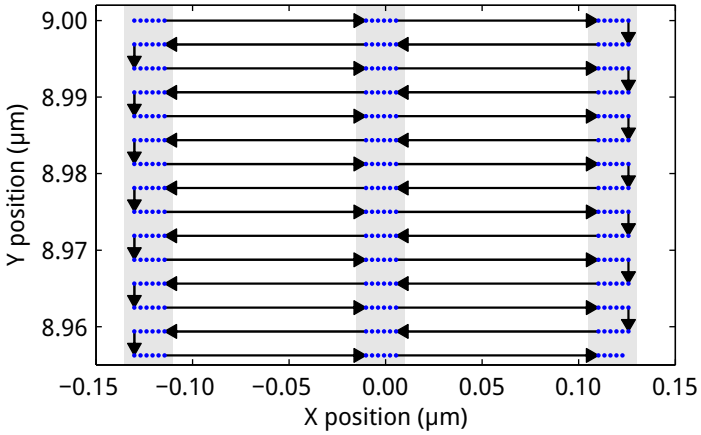


**Figure 3.5:** First 16 rows of serpentine pattern used for milling single-pass structures with FIB. Blue dots indicate milling positions, the arrows indicate the milling order. The gray vertical sections are the milled slots.

ing more control over the plasmonic modes in the gap between the gold-coated beams.

When fabricating these freestanding structures it is important to manage the release of the different beams to prevent beams collapsing onto each other. To do this, we mill in a single pass, with a long dwell time (200 µs per pixel, $3 \times 3$ nm pixel size), in a serpentine fashion, as shown in Figure 3.5, which shows the first rows of the milling pattern for a double-beam structure, with the blue dots indicating the

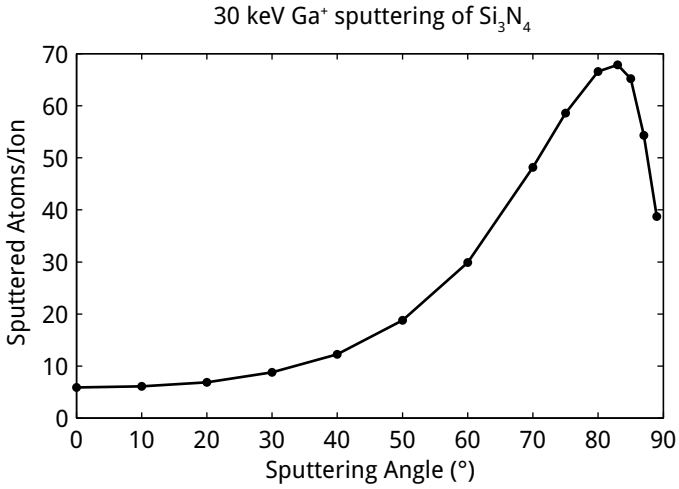


**Figure 3.6:** SRIM simulation of the sputtering rate in sputtered atoms per incoming ion as a function of the angle of the incoming ion beam, with normal incidence at 0°.

milling pixels, executed in the order indicated by the arrows. The gray rectangles indicate the resulting slots. This procedure keeps all the beams the same length during milling, preventing beam collapse.

The milling rate is strongly dependent on the angle at which the gallium ions hit the membrane. This is shown in Figure 3.6, which shows the sputter rate of $Si_3N_4$as a function of incident angle for 30 keV $Ga^+$ ions as calculated by the Stopping Range of Ions in Matter (SRIM) progam [101, 102]. This strong angle dependence implies that initially it will take relatively longer to penetrate the membrane (incident angle = 0°). Therefore the initial hole is created using a longer dwell time of up to 1000 µs per pixel. Subsequently, as the ions mill along the edge of the lengthening slot, the angle increases and the higher sputter rate allows for a shorter dwell time. Optimizing these dwell times decreases the overall milling time required to generate these structures and also decreases gallium contamination of the structures.

To mill the desired patterns, the FEI dual beam system was controlled using predefined 'streamfiles', which allow near-arbitrary pixel-by-pixel control over position, dwell time and blanking of the ion and electron beams. A streamfile consists of a three-line header, with the digital-analog-converter bit-depth used, the number of times to loop the streamfile's list of positions, and the number of lines in the streamfile. Following this are 3-row columns of dwell times (in units of 100 nanoseconds), x-positions and y-positions (the latter two in DAC bits). An optional fourth column can be used to blank and un-blank the beam. An example of a streamfile is:

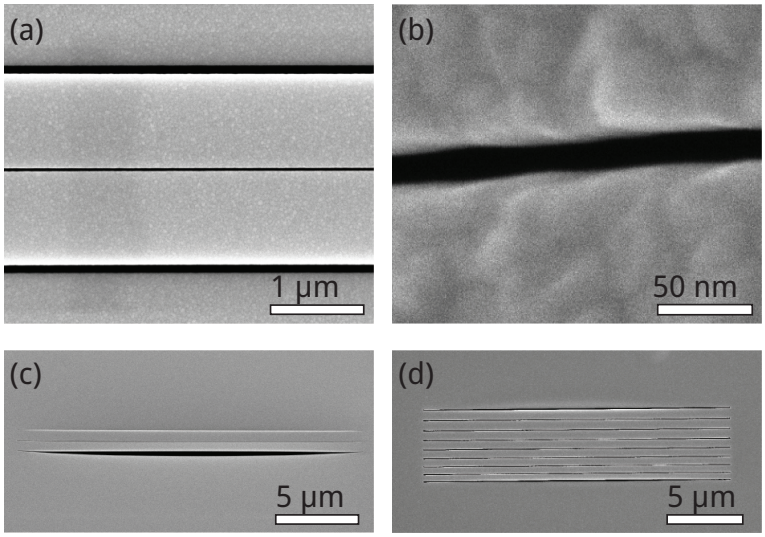


**Figure 3.7:** SEM images of FIB-milled beams in metal-coated silicon nitride. (a): Top-view of double-beam structure. (b): Center slot in double-beam structure, with ∼15 nm slit width. (c): Overview of double-beam structure, taken at an angle of 52°. (d): Overview of 8-beam array.

```
s16
2
478080
11000 27459 9728
11000 27467 9728
11000 27475 9728
11000 27483 9728
11000 27491 9728
...
...
```

A MATLAB script was written to calculate and export these streamfiles, based on the desired nanobeam sizes, allowing easy iteration to find the optimum milling parameters.

Figure 3.7 shows the results of this fabrication method. Figure 3.7a shows a top view SEM image of a double-beam geometry, in which two 1-µm-wide beams are separated by a 20 nm wide slit. A detailed view of a typical slit is shown in Figure 3.7b. Figure 3.7c shows a completed double-beam structure, composed of two 20-µm long beams. The image is taken under an angle of 52° and clearly shows the large gap at the side of the array, which is due to bending of the silicon nitride membrane. The beams themselves are straight and remain in the plane of the membrane, leading to very narrow gaps between the beams. These structures are

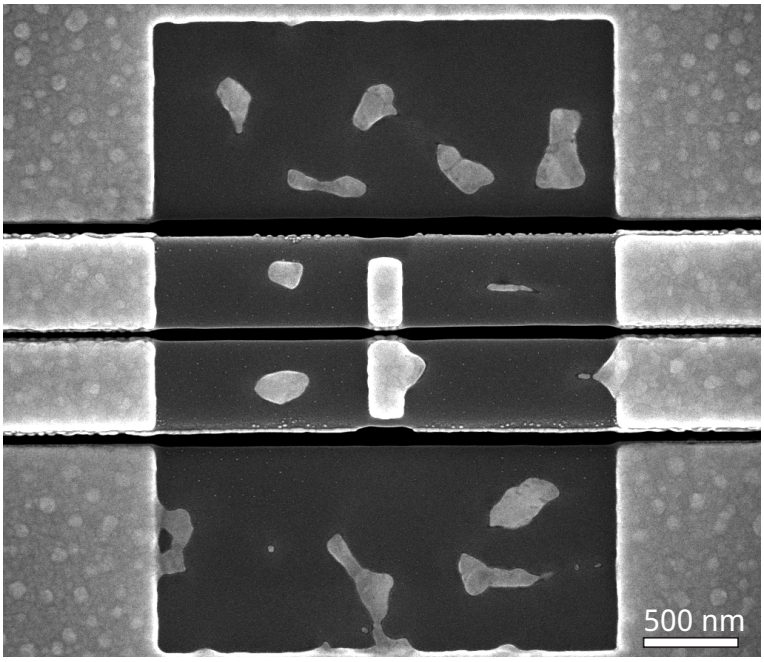


**Figure 3.8:** Double-beam structure with dimer antenna fabricated using FIB milling for beam release and antenna fabrication. Note the leftover grains of gold and the narrowing of the beams in the milled region.

investigated in Chapter 4. Figure 3.7d shows an array of 8 parallel beams with a length of 18 μm and beam widths ranging from 475 to 525 nm, investigated in Chapter 5.

## 3.3 Fabrication of single plasmonic antennas supported on nanobeams

A second geometry that was used in the experiments is composed of plasmonic dimer antennas, consisting of two dipolar scatterers, with each antenna element placed on an individual mechanical nanobeam, which we study in Chapter 6. This section describes two fabrication methods we used to fabricate these structures.

### 3.3.1 FIB milling of dimer antennas

The first method uses FIB milling not only to define the beams, but also to create antennas. We start with the same silicon nitride membranes as described in Section 3.2, and again use sputter coating to deposit 100 nm of gold on one side of

the membrane. To define the antenna, we mill from the same side as the gold was deposited. In a first milling step, we define the dimer antenna by milling a $2 \times 3$ µm area, leaving the antenna unmilled in the center. This requires careful tuning of the milling dose; too low doses leave many gold grains surrounding the antenna, causing unwanted light scattering. On the other hand, overmilling into the silicon nitride can damage the mechanical properties of the beams.

In the next step, we use the focused ion beam to release the beams. We milled the beams from the same side as the antenna. As a result, the gap between the antenna elements becomes slightly larger than the width of the slot between the beams. In addition to these milling problems, a disadvantage of this antenna design is that it leaves a large portion of the beam covered with gold. This greatly increases the effective mass of the oscillator, reducing the thermal fluctuations we want to probe.

### 3.3.2 Fabrication of antennas using electron-beam lithography

We then developed an alternative fabrication procedure for creating dimer antennas on nanobeams. First, we use electron-beam lithography, thermal evaporation of gold and liftoff to pattern antennas on a $Si_3N_4$ membrane. We create dimer antennas and longer single antennas. The dimer antennas are used for optical characterization, while the single antennas are used in fabricating antennas on beams. In the next fabrication step, we use focused ion beam milling to create two beams around the longer single antennas. In separating the beams we also divide the antenna in two elements, thus creating a dimer antenna. The final result is a structure with two beams, each with a dipole scatterer on top.

For antennas fabricated using EBL, we used low-stress silicon nitride membranes (Norcada, Inc.), of 100 nm thickness, with window sizes of either $0.5 \times 0.5$ mm, $1.0 \times 1.0$ mm or $1.5 \times 1.5$ mm, and large frames ($7.5 \times 7.5$ mm). We first attempted to create antennas on beams on high-stress membranes. However, when releasing the beams on these high-stress membranes, the membrane would break soon after beginning milling, possibly due to too high stresses around the initial milling opening. This problem is eliminated by using lower stress ($\sigma < 250$ MPa) silicon-rich membranes.

Table 3.1 shows the workflow used for electron-beam lithography of antennas on membranes; Figure 3.9 shows a schematic of these steps. To pattern the antennas we use the positive-tone resist ZEP520a, diluted 2:1 with anisole. To improve the wetting properties of the resist on the silicon nitride, the membranes are ozone-cleaned for 10 minutes and a layer of HMDS is applied. Because the frame size is still fairly small, getting the resist to spin coat to a uniform layer can be difficult. To control the spin coating process on the very small membrane samples we use a custom made sample-adapter, consisting of a PDMS gel-box glued onto a glass microscope slide. The membrane is mounted on the PDMS, and the spin coater

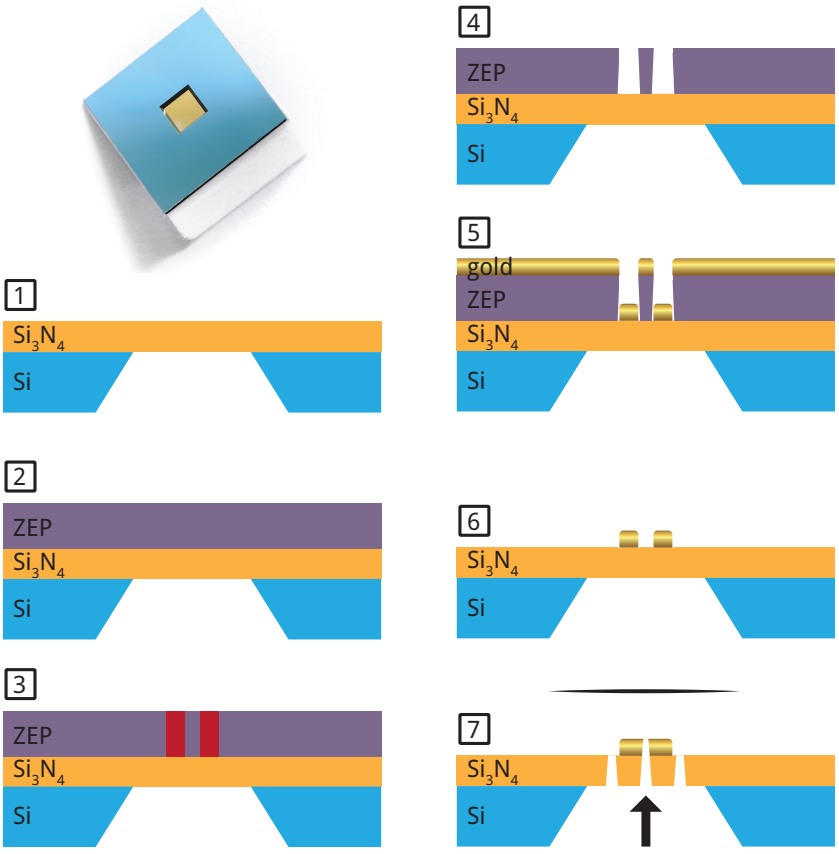


**Figure 3.9:** Electron-beam lithography workflow as used to fabricate dimer antennas on silicon nitride membranes. Top left: photograph of a 100-nm-thick 1.5-mm-square low-stress silicon nitride membrane suspended in a 7.5-mm-square silicon frame (Norcada, photo credit: Henk-Jan Boluijt). Fabrication steps depicted here are detailed in Table 3.1. Step 7 is the FIB milling step to create nanobeams and dimer antennas from single rods of double length.

| step | description | details |
|---|---|---|
| 1 | ozone clean | 10 minutes |
| | dry bake | 150° C, 5 minutes |
| | spin adhesion layer | hexamethyldisilazane (HMDS), 4000 rpm for 32 s, 2000 rpm/s acceleration |
| | bake adhesion layer | 150° C, 1 minute |
| 2 | spin resist | ZEP520A : anisole 2:1, 1500 rpm for 45 s, 500 rpm/s acceleration |
| | bake resist | 180° C, 5 minutes |
| 3 | electron beam exposure | 100 μm write field, aperture 10 μm area dose 100 μC/cm$^2$, line dose 250 pC/cm |
| 4 | develop resist | pentyl acetate, 90 s methyl isobutyl ketone (MIBK) & isopropyl alcohol (IPA), MIBK:IPA 9:1, 15 s IPA, 15 s |
| 5 | evaporate Ge & Au | argon plasma clean, 2 minutes 3-4 nm germanium, 35-40 nm gold |
| 6 | liftoff resist | *N*-methyl-2-pyrrolidone (NMP), 65 ° C. At least 2 hours, use syringe to aid liftoff Rinse in acetone and IPA, 15 s each |
| 7 | FIB milling | From reverse side. Current 9.7 or 28 pA. |

**Table 3.1:** Electron-beam lithography workflow. Step numbers refer to the schematic shown in Figure 3.9.

(Suss Delta 80) is first spun slowly to check the centering of the membrane window over the rotation axis of the spincoater. Membranes supported in 7.5 × 7.5 mm frames were used to increase the yield of the spin coating process.

For electron-beam exposure, development, evaporation, and liftoff, we mount the membranes in a custom holder (Figure 3.10) to increase ease of handling and reduce the risk of puncturing the membrane, and expose using a Raith e-LiNE system. Even though silicon nitride is an insulator, we do not apply a conductive coating to improve the electron-beam imaging and pattern writing. While charging is visible when focusing on the frame region of the sample, the thin $Si_3N_4$ layer only absorbs a small fraction of incident electrons, so that charging during pattern writing creates a negligible effect.

After exposure, the resist is developed, and Au is deposited using a thermal evaporator at a base pressure of $10^{-6}$ mbar. Before evaporation, we run an argon plasma for 2 minutes to clean the chamber and increase the adhesion of the surface. Then we evaporate 3-4 nm of germanium (as an adhesion layer) and 35-40 nm of gold.

After coating, the sample is placed in NMP for liftoff. Figure 3.11 shows an SEM

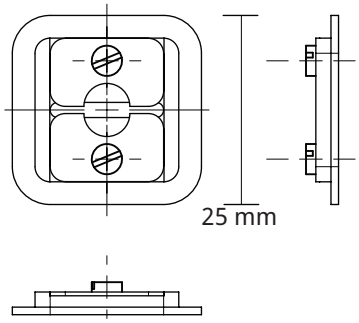


**Figure 3.10:** Sample holder for electron-beam lithography process (design: Henk-Jan Boluijt, AMOLF).

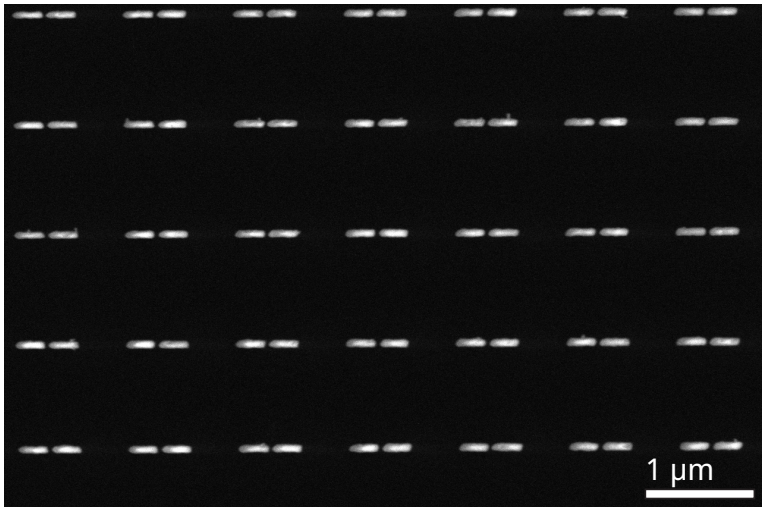


**Figure 3.11:** SEM image of a portion of a 70×70 µm array of 250×40 nm-size antennas, with a 30 nm gap between the elements, with the antennas placed at a 1 µm pitch in both $x$- and $y$-directions.

zoom image of a portion of a 70 × 70 µm array of 250 × 40 nm-size antennas, with a 30 nm gap between the elements, with the antennas placed at a 1 µm pitch in both $x$- and $y$-directions. These dimer antennas were used in optical transmission measurements, which are shown in Figure 6.2a.

Dimer antennas on double nanobeams were made by first fabricating single antennas of roughly the same length as a dimer antenna in Figure 3.11. The same electron-beam lithography and liftoff procedure as described above was used. After liftoff, the samples are mounted on an aluminum sample holder using copper tape (3M) for FIB milling. This holding plate is also used in the optomechanical

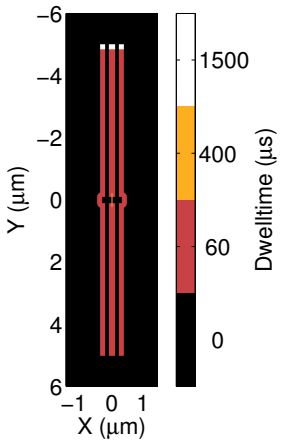


**Figure 3.12:** Pattern used for milling narrow beams for plasmonic dimer antennas. The color scale indicates the ion beam dwell time per pixel. Pixel spacing is 3 nm.

measurement setup, eliminating another sample handling step.

Next, we use FIB milling to create beams in the $Si_3N_4$ membrane using a current of 9.7 or 28 pA, with milling direction as indicated in panel 7 in Figure 3.9, milling the structures in a single pass. The antennas are on the top side of the membrane, to enable the EBL fabrication process. We mill from the reverse side, to protect the antennas from gallium contamination and to use the tapering inherent in FIB milling in our favor to create small antenna gaps. This process leads to both the creation of two beams and the cutting of the antenna into parts, to form the dimer antenna.

Figure 3.12 shows a schematic of a MATLAB-generated streamfile we use to control the ion beam, with a dwell time of 1500 µs/pixel for the initial hole, 60 µs/pixel for separating the beams, and 400 µs/pixel for the narrow gap between the antennas. The pattern uses a small pixel size of 3 nm, and the total milling time per structure is about 1 minute. Because the beams are only 120 nm wide, we leave an 'island' of silicon nitride to support the 250-nm-long antennas.

To align the pattern onto the pre-existing antennas, we use the electron beam in our dual-beam FIB system to image the antennas through the silicon nitride. This places high requirements on the alignment between the electron and ion beams. In practice, we use each milled structure to check the alignment, and if necessary we use the beam-shifting coils on the electron column to realign the beams.

Because the membrane is nonconductive, charging due to the ion beam can cause large beam drifts during milling. This drift is especially severe during the milling of the initial hole. We have obtained the best results by leaving the electron beam running in imaging mode, zoomed out enough to see the area of the complete structure, while milling the initial hole. After the ion beam has penetrated the

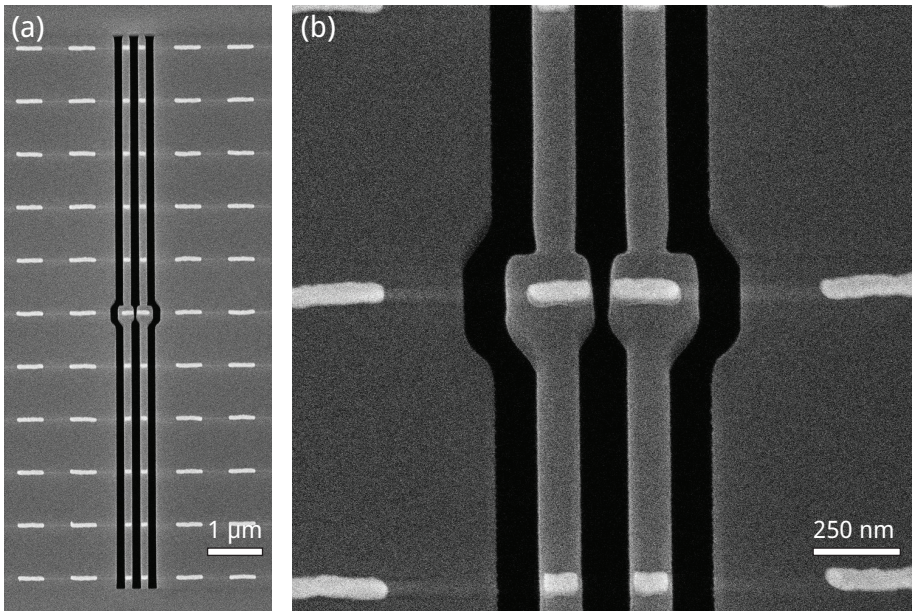


**Figure 3.13:** SEM images of dimer plasmonic antennas on nanobeams, fabricated using EBL and FIB. Panel (a) shows an overview of the complete structure. Panel (b) shows a zoom of the antenna region.

membrane, the electron beam is blanked. Once milling is complete, the structures are stable under electron-beam illumination, and do not stick together due to electron charging. Figure 3.13a shows a completed structure, and Figure 3.13b shows an image zoomed on the antenna region, showing that we can reliably fabricate dimer antennas (200 × 40 nm) on 10 µm long beams with a cross-sectional area of 100 × 120 nm.

# 4

# Measurement of nanomechanical motion using metal-insulator-metal plasmons

This chapter demonstrates plasmon–mechanical coupling in a metalized nanomechanical resonator. A surface plasmon polariton mode is excited in the 25-nm wide gap between two gold-coated silicon nitride beams. The strong plasmonic dispersion allows the nanomechanical beams' thermal motion at a frequency of 4.4 MHz to be efficiently transduced to the optical transmission, with a measured displacement spectral density of 40 fm/$\sqrt{\text{Hz}}$. Our results show that novel functionality of plasmonic nanostructures can be achieved through coupling to engineered nanoscale mechanical oscillators.

## 4.1 Plasmonic coupling

The experimental structure is composed of two parallel 20-μm-long and 1-μm-wide freestanding doubly-clamped 50-nm-thick $Si_3N_4$ beams, coated on one side with a 120-nm thick Au layer using sputter coating. The central gap width between the two beams is varied between 15 and 120 nm for different structures. A top-view scanning electron microscopy image of the structure is shown in Fig. 4.1a. Due to strong residual stress in the silicon nitride layer the membrane on the outer side of both nanobeams bends away, increasing the size of the two outer gaps, while the central gap keeps its width as fabricated. Figure 4.1d shows a magnified view of a structure with a 25-nm central gap size.

The relative mechanical motion of the nanobeams is probed by measuring the transmission of a laser beam that is incident normal to the sample, with its focus

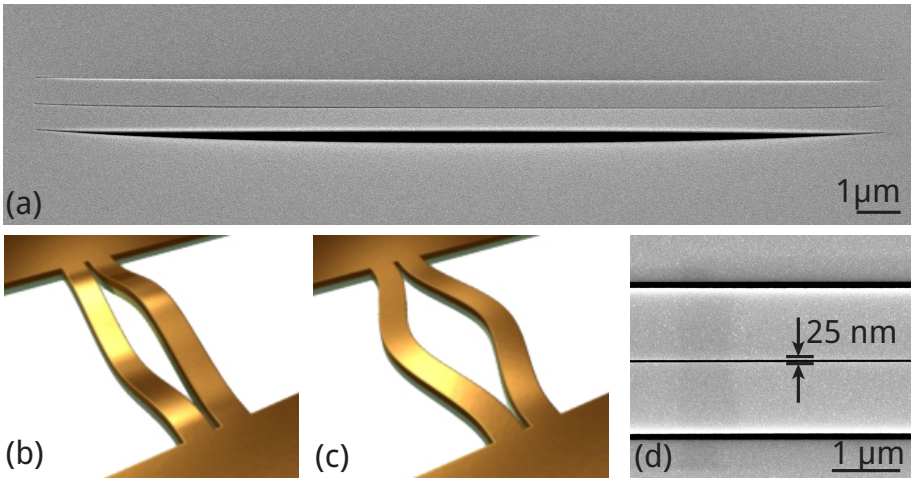


**Figure 4.1:** Plasmonic nanomechanical transducer geometry. (a): Scanning electron micrograph (incident angle 52°) of the double beam structure after fabrication. The two-beam structure is freestanding and lifted above the surrounding membrane due to mechanical stress in the latter. (b): Cartoon of the anti-symmetric out-of-plane mechanical mode of the double beam structure. (c): Cartoon of the anti-symmetric in-plane mechanical mode of the double beam structure. (d): Scanning electron micrograph (incident angle 0°) of the center part of the double beam, showing the 25-nm-wide central gap. The Au layer is visible as the grainy structure on top.

centered on the middle slit. The laser excitation generates metal-insulator-metal (MIM) plasmons that are confined within the 25-nm gap suspended by the Au layers. Figure 4.2a shows the calculated plasmon dispersion relation [103] for a semi-infinite gold-vacuum-gold MIM waveguide (see inset) for gap widths ranging from 120 nm to 10 nm. As the width of the insulator gap region is reduced, the plasmonic coupling between the two metal interfaces becomes stronger, increasing the wave vector and the effective index of the plasmonic MIM mode [62]. The reflection of the MIM plasmon at the upper and lower dielectric discontinuities defines an MIM Fabry-Pérot cavity. For this cavity, as well as for the propagating MIM mode, the plasmonic coupling between the two metal interfaces is dependent on the width of the insulator gap region, creating nanomechanical cavity resonance wavelength shifts.

## 4.2 Optical transmission spectra

Figure 4.3 shows optical transmission spectra for double-beam slits in the red and near-infrared spectral range, probing the plasmonic localized mode in the slit. Light from a fiber-coupled halogen lamp was focused on the central slit using

a confocal transmission microscope. The light is incident on the $Si_3N_4$ side of the membrane (see inset Fig 4.2b) to optimize impedance matching from the free-space incident beam to the MIM plasmon mode. The spot size diameter is about 1.5 μm. The light transmitted through the slit is spectrally analyzed using a fiber-coupled grating spectrometer equipped with a silicon deep-depletion CCD detector. A clear resonance is observed near 700-750 nm, with the spectral shape varying with gap width. The transmitted intensity increases with gap width and shows a blue-shift of the peak resonance wavelengths with increasing slit width, both in agreement with the calculations shown in Fig. 4.2b.

## 4.3 Finite-difference time-domain simulation

Figure 4.2b shows a 2D finite-difference-time-domain simulation (Lumerical Solutions) of the transmission through the 120-nm long MIM waveguide (see inset). Several characteristic resonant features are seen in the transmission spectrum. In the range 700–800 nm, a resonant Fabry-Pérot mode is observed that results from the reflection of the MIM plasmon at the upper and lower dielectric discontinuities defining the MIM cavity. As the gap width is reduced, the plasmon wave vector increases and the resonance redshifts. The inset in Figure 4.2c shows the field distribution at 750 nm for a 20 nm gap width, corresponding to the first-order ($n = 1$) Fabry-Pérot resonance that occurs when the cavity length is equal to one-half of a plasmon wavelength, taking into account the phase jump at the interfaces [104]. Note that the strong resonance shift with gap width in this plasmonic MIM cavity geometry is due to the strong sensitivity to dispersive plasmonic effects rather than being linearly linked to a mirror displacement as is the case in conventional optomechanical Fabry-Pérot cavities. Figure 4.2c shows the simulated center frequency and relative shift of the $n = 1$ Fabry-Pérot resonance frequency for different gap widths. From the data shown in Fig. 4.2b, we extract the peak positions of the $n = 1$ resonance and calculate $G$, the optical frequency shift per unit displacement, with units of [Hz]/[m], to derive many optomechanical interaction parameters. For instance, the radiation pressure exerted by the plasmonic mode on the mechanical oscillator is $\hbar G$ per photon. For gaps smaller than 40 nm, the simulated optomechanical coupling constant is larger than 2 THz/nm, which is larger than has been shown in any optomechanical system to date: for Fabry-Pérot cavity systems the frequency shift is limited to $G = \omega_c/L$, which typically ($\omega_c = 2\pi \times 300$ THz, $L = 25$ mm [105]) gives a frequency shift on the order of 10 MHz/nm. For photonic crystals, a frequency shift of 350 GHz/nm has been shown [106], and for nanoscale GaAs disk resonators, a frequency shift of $G = 450$ GHz/nm has been shown [18]. At longer wavelengths, the $n = 0$ plasmonic mode is excited, which modulates the transmitted intensity as a function of gap width, as shown in Figure 4.2d.

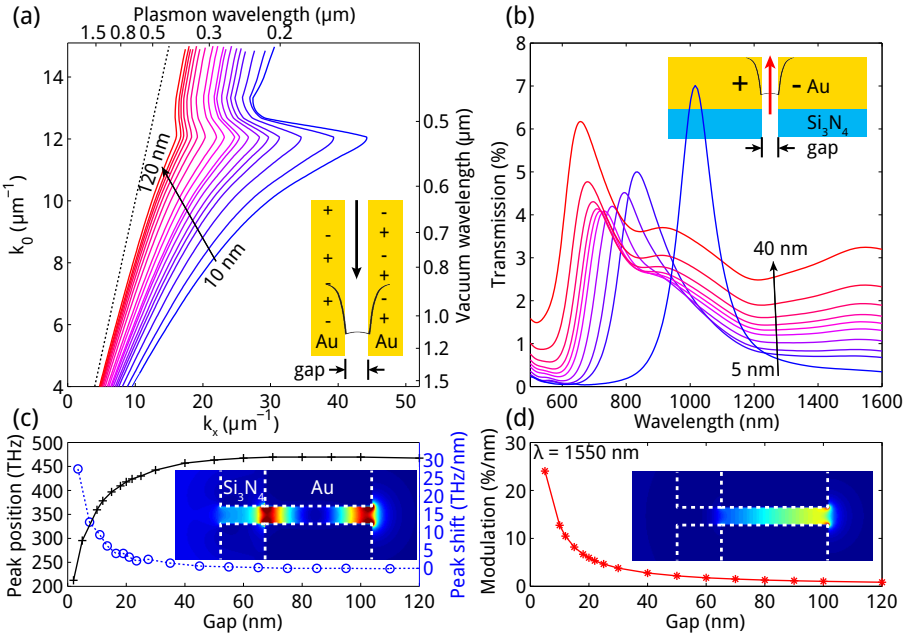


**Figure 4.2:** Dispersion of metal-insulator-metal plasmons. (a): Calculated dispersion relation for a gold-air-gold metal-insulator-metal (MIM) waveguide, shown schematically in the inset, with the mode profile indicated in black. The width of the air gap ranges from 10 nm (blue) to 120 nm (red). The light line is indicated by the dashed black line. (b): Simulated (FDTD) transmission through a 120 nm long MIM cavity, as shown in inset, with gap widths from 5 nm to 40 nm. (c): Calculated resonance frequency as a function of gap width for the $n = 1$ Fabry-Pérot mode (black) and differential peak shift (blue) at each gap width. (d): Calculated modulation of transmission for the $n = 0$ mode at $\lambda = 1550$ nm. The insets in (c) and (d) show the electric field intensity $|E|^2$ of the two modes for a gap width of 20 nm.

## 4.4 Measurement of mechanical modes

To investigate the transduction of the nanomechanical motion to the optical signal, we use the experimental setup described in Chapter 3. A narrowband laser is focused through the center slit of a double beam structure, with TM polarization, exciting MIM plasmons. The transmission is detected on a fast photodiode.

Figure 4.4a shows the frequency spectrum of the signal transduced by the plasmonic nanocavity. Four mechanical resonances are clearly observed, at $f = 2.75$, 4.4, 4.6, and 5.8 MHz. To corroborate the mechanical nature of these resonances, we fabricated a series of beams with lengths between 12 and

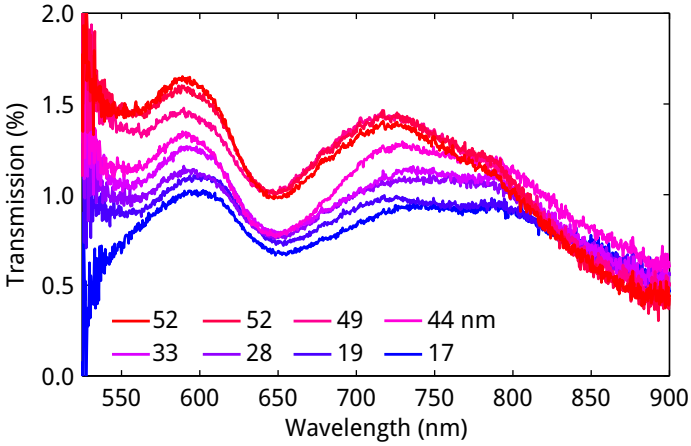


**Figure 4.3:** Optical transmission spectra of double-beam structures in the NIR wavelength range. A series of beams with different center widths (indicated by the different colors) was fabricated, and transmission was measured using a confocal microscope.

25 µm. For all these beams, we measured spectra similar to the one shown in Figure 4.4a and extracted the mechanical resonance frequencies, which are plotted in Figure 4.5. These measured eigenfrequencies show good agreement to finite-element-method (COMSOL) simulations of the mechanical eigenfrequencies of the beams as shown in Figure 4.5, assuming a reasonable value for the stress in the $Si_3N_4$ membrane ($\sigma$ = 700 MPa). This simulation also allows us to identify the nature of the mechanical eigenmodes at the different resonant frequencies, with corresponding FEM simulations inset in Figure 4.4a. We find that the modes near 2 MHz correspond to out-of-plane oscillation of the beams (sketched in Fig 4.1b), while modes in the 4–5 MHz spectral range are due to in-plane oscillation of the beams (Figure 4.1c). The 5.8 MHz resonance matches the second-order out-of-plane mode.

Figure 4.4a also shows a reference measurement taken on a $Si_3N_4$ beam structure without gold film. Manufacturing narrow slits in the $\sigma$ = 700 MPa membranes without gold coatings was unsuccessful: the beams collapsed onto each other during milling, due to the high stress in the membrane. However, this structure was successfully milled in a lower-stress membrane, with $\sigma \approx 200$ MPa. From FEM simulations for this geometry the lowest-order out-of-plane and in-plane modes would be expected at 4.41 and 18.5 MHz, respectively. No mechanical modes are observed, clearly demonstrating that detection of mechanical motion observed in the metallic beams is due to MIM plasmons in the narrow metal gaps.

Figure 4.4b shows a more detailed view of the resonant modes at $\nu$ = 4.447 MHz and 4.566 MHz. The observation of the doublet resonant modes is attributed to

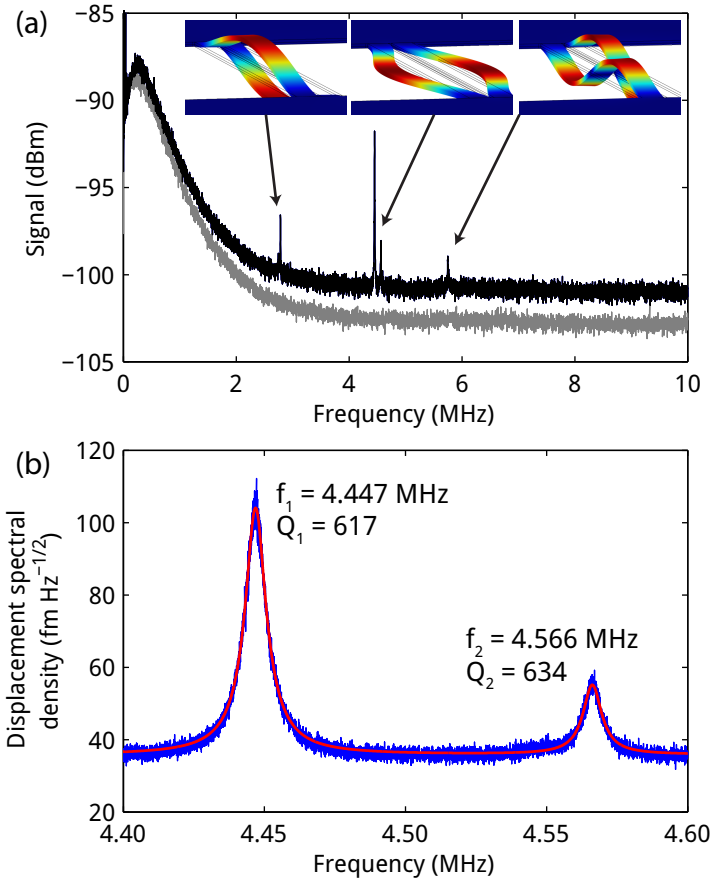


**Figure 4.4:** Nanomechanical frequency spectra of plasmonic nanoresonators measured at $\lambda$ =1550 nm. (a): Black line: Mechanical spectrum measured using a spectrum analyzer. Four mechanical resonances are visible, at $\nu$ = 2.8, 4.5, 4.6 and 5.75 MHz. The broad peak centered at 250 kHz is attributed to laser classical noise. The insets show FEM simulations of the associated mechanical modes. Gray line: mechanical spectrum of a reference sample, consisting of a double beam structure in low-stress (200 MPa) silicon nitride without gold, vertically shifted by −3 dBm. No mechanical resonances are observed. (b): Higher RBW measurement of the mechanical resonances around 4.5 MHz. The data very well fit a double-Lorentzian line profile superimposed on a constant background representing the classical noise, shot noise and electrical noise. The lower and higher frequency resonances have quality factors $Q = 617$ and $Q = 634$, respectively. The signal amplitude corresponds to an RMS mechanical amplitude $x_{\mathrm{rms}}$ = 10.4 pm, in agreement with theory, demonstrating the high displacement sensitivity of the plasmonic nanocavity.

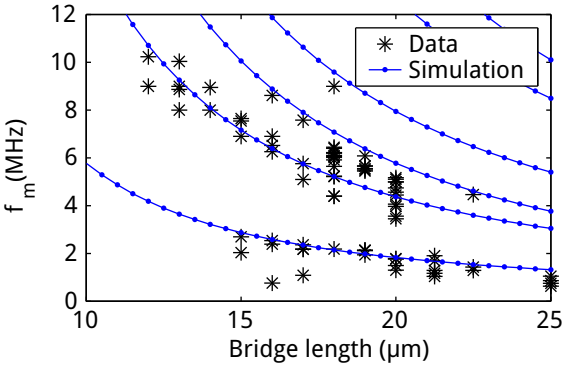


**Figure 4.5:** Measured eigenfrequencies for beams of different lengths (black stars), compared to eigenfrequency values extracted from FEM simulations.

the lifting of the degeneracy of the double-beam resonant modes by small differences in beam sizes resulting from slight differences in the ion milling parameters. Lorentzian line shapes are fitted through the resonances, in combination with a constant background due to classical noise, shot noise and electrical noise, as discussed in Chapter 2. Good agreement with the data is observed, with quality factors of Q = 617 and 634, respectively, for the two modes. These values being close again testifies to the degenerate nature of the two resonant modes. The mechanical quality factor is limited in these structures by the large amount of gold on the beams. By depositing gold only in the optically probed region of the beams, the quality factor could likely be improved [107]. In Section 5.5, we will show that this is indeed the case for an array of nanobeams.

## 4.5 Transduction

From the Lorentzian line fits the energy stored in each mechanical mode is determined. Dividing by the known DC electrical power output from the detection photodiode a signal modulation depth of $5.2 \times 10^{-4}$ is found. Using the simulated intensity modulation of 0.05/nm at $\lambda = 1550$ nm for a gap width of 20 nm (Fig. 4.2c) this corresponds to a RMS amplitude of the mechanical mode of $\delta_{\mathrm{rms}} = 10.4$ pm. From the equipartition theorem we find the root-mean-square displacement:

$$\delta_{\mathrm{rms}} = \sqrt{\frac{k_B T}{m_{\mathrm{eff}} \Omega_{\mathrm{m}}^2}} = 15\,\mathrm{pm}, \tag{4.1}$$

assuming an effective mass $m_{\mathrm{eff}} = 42.5$ pg calculated from the bridge geometry, in good agreement with the measurement given the uncertainties in material pa-

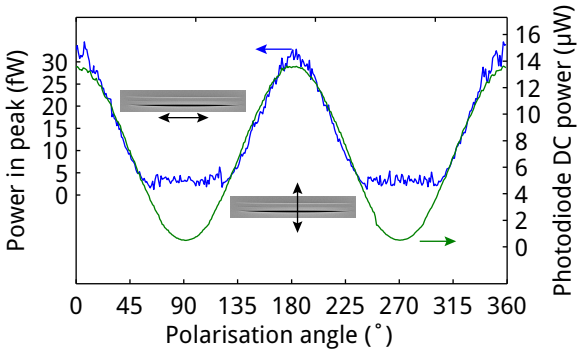


**Figure 4.6:** Measured mechanical signal (blue line) and transmitted optical power (green line) as a function of the polarization of the incident beam at $\lambda = 1550$ nm. The polarization angle relative to the beam structure is indicated in the insets of the plot.

rameters. These data demonstrate the high displacement sensitivity of the plasmonic nanocavities. Using this calibration, we calibrated the spectrum shown in Figure 4.4b to a displacement spectral density, expressed as $\sqrt{S_{xx}(\Omega)}$, showing an imprecision of about 40 fm/$\sqrt{\text{Hz}}$.

We have also compared these data to the modulation expected from a knife-edge modulation, as discussed in section 2.7. In the naive approach, taking only the geometric width change into account without any resonant effects, the transmitted intensity scales with the gap width, leading to a modulation of $\delta x / x_0$. For the measured transduction at $\lambda = 1550$ nm, these values are close to each other. However, near the resonance at 780 nm, plasmonic transduction offers higher sensitivity. This can be understood from Fig. 4.2b, as the transduction benefits especially from strong plasmonic mode dispersion with the laser tuned to the side of the resonant peak.

To further verify that the optomechanical spectra shown in Figure 4.4 are due to cavity plasmonic resonances, we studied the dependence of the optomechanical spectra and the DC transmission background on incident polarization, while keeping the incident power constant. Figure 4.6 shows the optomechanical resonance peak intensity for the resonance at 4.447 MHz and transmitted DC power as a function of polarization angle. A sinusoidal trend is observed with maxima and minima for TM and TE polarization, respectively, directly proving the plasmonic nature of the coupling mechanism. For TE polarization, the mechanical peak is no longer visible above the detector noise background.

We have also systematically varied the gas pressure in the measurement chamber: the signal gradually reduces and the linewidth increases for increasing pressures as shown in Figure 4.7, with blue circles indicating the linewidth and black stars the signal-to-noise ratio as a function of vacuum pressure. The linewidth

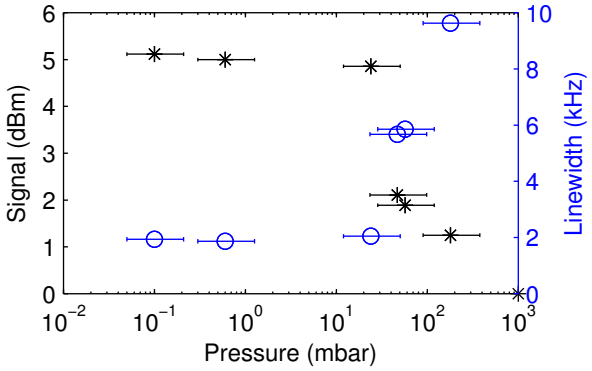


**Figure 4.7:** Pressure dependence of signal and linewidth measured for the out-of-plane resonance at ≈ 2.1 MHz for the double beam structure. Black stars: signal amplitude, blue circles: linewidth. Note the strong change as a function of chamber pressure above 10 mbar.

broadening and reduction in amplitude shows that the signal is indeed mechanical in origin.

## 4.6 Conclusion

In conclusion, we demonstrated a plasmonic optomechanical resonator with high displacement sensitivity. Light is coupled to plasmonic localized Fabry-Pérot resonances that show large amplitude modulation with small mechanical displacements of the cavity, with an optomechanical coupling constant larger than 2 THz/nm. We detect the fundamental cavity mechanical mode with $\nu = 4.447$ MHz and $Q = 617$ and determine an RMS amplitude of the mechanical mode as small as $\delta_{\mathrm{rms}} = 10.4$ pm, with a displacement sensitivity of 35.8 fm/$\sqrt{\mathrm{Hz}}$. These plasmonic nanocavities provide a rapid, effective and ultra-sensitive readout method of nanoscale mechanical motion that could be of use in both fundamental and applied studies, in which nanomechanical systems act as transducers, sensors or active elements.

# 5

# Parallel plasmo-mechanical transducer array

Arrays of nanomechanical resonators have many applications, ranging from force and mass sensing [1, 2] to collective nonlinear dynamics [108] and mechanical memories and computing [109]. In particular, large numbers of integrated mechanical sensors can enable sensitive, rapid, label-free and massively parallel detection of biochemical species and trace gases [110, 111]. By varying the frequency of the oscillators in an array, the sensing bandwidth can be effectively increased. Parallelization can also address some of the difficulties associated with scaling down mechanical oscillator size, which is generally favorable for sensitivity: difficulties that include reduced power handling capability [112, 113] and reduced effective interaction cross section (i.e. the sensor surface area). Another challenge that nanoscale mechanical systems pose is how to efficiently transduce mechanical motion to a measurable signal, crucial to any sensor's operation.

In the case of a sensor consisting of multiple mechanical oscillators, it is often useful to create a system that can be measured using a single input and single output, as described in [114], by separating the oscillators in frequency. Mechanical arrays have been demonstrated using various readout schemes: electrical readout [115], using optical diffraction [116], and using (deformable) optical waveguides [39].

Here, we demonstrate the parallel transduction of the motion of an array of nanobeams using a single laser beam focused on the array. The transduction is mediated by surface plasmon resonances in the narrow metal-coated slots between the nanobeams, as discussed in detail in Chapter 4, can be extended to measuring individual mechanical resonator modes in an array of nanobeams.

The small size of plasmonic resonators allows high mode overlap with nanomechanical modes. At the same time, the free-space addressability of localized surface plasmon resonances allows the use of simple optical elements to couple light

to and from the cavity, without having to resort to for instance nanoscale positioning of waveguides, as is necessary for many photonic crystal cavity [35] and microcavity [21] optomechanical implementations. This free-space addressability makes measuring multiple mechanical oscillators with a single laser beam a relatively straightforward process.

During the measurement, the beams absorb some of the incident light. We demonstrate that this leads to photothermal modification of the beams' eigenfrequencies [117–120]. At high enough driving powers, the photothermal heating can parametrically amplify the motion of the beams. This photothermal amplification effect has been observed in a variety of optomechanical systems: in metal-coated cantilevers [12, 121], in semiconductor membranes using electron-hole pair relaxation [122], and in microdisks [123]. Photothermoelastic interactions may thus allow for both tuning and actuation in these systems. Finally, we discuss the mechanical coupling between the nanobeams and show a fabrication technique to improve the mechanical quality factor of the system.

## 5.1 Experimental methods

To fabricate arrays of parallel mechanical nanobeams, 110 nm of gold is sputter coated on commercially available high-stress stoichiometric silicon nitride membranes of 50 nm thickness (Norcada, Canada). Using a focused ion beam (30 keV Ga+ ions, current 10 pA), we mill 9 18-μm-long slits in a single pass, creating 8 nanomechanical beams, each separated by a slit width of 20 nm. The beam widths are fabricated to range in incrementing steps from 475 to 550 nm wide. The difference in beam widths lifts the degeneracy of the in-plane eigenfrequencies and allows the identification of individual beams from the transduced mechanical spectrum. The out-of-plane mechanical eigenfrequencies are to first order indepedent of beam width, and are therefore more difficult to separate spectrally. However, the out-of-plane and in-plane eigenmodes are well separated in frequency ($\sim 2.2$ and $\sim 3.7$ MHz respectively), and we will mostly consider the latter below.

Figure 5.1a shows a scanning electron microscopy (SEM) image of the fabricated array, taken with the gold-coated side of the membrane upward and the sample tilted at 52°. The narrow gaps between the nanobeams are clearly visible; a larger gap is seen for the two outer sides, where the silicon nitride membrane bends downwards due to its in-plane stress.

The sample is then placed in a custom-built confocal transmission microscope, as described in Chapter 3. A 1550 nm wavelength CW erbium-doped fiber laser is focused onto the sample, polarized orthogonal to the slits, and incident from the gold-coated side of the nanobeams, as shown in the schematic cross section in Figure 5.1b. Different focusing conditions were used, as will be described later on.

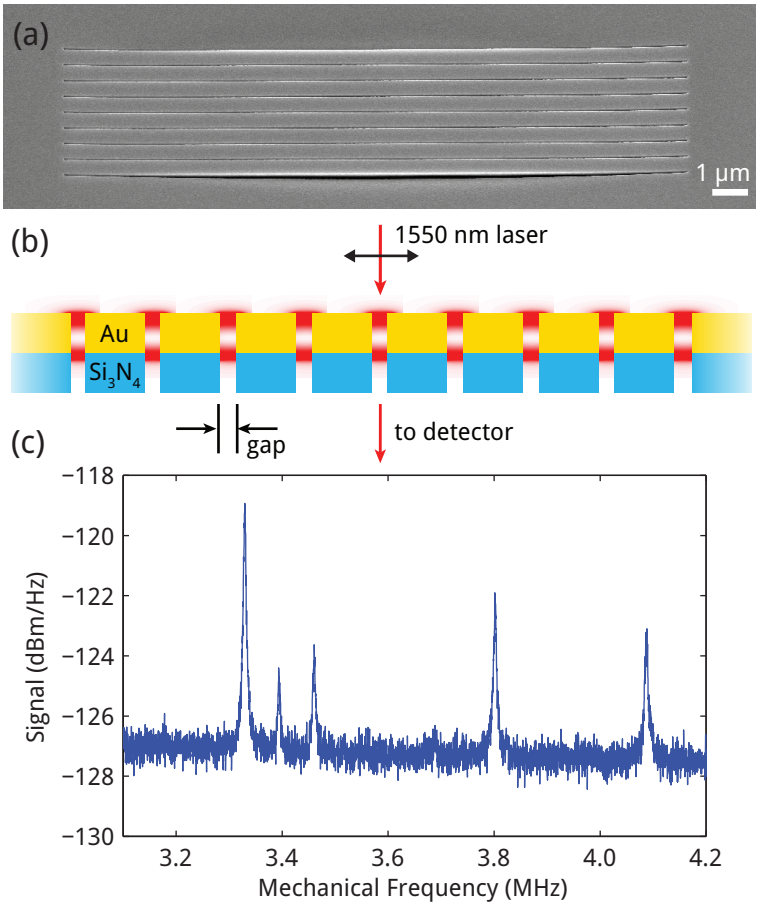


**Figure 5.1:** Experimental geometry. (a): SEM micrograph of array structure, tilted at 52°, taken on the gold side of the array (beam length: 18 µm, thickness: 50 nm $Si_3N_4$, 110 nm Au, beam widths: 475 to 550 nm, gap width: 20 nm). (b): Schematic cross section of the nanomechanical beam array. Red spots indicate plasmonic Fabry-Pérot resonances excited in the slits between the Au layers by a 1550 nm CW laser. (c): Frequency spectrum of light intensity transmitted through the array, showing 5 distinct resonances caused by 5 of 8 nanomechanical beams in the array.

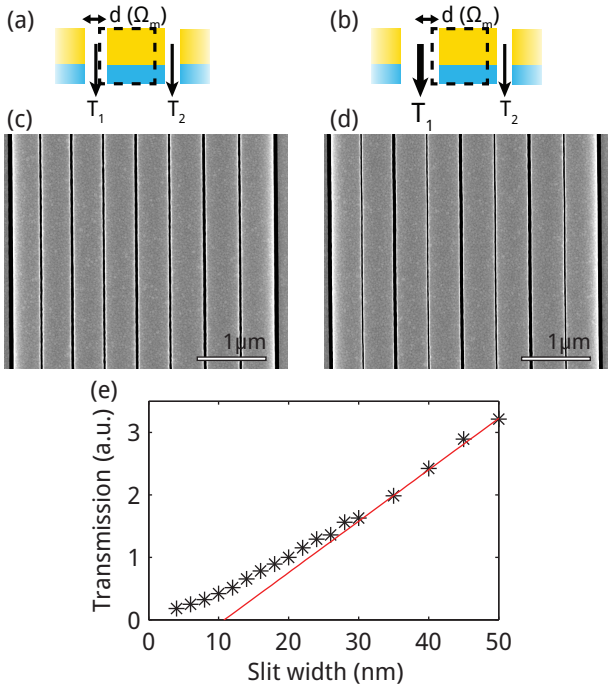


**Figure 5.2:** Parallel mechanical transduction. (a), (b): Schematic of transduction through (a) constant-width and (b) alternating-width gaps. SEM micrographs of center of arrays of (c) constant-width gap (20 nm) and (d) alternating-width gap (20 nm and 50 nm) array structures. (e) Transmission through slit as a function of slit width $d$, extracted from FDTD simulations. The red line is a linear fit to the transmission through slits of width greater than 35 nm.

## 5.2 Nanomechanical transduction

Mechanical displacement affects the optical response of the slots, changing the transmitted power. In the present geometry, the motion of 8 parallel nanobeams is measured simultaneously. Figure 5.1c shows the frequency spectrum measured by defocusing the laser beam to a spot diameter of ~ 5 μm, so that all plasmonic gaps are illuminated, and detecting a power of approximately 12 μW. The peaks are related to the thermal motion of individual mechanical modes. Interestingly, only 5 resonant mechanical modes are observed in the spectrum, with varying amplitude. To analyze this, we first analyze how the motion of the 8 beams is transduced to the measured intensity.

The motion of each of the beams is probed by its two adjacent slits, each of which supports a plasmonic resonance. The transmitted power through each slit is given by $\eta(d_i)\mathscr{P}_i$, where $\mathscr{P}_i$ is the optical power density (in W/m$^2$) interacting

with the slit and $\eta(d)$ is an effective scattering cross section into the transmission channel, which is a function of the slit width $d_i$.

For in-plane motion, the two slits at either side of the beam have widths $d_1(x) = \bar{d}_1 + x$ and $d_2(x) = \bar{d}_2 - x$, respectively, where $\bar{d}_i$ denotes the mean width of slit $i$. The total transmitted power is as such $T = \eta(\bar{d}_1 + x)\mathscr{P}_1 + \eta(\bar{d}_2 - x)\mathscr{P}_2$. This power is modulated through oscillations of the beam, as to first (linear) order

$$\frac{\mathrm{d}T}{\mathrm{d}x} = \frac{\mathrm{d}\eta}{\mathrm{d}x}(\bar{d}_1)\mathscr{P}_1 - \frac{\mathrm{d}\eta}{\mathrm{d}x}(\bar{d}_2)\mathscr{P}_2. \tag{5.1}$$

The slit widths are modulated by the displacement $x$ of the beam (we take the mean displacement $\bar{x} = \langle x(t)\rangle = 0$).

For a plane wave incident on a nanobeam surrounded by two identical slits, this would lead to completely vanishing transduction of motion as $\bar{d}_1 = \bar{d}_2$ and $\mathscr{P}_1 = \mathscr{P}_2$. Figure 5.2a shows a schematic of this geometry. An SEM image of such an array is shown in Figure 5.2c.

We can also describe this vanishing $\mathrm{d}T/\mathrm{d}x$ using a symmetry argument: there is a symmetry axis through the center of the beam. This implies that $\mathrm{d}T/\mathrm{d}x = \mathrm{d}T/\mathrm{d}(-x)$, which must be equal to 0. However, if we break the symmetry, for instance by changing the width of the two slits, the derivatives can be different: $\mathrm{d}T/\mathrm{d}x \neq \mathrm{d}T/\mathrm{d}(-x)$. This also holds for more complicated optical modes, for instance if the modes are (optically) coupled across multiple beams.

Two factors can potentially break down this expectation and lead to a resonance peak: (1): a different input power density $\mathscr{P}$ on the two slits, due to the fact that a non-uniform (for instance, a focused) beam is used, and (2) a difference in slit widths $\bar{d}_1 \neq \bar{d}_2$. Because the plasmonic coupling strength is dependent on the slit width, $\eta$ is not linearly dependent on $d$, such that $\frac{\mathrm{d}\eta}{\mathrm{d}x}(\bar{d}_1) \neq \frac{\mathrm{d}\eta}{\mathrm{d}x}(\bar{d}_2)$ if $\bar{d}_1 \neq \bar{d}_2$.

This implies that by changing the width of the slit on either side of a beam, we can allow transduction of motion to transmitted power. Importantly, it is the nonlinear dependence of slit transmission $\eta$ on slit width $d$ (or on slit area, for that matter), that is crucial to allow transduction. Such a strong dependence on slit width, shown in Figure 5.2e, is a defining characteristic of plasmonic response. In this figure, the black data points are the transmission extracted from a series of FDTD simulations of slits of differing widths. The transmission is normalized to the transmission through the 20-nm-wide slit. The red line is a linear fit to slits of widths between 35 and 100 nm, showing the nonlinear behaviour of the plasmonic transmission for slit widths narrower than 30 nm.

In the structure of Figure 5.1 differences between slit widths are caused by fabrication imperfections, allowing observation of the motion of some of the beams in Figure 5.1c. The outermost slits in the structure are much wider: in-plane stress in the silicon nitride causes bending in the membrane surrounding the array structure, leading to a resonance peak for the two outermost beams. For some of the inner beams, the surrounding slits are also slightly different.

Next, we study the transduction for an an array in which the slits were intentionally made alternately narrow (20 nm) and wide (50 nm), shown schematically

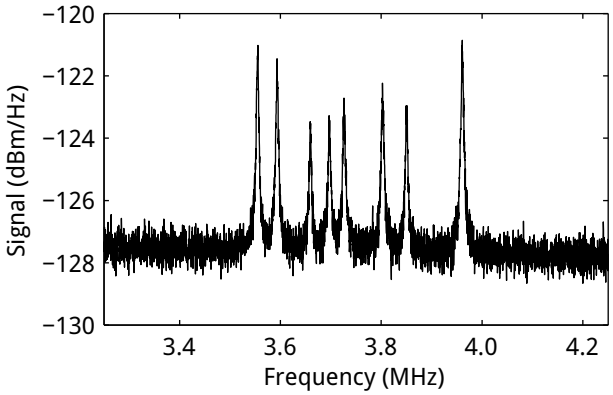


**Figure 5.3:** Frequency spectrum of light transmitted through an array with 8 beams, with alternating-width slits of 20 and 50 nm, with beam widths ranging from 475 to 525 nm. The laser beam was defocused to a spot size of $\sim 5$ µm.

in cross section in Figure 5.2b and in an SEM image in Figure 5.2d. For these structures, we expect that $\frac{\mathrm{d}\eta}{\mathrm{d}x}(\bar{d}_1) \neq \frac{\mathrm{d}\eta}{\mathrm{d}x}(\bar{d}_1)$ for all beams, based on finite-difference-time-domain simulations of metal-insulator-metal slits of varying width (Figure 5.2e). Therefore, the motion of all beams is expected to be transduced. At the laser wavelength of 1550 nm, we find from the FDTD simulations that $\frac{\mathrm{d}\eta}{\mathrm{d}x}(20\text{ nm}) = 1.1\,\frac{\mathrm{d}\eta}{\mathrm{d}x}(50\text{ nm})$.

We again measured the transduction with a defocused beam, and simultaneously detected the modulations induced by 8 beams with widths ranging from 475 to 525 nm. This time, we achieve parallel transduction of motion of all 8 beams, as shown in Figure 5.3, when we detect a power of 15 µW. This shows that using alternate slit widths (20 nm and 50 nm) is a viable method to enable parallel transduction of the motion of 8 parallel resonators using a single focused laser beam.

To further investigate the transduction of each beam by its two neighbouring slits, we perform measurements in which both structures were scanned through the focus of a laser beam ($2.48 \pm 0.06$ µm FWHM for the constant-width array, $2.84 \pm 0.13$ µm for the alternating-width array), scanning orthogonal to the long axis of the beams.

Figure 5.4a and b show color plots of the spectral density of transduced power as a function of the position of the laser beam across the constant-gap-width and alternate-gap-width arrays respectively. Eight different curves are now clearly resolved for both structures, each corresponding to the motion of an individual nanobeam. Interestingly, as the laser beam is scanned across a single nanobeam, the mechanical resonance wavelength decreases and increases. This will be discussed further in Section 5.3.

Another striking feature in the transduction spectra in Figure 5.4a is that the

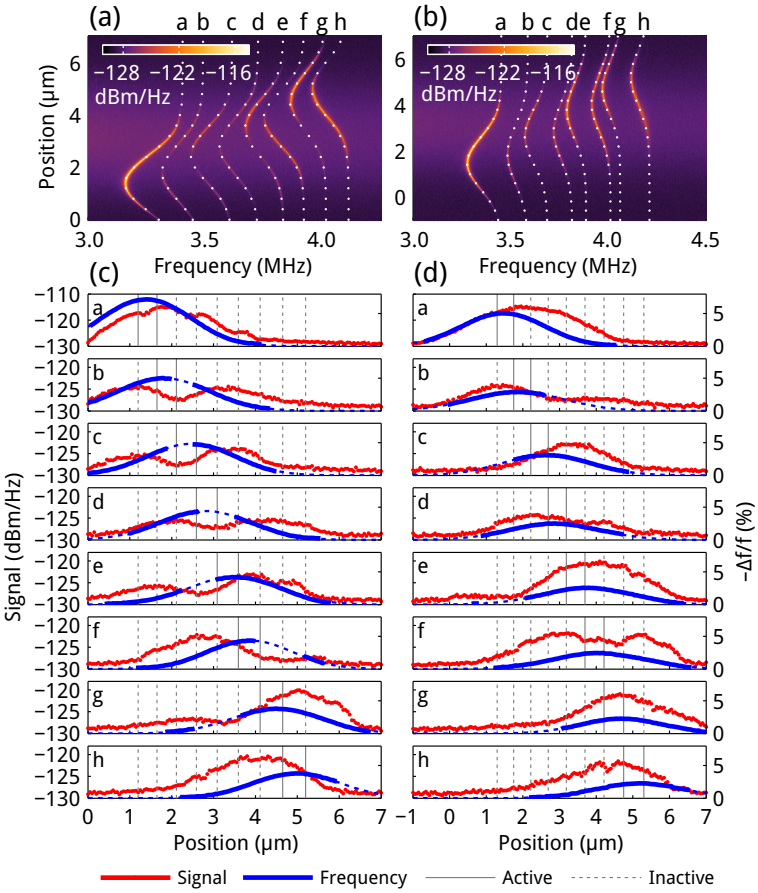


**Figure 5.4:** Mechanical resonance intensities. (a) Linescan across the center of an array of 8 nanobeams separated by a fixed width of 20 nm. The peak resonance frequency is plotted on the horizontal axis, and the resonance peak intensity is represented by the color scale. Dots indicate Gaussian fits to peak frequencies as a function of laser focus position on the array. (b) Similar as in (a), for an array with beams alternately separated by 20 and 50 nm. (c) Transduction curves extracted from (a): the resonance peak intensity intensities are shown as a function of laser spot position (red dots), along with the peak resonance frequencies (blue line). A dashed line indicates that the signal was too low to extract for use in fitting. The gray vertical lines indicate the positions of the slits, with the solid lines indicating the slits next to the beam for which the transduction is plotted. (d) Transduction curves extracted from (b). The focal diameters, 2.48 ± 0.06 μm FWHM for (a), 2.84 ± 0.13 μm for (b), were determined from the average width of the Gaussian fits. Laser power detected was 11.5 μW for (a), (c) and 10.5 μW for (b), (d).

intensity shows clear dips close to the center for all beams, except for the two outermost ones. The red data points in the subpanels of Figure 5.4c show the mechanical transduction power at resonance for each laser beam position. Each subpanel shows data for a single beam. The transduction curves clearly show dips in transduction for the 6 center beams when the focal spot is close to the center of each beam, when $\mathscr{P}_1 = \mathscr{P}_2$, implying a vanishing transduction, and showing that $\bar{d}$ is very similar for the seven center slits.

The mechanical transduction for each beam in the alternate-gap-width array is plotted in Figure 5.4d. The dips in the transduction are now much less pronounced compared to those observed for the constant-width array shown in Figure 5.4a and c, and are in fact absent in most cases, showing that $\frac{\mathrm{d}\eta}{\mathrm{d}x}(50\,\mathrm{nm}) \neq \frac{\mathrm{d}\eta}{\mathrm{d}x}(20\,\mathrm{nm})$.

The measurements in Figures 5.3 and 5.4 provide direct proof that the transduction through the arrays is due to a plasmonic effect. If the transmission through the slits were simply due to a geometric effect, i.e. a transmission that is linearly proportional to the slit width, we would not observe any transduction of motion: for in-plane motion, the total width of the 2 slits surrounding a nanobeam is constant, and therefore no transduction would be expected. However, the plasmonic resonance mediating the transmission through the slit will lead to nonlinear dependence of transmission on slit width (as shown in Figure 5.2e, allowing the alternate-slit-width structure to improve transduction of the in-plane mechanical mode, and precludes the observed effects being due to a purely geometric modulation of the transmitted light by the beams' motion.

## 5.3 Thermal tuning of eigenfrequencies

Figure 5.4 shows that the mechanical eigenfrequencies of the beams depend strongly on their position relative to the laser spot. We ascribe this to a photothermal effect: heating-induced expansion of the tensile-stressed beams leads to a reduction in the axial stress, leading to reduced resonance frequencies. The maximum frequency shift is observed when the laser beam is centered on a nanobeam, where heating is maximum. We perform Gaussian fits to the (thermally shifted) resonance frequency as a function of laser focus position for each beam. The blue lines in the subpanels of Figure 5.4c and d show the thermally tuned frequency shift $\Delta f = (f_{\mathrm{tuned}} - f_0)/f_0$. Frequency shifts as high as 5% (150 kHz) are observed.

To further investigate this effect, we calculate the relative frequency shift as a function of absorbed power using a simple thermal model [117–120]. We calculate the eigenfrequencies as a function of stress in the nitride layer of the beams:

$$f = \frac{1}{2\pi}\frac{\beta^2}{L^2}\sqrt{\frac{E_e I}{\rho_e w h} + \frac{12.30\sigma_e L^2}{\rho_e \beta^4}}, \tag{5.2}$$

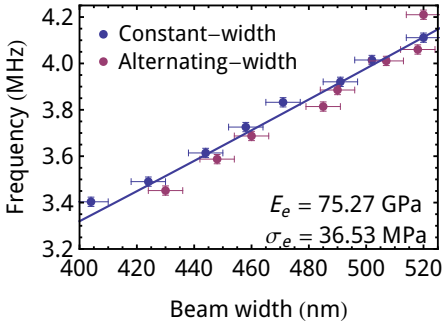


**Figure 5.5:** Non-thermally shifted eigenfrequencies for constant-width array (blue data points derived from Figure 5.4a,c) and alternate-width array (red dots, derived from Figure 5.4b,d) and model, fitting effective Young's modulus $E_e$ and in-plane stress $\sigma_e$.

using geometric averaging to calculate the effective stress $\sigma_e$, Young's modulus $E_e$ and density $\rho_e$ for the Au/$Si_3N_4$ bilayer beams. As we are measuring the fundamental mode, we use $\beta = 4.73004$ [69].

To fit the model to the data, we first extract the non-thermally shifted eigenfrequencies from the Gaussian fits in Figure 5.4(a,b), and plot these as a function of beam width in Figure 5.5. We then fit Equation (5.2) to the data using the effective Young's modulus $E_e$ and stress $\sigma_e$ as free parameters, using length and height as determined from SEM images, and using literature values for the mass densities of gold and silicon nitride. Figure 5.5 shows good agreement between model and data for an effective Young's modulus of $E_e = 75.2$ GPa, between the value of that for gold and silicon nitride. The fitted effective stress is $\sigma_e = 36.5$ MPa. Assuming the manufacturer's specification of $\sigma_e = 250$ MPa, this implies that there is a compressive stress of $\sigma_{Au} = -60$ MPa in the gold layer.

To verify the analytical bilayer eigenfrequency model, we also performed finite-element-method (FEM) simulations (COMSOL 4.3), with parameters identical to those quoted above. The eigenfrequencies calculated in the FEM simulation are shown together with the curves calculated using Equation (5.2) in Figure 5.6, showing excellent agreement between our analytical model and the FEM simulations. We note that when performing FEM simulations of beams with flexural stiffness, it is important to include enough (approximately 15) mesh points in the direction of the vibration. Otherwise, the flexural stiffness will be incorrectly modeled, leading to an underestimation of the eigenfrequencies for low stress values.

The beams are however not completely doubly clamped: they are connected through the supporting silicon nitride membrane. We therefore also performed a FEM simulation of the full geometry of an array of 8 beams of increasing width. Figure 5.7 shows the simulated mode profile at the eigenfrequency of the fourth beam. As can be seen, the third beam (which is narrower than the fourth beam) is moving in phase with the fourth beam, while the fifth beam (wider than the fourth beam)

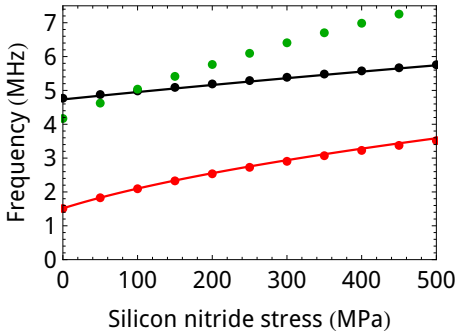


**Figure 5.6:** Resonance frequencies for a doubly-clamped gold on silicon nitride bilayer beam, showing the fundamental out-of-plane (red) and in-plane (blue) modes as a function of silicon nitride stress, calculated using Equation (5.2) (parameters given in main text). The dots are calculated eigenvalues extracted from a FEM simulation. The green dots are for the first excited out-of-plane mode.

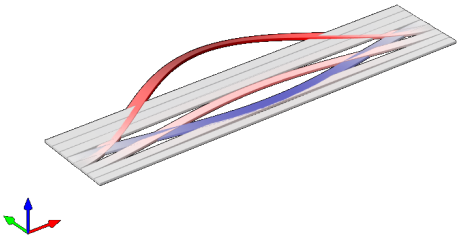

**Figure 5.7:** Simulated array of beams of increasing widths showing the shape of the fourth in-plane eigenmode, showing that the neighbouring beams are also in motion due to the coupling at the anchoring points of the beams. Displacements are greatly exaggerated for clarity.

is moving in antiphase. Figure 5.8a shows that the full-array-simulation leads to slightly different eigenfrequencies compared to simulating individual beams. We attribute this to the slightly different boundary conditions: in the full array simulation, as in the experiment, the boundary condition is not fully clamped: the mode can extend into the surrounding membrane, albeit with much larger stiffness and therefore smaller deflection.

Figure 5.8b shows the fundamental in-plane mode shape extracted from the simulation, compared to the analytical mode shape derived in Section 2.1 (blue line). We also plot the mode shape for a doubly fixed beam, with mode shape $X(x) = \sin(\pi x/L)$, which can be derived from the boundary conditions for a doubly fixed beam, $X(0) = X(L) = 0$, $X''(0) = X''(L) = 0$ [69] (see also Section 2.1). We see that the simulated mechanical mode profile has good agreement with the analytical doubly clamped mode profile: using single beam simulations is a good approxima-

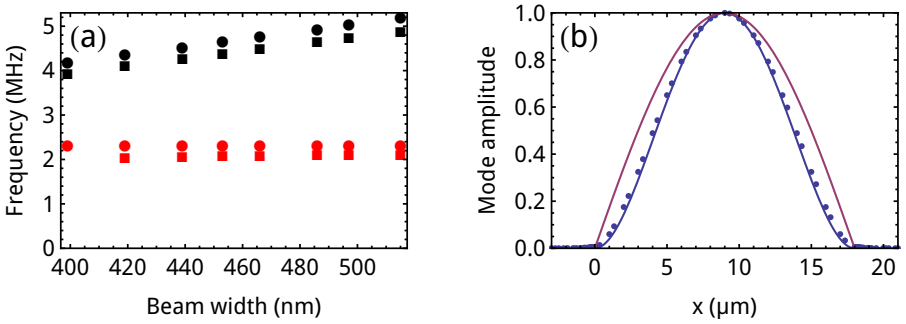


**Figure 5.8:** (a): Simulated resonance frequencies of an individual doubly-clamped bilayer beam (circles) and an array of beams (squares). Red: fundamental out-of-plane mode. Black: fundamental in-plane mode. (b): Calculated mode amplitude of the fundamental in-plane mode, as extracted from one of the beams in the full-array simulation (blue dots). Blue line: analytical mode amplitude for the fundamental doubly-clamped mode, calculated using Equation (2.21). Purple line: analytical mode shape for the fundamental mode of a doubly fixed beam, given by $X(x) = \sin(\pi x/L)$ [69].

tion for these arrays.

Next, we investigate the effect of heating of the nanobeams as they absorb light, changing the stress in the nanobeam through the thermal expansion coefficient:

$$\sigma = \sigma_i + \sigma_t = \sigma_i - \alpha_e E \Delta T, \tag{5.3}$$

where $\sigma_i$ is the original stress, $\sigma_t$ is the thermal stress, $\Delta T$ is the average temperature increase of the nanobeam, and $\alpha_e$ is the effective thermal expansion coefficient

$$\alpha_e = \frac{\alpha_{Si_3N_4} A_{Si_3N_4} + \alpha_{Au} A_{Au}}{A_{Si_3N_4} + A_{Au}}. \tag{5.4}$$

For this formulation for $\sigma$ to be valid, we assume the endpoints of the beam do not move. We can then calculate the relative frequency change due to heating, using Equation (5.2):

$$\delta f = \frac{\Delta f}{f} = \frac{f_t - f_i}{f_i} = \sqrt{1 + \left(\frac{f_0}{f_i}\right)^2 \frac{\sigma_t L^2}{3.4 E w^2}} - 1, \tag{5.5}$$

where $f_t$ is the thermally tuned frequency (Equation (5.2) with $\sigma$ from Equation (5.3)) and $f_i$ is the pre-stressed frequency without heating (Equation (5.2) with $\sigma = \sigma_i$) and $f_0$ is the eigenfrequency for a beam with no added stress ($\sigma = 0$).

We use a 1-dimensional heating model, in which the beam is heated by a power $P_{abs}$ applied evenly across the cross-section of the beam at $x_0$, while the ends of the beam are kept at ambient temperature ($T(0) = T(L) = 298$ K). In the stationary case,

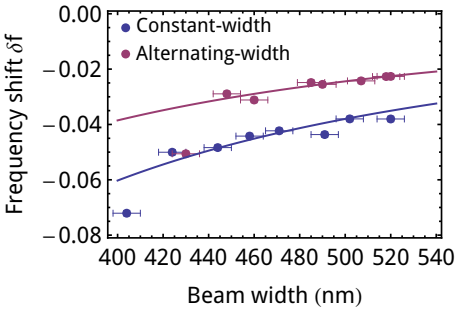


**Figure 5.9:** Measured thermally induced maximum frequency shifts from Figure 5.4 for constant-width (blue) and alternating-width (red) arrays as a function of beam width. The drawn lines are fits using Equation (5.8), with the fraction of absorbed power $\gamma$ as a free parameter.

the absorbed power equals the outgoing fluxes:

$$P_{\text{abs}} = A\kappa\left(T(x_0) - T(0)\right)\left(\frac{1}{x_0} + \frac{1}{L - x_0}\right). \tag{5.6}$$

with $\kappa$ the heat conductivity, so that

$$\Delta T = \frac{P_{\text{abs}} L}{8\kappa A}. \tag{5.7}$$

Inserting Equation (5.7) in Equation (5.3), we find from Equation (5.5):

$$\delta f = \sqrt{1 - \left(\frac{f_0}{f_i}\right)^2 \frac{\alpha_e L^3}{27.6\kappa_e w^3 h} P_{\text{abs}}} - 1 \tag{5.8}$$

Effective parameters for $\alpha$ and $\kappa$ are derived from the weighted averages (as in Equation (5.4)) using $\alpha_{Si_3N_4} = 1.23 \times 10^{-6}$ K$^{-1}$, $\alpha_{\text{Au}} = 14 \times 10^{-6}$ K$^{-1}$, $\kappa_{Si_3N_4} = 2.5$ W m$^{-1}$ K$^{-1}$, $\kappa_{\text{Au}} = 320$ W m$^{-1}$ K$^{-1}$.

Assuming the laser focus has a 2D Gaussian shape, the power density absorbed on one beam, with width $w$, can be expressed as a function of the incident power $P_{\text{in}}$ and a parameter $\gamma$ describing the fraction of incident power that is absorbed in the beam:

$$P_{\text{abs}} = \gamma P_{\text{in}} \text{Erf}\left(\frac{w\sqrt{\ln 2}}{\text{FWHM}}\right) \tag{5.9}$$

For example, for the constant-width array, a 500-nm-wide beam has 18% of the total optical power incident upon it, given the laser spot size. For the alternating-width array, the slightly larger focal width leads to a 500-nm-wide beam having 16% of the total power incident upon it. Figure 5.9 shows the measured maximum thermally induced frequency shift from Figure 5.4 as a function of beam width for

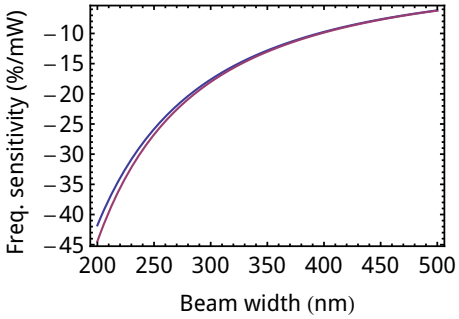


**Figure 5.10:** Calculated frequency shift in %/mW of absorbed power for a gold-coated silicon nitride beam, plotted as a function of beam width. The purple line is for the alternating-width array, the blue line for the constant-width array.

the constant-width and alternating-width arrays. The frequency shift is stronger for narrower beams, as these have a lower heat capacity. The drawn lines are fits of Equation (5.8) to the data, taking into account the width dependence of the incident power on the area of the beam (Equation (5.9)) and assuming a fixed fraction $\gamma$ of the power incident on the beam to be absorbed in the beam. We find the data can be fitted well with this model for both constant- and alternating-width arrays, and find that for a 500-nm-wide beam $P_{\mathrm{abs}} = 611$ μW for the constant-width array and $P_{\mathrm{abs}} = 396$ μW for the alternating-width array.

Using the thermal frequency shift model, we find that for both the constant-width and alternating-width arrays, the sensitivity of frequency to absorbed power is, for a 500-nm-wide beam, $\delta f / P_{\mathrm{abs}} = 6$ %/mW. This is shown in Figure 5.10. Because the heat capacity of a narrow beam scales with its width, the narrower beams are more sensitive to $P_{\mathrm{abs}}$.

## 5.4 Parametric oscillation of nanobeams

We have also studied the out-of-plane mechanical mode under high illumination power; Figure 5.11 shows the mechanical resonance spectrum for an array of 8 beams under 10 mW irradiation. The mechanical transduction amplitude exceeds 50 dB, and is much larger than the 7 dB observed in Figure 5.3. Also, the effective quality factor of the resonance increases to $Q_{\mathrm{m}} > 50.000$; this is a lower limit determined by thermal fluctuations that shift the resonance during the measurement averaging time. Figure 5.11 shows several harmonics at a frequency spacing exactly equal to the fundamental frequency of 2.21 MHz.

The appearance of these higher-order sidebands is intrinsic to the large modulation amplitude (up to 10% of the DC transmitted power). At these modulation amplitudes, power is transferred not only to the first sideband, but also to higher-

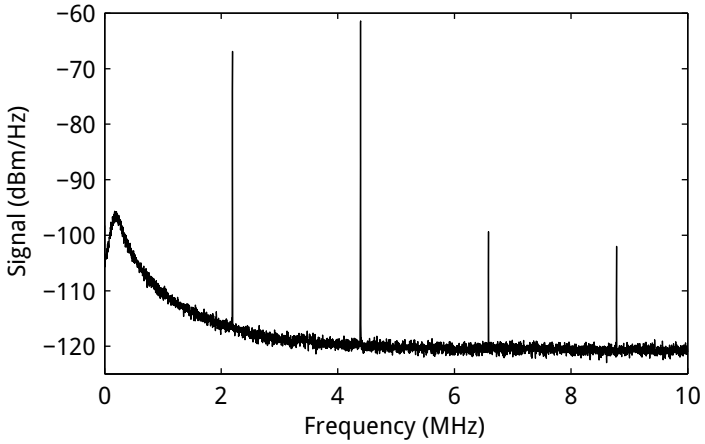


**Figure 5.11:** Mechanical response of a beam undergoing thermally induced parametric amplification, showing greatly increased response amplitude, high effective $Q$-factor and higher-order sidebands of the fundamental out-of-plane mode at 2.21 MHz.

order sidebands [22]. Spectra such as that shown in Figure 5.11 are observed for laser powers > 8 mW, with the exact threshold depending on the exact laser focusing condition.

We attribute this behaviour to parametric oscillations [12, 21] that occur due to a driving force that is bolometric in nature [123, 124]: for the out-of-plane mode, power absorbed in the beams causes an out-of-plane bending stress, due to the bilayer geometry of the beams and the differing thermal expansion coefficients $\alpha_{Si_3N_4}$ and $\alpha_{Au}$ of silicon nitride and gold, which, if this stress is modulated at twice the mechanical frequency, can lead to parametric oscillations. When the out-of-plane displacement of one of the beams increases, the incoupling into the plasmonic resonance is reduced, reducing the heating and allowing the beam to cool off, with a certain time delay controlled by the heat capacity, restoring the equilibrium position. Then, light can be coupled back into the cavity, once again increasing absorption, driving the beams to greater and greater displacement. This process is eventually limited by coupling of mechanical energy into the higher harmonics of the system.

## 5.5 Improving mechanical quality factor

The mechanical quality factors observed here and in Chapter 4 are all in the range $Q = 500 - 1000$, much lower than the typical values for high stress silicon nitride beams, which show quality factors up to $Q \sim 10^7$ [96, 125]. The quality factor is determined by viscous air drag, clamping losses and intrinsic material damping

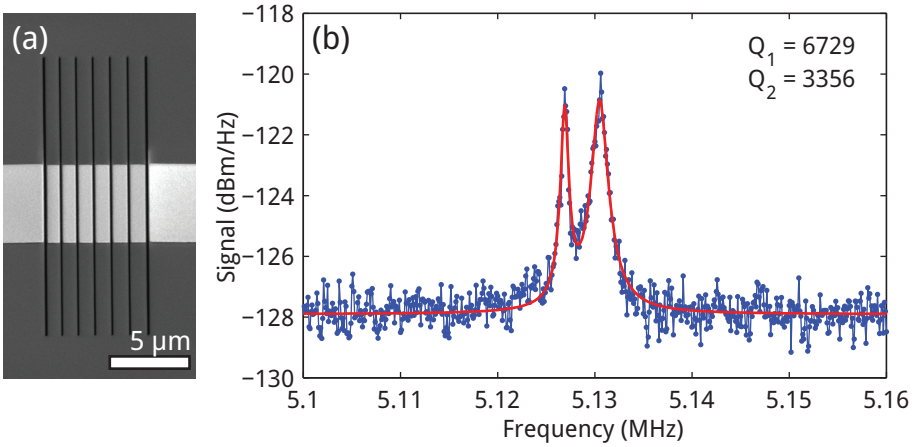


**Figure 5.12:** (a): SEM image of 5 µm wide gold bars on 20 µm long silicon nitride nanobeams. (b): Mechanical resonances in 2 µm wide gold bars on 20 µm long silicon nitride nanobeams, showing higher mechanical quality factor $Q_{\mathrm{m}}$. The red line shows a fit consisting of two Lorentzians and a constant offset through the data.

[107, 126, 127]. The viscous air drag is greatly reduced by measuring in vacuum, as is shown in Figure 4.7. The strain in the beam is the highest near the clamping points, leading to the highest losses due to intrinsic material damping, consisting of two-level systems [128, 129] and thermoelastic damping [125]. As the damping in gold is expected to be higher than that of silicon nitride, we fabricated a sample with no gold near the clamping points, using electron beam lithography, thermal evaporation and liftoff, following the method outlined in Section 3.3.2. Wide bars of gold (2–5 µm) were deposited on a silicon nitride membrane, which was then patterned into beams using focused ion beam milling. A SEM micrograph of a completed structure is shown in Figure 5.12a. Mechanical resonance spectra for these structures are shown in Figure 5.12b, and show quality factors up to $Q \approx 7000$. This indicates that intrinsic losses are a significant portion of the low $Q$ factors seen so far.

Other groups [37, 130, 131] have shown that the clamping losses can be reduced by engineering the surroundings of the beam to form a phononic crystal: the acoustical analog of a photonic crystal, which prevents the mechanical phonons from tunneling into the surroundings.

We expect that the quality factor is also limited by gallium implanted during the fabrication process. Using a dry-etch process with for instance $CF_4$ or $SF_6$ to release the beams could potentially increase the mechanical quality factor.

We also note that this reduced effective mass of the structure should increase the amplitude of the mechanical motion. Reducing the covering of the beams also

changes the transduction model: the gold covering the beams creates a darkfield geometry, suppressing background noise, as described in Section 2.7. Reducing the gold coverage will allow light that has not been modulated by the plasmonic cavity to reach the detector, increasing the noise imprecision. Finally, for much longer beams (length 1 cm), Schmid et al. [119] show that removing the gold near the beams' anchoring point can increase the thermal eigenfrequency tuning, by decreasing the thermal conductivity to the substrate, which is useful in the context of the thermal tuning shown in Section 5.3, as well as for using the devices as bolometric sensors.

## 5.6 Avoided crossings in arrays of beams

Multiple mechanical oscillators can not only be used for parallelization of measurements. If the mechanical modes are coupled, a range of different effects can be observed and exploited, for instance using localized modes [132] to improve sensitivity [133], or using coupled resonances to create mechanical RF filters [134, 135], to enable single-input single-output mass sensing [136] or to observe synchronization [137].

If two resonators are coupled, and then are tuned to make their eigenfrequencies match, their eigenfrequencies as a function of coupling will show an avoided crossing, as shown earlier for nanomechanical systems [138, 139]. Figure 5.7 shows a FEM simulation of the in-plane eigenmode of the fourth beam, showing that the neighbouring beams also contribute to the eigenmode. To study the coupling between the beams, we fabricated an array of eight beams with beam widths leading to in-plane eigenfrequencies such that they could be thermally tuned to match. This was achieved by fabricating an array of eight beams with widths of 425, 450, 459, 480, 500, 525, 545 and 570 nm, where the third and fourth beams have nearly identical widths. The gap widths were fabricated to be alternating between 20 and 40 nm.

Figure 5.13 shows the measured mechanical transduction as a function of frequency and of the position of the focused laser beam in the array. The thermal tuning behaviour observed in Figure 5.4 is clearly observed for 4 beams. Two avoided crossings are observed, indicated by the dashed outlines.

We also observe a non-avoided crossing, suggesting these mechanical modes as being related to non-adjacent beams. For non-adjacent beams, we expect very low mechanical coupling between these beams, and therefore do not expect to see a splitting in the crossing.

## 5.7 Conclusion

We demonstrate parallel transduction of the thermally driven mechanical motion of an array of nanobeams using a simple free-space technique. The motion of each beam is transduced by the adjacent plasmonic slits. When these are identical, the

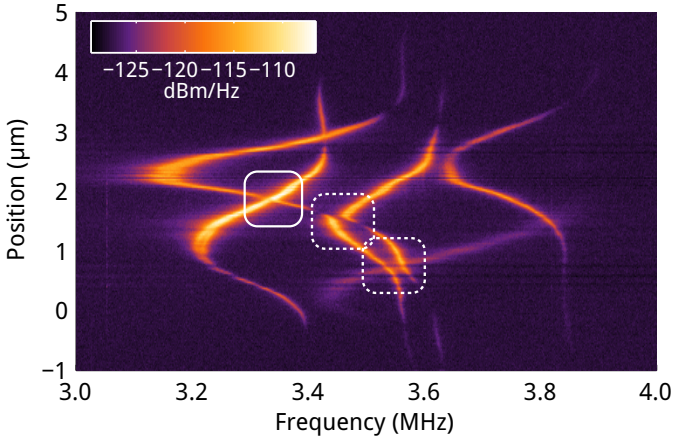


**Figure 5.13:** Mechanical transduction spectrum of an array of 8 microbeams, engineered to show avoided crossings in the thermally tuned eigenfrequencies of the microbeams. The widths of the beams was chosen such that one pair of neighbouring beams would have similar eigenfrequencies. The dashed outlines indicate avoided crossings. The solid outline indicates a non-avoided crossing.

transduction of in-plane motion can cancel, due to antisymmetric transduction by the slits. By tuning the gap width, the plasmonic resonances are tuned, allowing simultaneous parallel transduction of the mechanical modes of all beams.

The thermal tuning due to optical power absorption leads to resonance frequency shifts as large as 6%/mW of power absorbed in the beam. At powers above 8 mW parametric oscillations are observed due to a bolometric driving force. We find that neighbouring beams are mechanically coupled through the membrane in which they are suspended. When thermally tuning such an array to make the eigenfrequencies of two neighbouring beams match, the coupling between these beams creates an avoided crossing in the transduced mechanical modes of these two beams. The photothermoelastic effect observed in this work could therefore find application in tuning and actuating micro- and nanomechanical resonators. Creating beams that are free of gold near the clamping points can greatly increase the mechanical quality factor and reduces the total mass.

The principle of parallel plasmonic mechanical transduction could be used in a variety of sensor array applications, due to its simple free-space readout and scalability to include many more resonators than shown here.

# 6

# Plasmonic dimer antenna nano-optomechanical transducers

Dipole–dipole-coupled plasmonic dimer antennas, with nanoscale optical confinement in all 3 dimensions, are among the smallest conceivable optical resonators. Such a small optical system can naturally be interfaced with nanoscale mechanical beams. We use beams with a cross section of $100 \times 120$ nm and a length of 10.5 μm. Structures are fabricated with two beams, placing each of the dimer antenna elements on an individual nanobeam. Using small nanomechanical resonators is favorable for sensing: the reduction in effective mass increases the sensitivity for force and mass. We note that for the system studied in this chapter, the optical mode is smaller than the mechanical mode. This implies that the plasmonic antenna could be used to transduce the motion of even smaller mechanical systems than studied here.

The antennas are used to transduce thermally driven mechanical motion of the strings, measuring with a displacement sensitivity of 800 fm/$\sqrt{\text{Hz}}$ . This apporaches the thermal limit of the sensor, which has a single-sided force sensitivity of 420 aN/$\sqrt{\text{Hz}}$ and a mass sensitivity of 10 fg in a 1 Hz bandwidth on resonance at room temperature. We analyze the sensitivity of this system, study a crossed-polarizer technique to enhance the sensitivity, and investigate the different contributions to the measurement imprecision.

Finally, we discuss the possibility of further enhancing the sensitivity in future experiments, using coupled dipolar–quadrupolar plasmonic resonators. By combining the narrow linewidth of the radiatively limited quadrupolar mode with the strong plasmonic optomechanical frequency shift expected for dipole–dipole coupling, improved sensitivity is predicted.

## 6.1 Methods

The dipole–dipole coupled antennas operate around 1550 nm, utilizing the strong near field enhancement in the gap between the dimer elements for strong sensitivity to changes in the width of this gap. Gold antennas (total length 485 nm) are integrated with freestanding silicon nitride beams ($m_{\mathrm{eff}}$ = 160 fg, $\Omega_{\mathrm{m}} \approx 9$ MHz). The mechanical transduction is based on the near-field coupling between the antenna's two elements, where the two antenna elements are dipole scatterers. Due to dipole–dipole coupling, the modes of the antenna elements hybridize, forming a bright mode, with in-phase dipole moments and a dark mode, where the two dipole moments are driven in antiphase [61]. In this experiment, we observe the dipole–dipole coupled bright mode. When the in-plane motion of the nanobeams changes the distance between the antenna elements, the resonance frequency is changed, as described in detail in Section 2.3.

Figure 6.1a shows a schematic of the antenna-on-beam geometry, fabricated using a combination of electron-beam lithography and focused ion beam milling, as described in Section 3.3.2. SEM images are shown in Figure 6.1b and c. We can realize double-beam structures with lengths up to 15 µm and nanobeam separation of 30 nm. Separations down to 20 nm are achievable but with very low fabrication yield.

## 6.2 Optical design

Before fabricating antennas and milling beams around them, we first measure the resonance properties of arrays of dimer antennas using white light scattering. This is done to determine the scattering properties of the antennas, which aids in fabricating antennas with the correct dimensions on the nanomechanical beams. We perform Fourier-transform-infrared-spectroscopy (FTIR) transmission measurements on arrays of antennas, as measuring the transmission scattering spectrum from a single antenna in the infrared is experimentally challenging. Our FTIR microscope has a spot size with a diameter of approximately 70 µm with a numerical aperture NA = 0.39. To match this, we fabricate 70 µm × 70 µm fields of antennas with a pitch of 1 µm on a 100-nm-thick silicon nitride membrane. The antenna lengths range from 100 to 250 nm (length of one of the elements), with some fields of antennas having touching elements and others with element separations of 10 and 20 nm, as measured using an SEM. The results for arrays with antennas of different lengths, with element spacing of 20 nm, are shown in Figure 6.2a. We observe two resonances: the localized surface plasmon resonance (LSPR) around 1.4–1.5 µm, and a high-$Q$ surface lattice resonance [140, 141] at 1.25 µm, where the different antennas are coupled through a transverse-electric mode propagating through the 100-nm-thick silicon nitride membrane [142]. The LSPR resonance exhibits a clear red shift in extinction for increasing antenna element length, as expected. The laser wavelength in subsequent experiments is

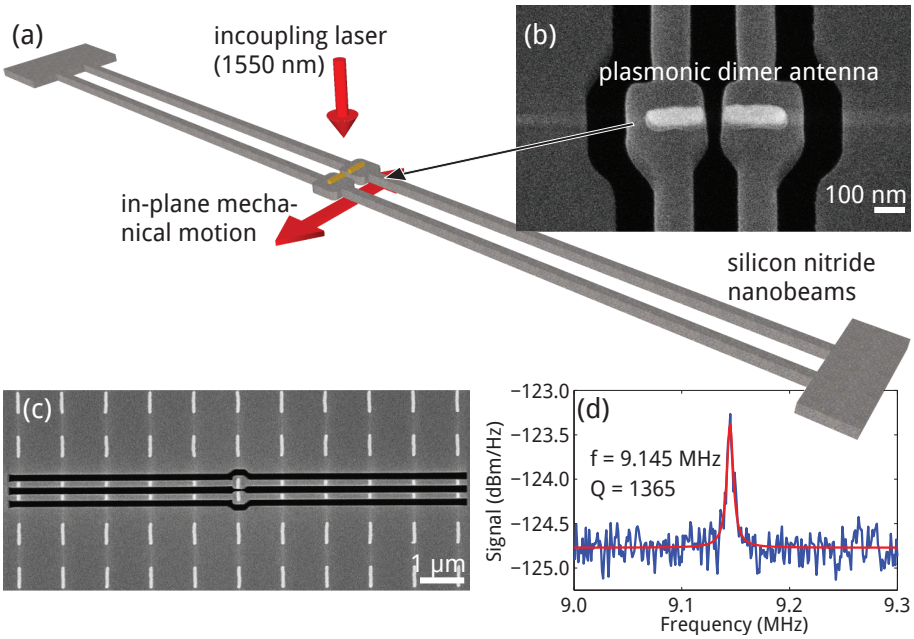


**Figure 6.1:** (a): Schematic depiction of the experimental geometry. (b): SEM image of the two elements (225 nm × 50 nm × 40 nm) of a dipole-coupled gold plasmonic dimer antenna, placed on individual silicon nitride nanobeams (10.5 µm × 120 nm × 100 nm), with a 30 nm gap between the two antenna elements. The beams' in-plane mechanical motion leads to modulation of the 1550 nm laser light scattered by the dimer antenna. The antennas are fabricated as one gold bar using electron-beam lithography, thermal evaporation of gold and liftoff, after which the beams and antenna are released using a single pass of focused-ion-beam milling. Scale bar: 100 nm. (c): SEM micrograph of a double beam structure with antenna. Scale bar: 1 µm. (d): Optically transduced thermal vibration spectrum of one of the nanobeams.

indicated with the dashed line. Based on this measurement we chose to use the 225 and 250 long antennas to create freestanding dimer antennas, since for these lengths, the laser wavelength is on the slope of the resonance, leading to the largest change in scattered power if the inter-element spacing is changed.

As the FTIR measurements are performed with unpolarized light, and the scattering from the antennas is highly polarization dependent, it is expected that the extinction for light polarized along the dimer axis is a factor 2 larger than shown in this measurement. The in- and outcoupling objective in the vacuum microscope (Figure 6.3a) both have NA = 0.75, while the FTIR measurement uses a lower numerical aperture (NA = 0.39). As we have seen in Section 2.3.5, the measured transduction of motion is sensitive to the NA used. Also, the antennas on beams

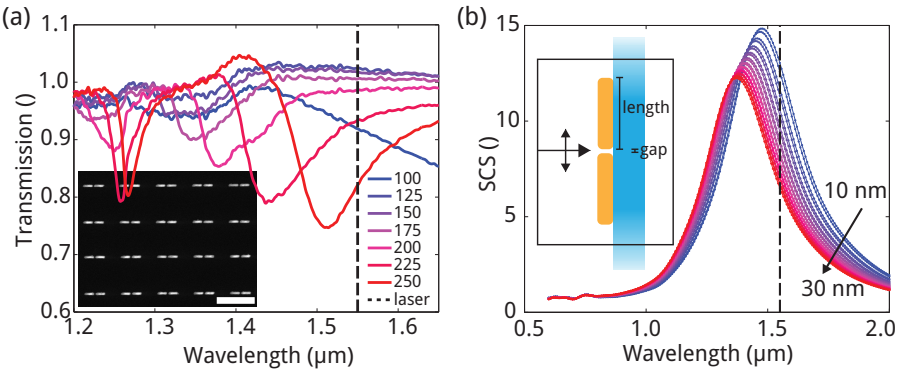


**Figure 6.2:** Optical characterization. (a): FTIR measurement of the transmission through $70 \times 70$ μm$^2$ fields of antennas of different lengths, all with gap width of ~ 20 nm. Lengths quoted in the legend are the lengths of one of the two elements. The laser wavelength of 1550 nm is indicated by the dashed black line. Inset: SEM micrograph of a portion of a field of dimer antennas, length 250 nm, with field pitch 1 μm. Scale bar: 1 μm. (b): Finite-difference-time-domain simulation of the scattering spectrum of a dimer antenna with elements of 225 nm long for different gap between the two elements, showing a change in center frequency $\omega_0$ and in total scattering as a function of gap size, with scattering cross section increasing and center wavelength red-shifting for decreasing gap width. The scattering cross section is normalized to the geometrical cross section of one antenna element ($225 \times 50$ nm$^2$). Arrow indicates varying gap width. Inset: schematic of the simulation volume, showing two gold particles and the silicon nitride substrate, which extends through the simulation boundaries. Arrows indicate the propagation direction and polarization of the incident light.

have a different dielectric surrounding, consisting of silicon nitride beams and vacuum, rather than a planar silicon nitride membrane. Therefore, the scattering from antennas as measured in the FTIR microscope can be different from that measured in the vacuum microscope.

Next, we performed finite-difference-time-domain (FDTD) simulations to verify the FTIR results, shown in Figure 6.2b. The inset in this figure schematically shows the total-field/scattered-field simulation used. The simulation shown is for a single particle, surrounded by perfectly matched layers. The localized surface plasmon resonance around 1.4 μm observed in the FTIR measurements for 225 nm particle length is clearly reproduced in these simulations.

The extinction dip at 1.25 μm is not observed in this single-particle simulation. When the simulation boundary conditions are set to be periodic, with a lattice period of 1 μm in both $x$ and $y$ directions, closely reproducing the experimental conditions for the FTIR measurement shown in Figure 6.2a, this dip is reproduced

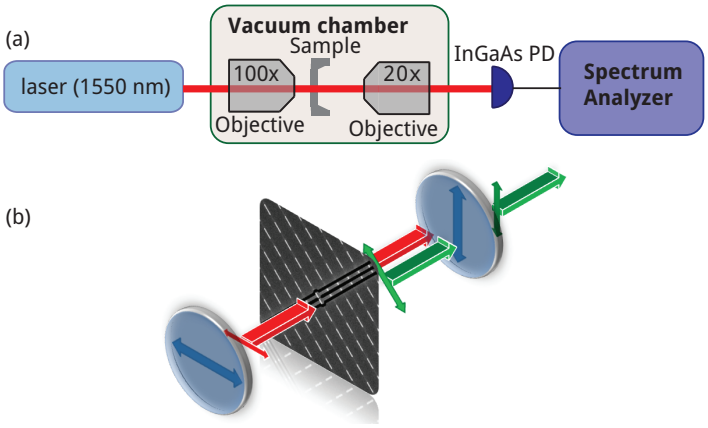


**Figure 6.3:** Measuring mechanical transduction. (a): Laser light from an erbium-doped fiber laser operating at 1550 nm is aligned onto the sample through the incoupling objective. The sample and in- and outcoupling objectives are placed on motor-driven stages in a custom built vacuum chamber evacuated to $10^{-3}$ mbar using a turbomolecular pump. The sample is mounted on a 3-axis feedback piezo stage to control the sample position in the laser focus. A second microscope is used to align the outcoupling objective. The transmitted light is then sent to an amplified photodiode. The AC output is monitored on a spectrum analyzer, and the DC output is monitored on an analog-to-digital converter. (b): Crossed polarizers are used to reduce the signal background. Light is sent in with horizontal polarization, with the sample mounted at 45°. A vertical polarizer is used to block non-scattered light and transmits 1/2 of the scattered light.

in the simulations, showing that this is a lattice-mediated resonance.

The simulations were also used to estimate the optomechanical frequency shift $G \equiv \frac{\partial \omega_c}{\partial x}$ and the scattering properties of individual antennas. For the design separation of 15 nm, we extracted $G \approx 2\pi \times 1$ THz/nm from the simulation, defining $x$ as the spacing between the antenna elements. However, the antennas as fabricated have a separation of 35 nm, leading to $G = 2\pi \times 0.45$ THz/nm. This leads to a predicted relative change of the scattering cross section of 0.01/nm in the antennas as fabricated. We choose the length for antennas on beams such that the laser probes the red side of their resonance, as this side has stronger transduction, as can be seen in Figure 6.2b. This is due to the radiation damping being lower for lower frequencies.

## 6.3 Mechanical transduction

The nanobeams exhibit both in-plane and out-of-plane mechanical modes, with resonant frequencies between 8 and 10 MHz, as predicted from FEM simulations.

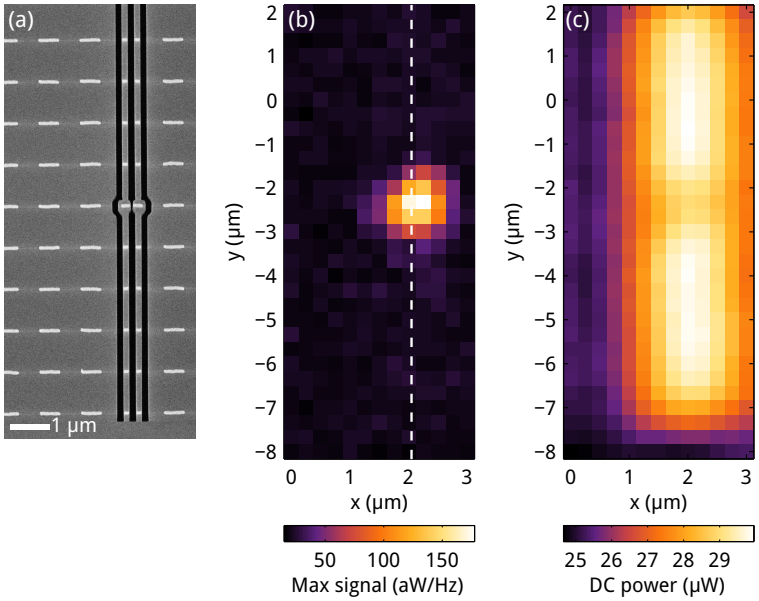


**Figure 6.4:** Raster scanning. (a): shows an SEM micrograph of the nanobeam with antennas, at a scale equal to (b) and (c), scale bar length: 1 µm. (b) and (c): Scanning the sample through the focus. (b) shows the signal power spectral density at the mechanical resonance frequency, with the noise background subtracted, while (c) shows the DC component of the transmitted power.

In this experiment, we are most sensitive to the in-plane motion, where the gap between the antenna elements changes with the vibration of the beams.

The mechanical transduction is measured by raster scanning the structures through a transmission microscope (Figure 6.3a), and recording intensity modulations in the transmitted light on an electronic spectrum analyzer (ESA). A 1.55 µm CW laser was used, with a spot size of about 1.8 µm FWHM on the sample (determined from Figure 6.4c). The experimental setup is discussed in detail in Section 3.1. Figure 6.1d shows a typical frequency spectrum obtained on the ESA, where the peak is the signal due to thermally driven mechanical motion of the beams, and the background is caused by various noise sources in the experiment. The transmitted signal, consisting of the light scattered by a single dimer antenna, is weak. We therefore use crossed polarizers (Figure 6.3b) to enhance the signal relative to the background noise sources in the experiment. Figure 6.4a shows an SEM image of the two double beam structures measured in Figures 6.4b and c. Figure 6.4b shows the highest value of the measured signal power spectral density for each pixel. The noise contributions are found by fitting a second-order polynomial to the total scan (2 MHz bandwidth). This is subtracted

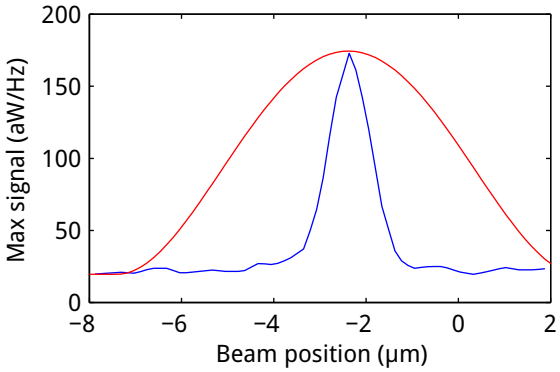


**Figure 6.5:** Signal power density (blue line) measured along the beam for the data shown in Figure 6.4b (data extracted on white dashed line as indicated in Figure 6.4b). The calculated double beam mechanical mode profile (Equation (2.8), plotted in red) is overlaid with the data.

from the measured peak value. The relative magnitude of signal and noise will be described later in this chapter. Figure 6.4c shows the DC optical power measured in the same raster scan. We see that due to the low albedo of the antenna, a reduction in scattering is observed at the antenna position, relative to the scattering from the beams.

### 6.3.1 Comparing signal profile to mechanical mode profile

If the mechanical transduction is due to scattering by the plasmonic antenna, we expect the signal in the raster scan (Figure 6.4b) to be strongly peaked around the antenna position in the center of the beam. If the transduction were not due to scattering from the antenna but some form of scattering or extinction from the whole beam, we would expect the signal strength to be proportional to the mechanical mode profile. To study this, we extract the signal strength along the beams from the raster scan in Figure 6.4b, and plot this in Figure 6.5. The red curve shows the mechanical mode profile, as calculated in Section 2.1. The center position of the mechanical mode profile is obtained from a least-squares fit to the measured mechanical transduction signal. The width of the mode profile is equal to the length of the beams (10.5 μm), and the amplitude and offset are determined by the minimum and maximum values of the plotted transduction signal. We see that the mechanical mode amplitude is more strongly peaked in the center of the beams than the mechanical mode. Rather, the width of the signal peak is comparable to the 1.8-μm spot size extracted from Figure 6.4c, indicating that the signal origin is from the antenna location at the center of the nanomechanical beams.

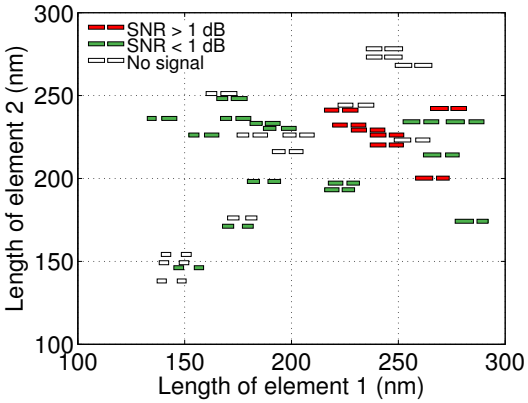


**Figure 6.6:** Distribution of antenna element lengths in this study. The color indicates the signal intensity measured on each antenna. The symbols are drawn to scale, with lengths & gaps matching sizes determined from SEM measurements.

### 6.3.2 Antenna length

To determine the resonance properties of the dimer antenna, we performed motion transduction measurements on antennas on beams with antenna elements and gaps of different sizes, as shown in Figure 6.6. In this figure the measured antennas are plotted as a function of the lengths of the elements. The antenna elements' lengths and the gap between them is plotted to scale in the symbols plotted in this graph. The transduced signal strength is indicated by the color: white antennas showed no transduction, green antennas show a weak signal (including noise) with SNR < 1 dB, and the red antennas had the highest SNR, with SNR > 1 dB. We find that for a fairly large range of antenna lengths there is some transduction. However, the antennas with the highest SNR in their transduction are clustered around $L_1 = 240$ nm, $L_2 = 240$ nm. This matches well with the antenna array transmission measured in Figure 6.2b, where the arrays with antenna lengths of 225 nm and 250 nm have their resonance such that the laser at 1550 nm is on the steep part of the red side of the resonance.

### 6.3.3 Noise sources in transduction

Figure 6.7 shows a signal trace for one of the antenna geometries, expressed in displacement spectral density (blue dots), with the various signal and noise contributions indicated. The vertical axis is calibrated using the spectral displacement density for thermal fluctuations:

$$S_{xx}^{th}(\Omega) = \frac{1}{m_{eff}} \frac{2\Gamma_m}{(\Omega^2 - \Omega_m^2)^2 + \Gamma_m^2 \Omega^2} k_B T. \tag{6.1}$$

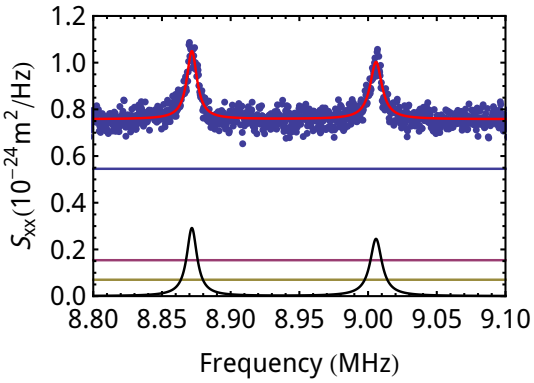


**Figure 6.7:** Measured mechanical displacement spectral density $S_{xx}(\Omega)$, detecting a total power of 22 μW. Blue dots: measured data points. Red line: total calculated signal, consisting of four separate contributions: displacement density (black); electrical noise (blue); classical noise (gold:); and shot noise (dark red). The determination of the relative magnitude of the noise contributions is described in Section 6.3.4.

The effective mass $m_{\mathrm{eff}} = 160$ fg is determined from the structural dimensions. The mechanical resonance frequency $\Omega_0$ and damping rate $\Gamma_m = \Omega_m/Q$ were extracted from the Lorentzian fit to the measurement. The spectrum shows two mechanical resonances. For the double-beam geometry which we study here, the two beams could couple through their clamping points. This leads to two modes: one with the beams moving in phase with each other and one with the beams moving out of phase. The former would have no transduction: the in-phase motion of the beams would not modulate the dimer antenna spacing.

The fact that we observe two resonances and that the mechanical transduction has almost the same strength for these two resonances implies that the two modes we observe are both confined to individual beams, with low coupling strength, and with frequency differences due to slight differences in fabricated width. As such, we can assume that the effective mass in Equation (6.1) is that of one moving beam. The $G$ extracted from simulations earlier is the same for one beam or two coupled beams, due to the definition of $x$ as the gap between the two antenna elements. From the Lorentzian fit we can find a total measurement imprecision $S_{xx}^{\mathrm{imp}} \approx 8 \times 10^{-25}\,\mathrm{m}^2/\mathrm{Hz}$.

The displacement spectral density of the beam modulates the power scattered and absorbed by the antenna, leading to a power spectral density $S_{PP}^{x}(\Omega)$.

This signal is superimposed on the signal due to three noise sources: shot noise and classical noise from the laser and electronic noise from the photodiode/amplifier combination. This offset in Figure 6.7 is due to these three noise sources and determines the measurement imprecision. In Section 6.3.4, we will show how we determined the relative amplitudes of the noise sources.

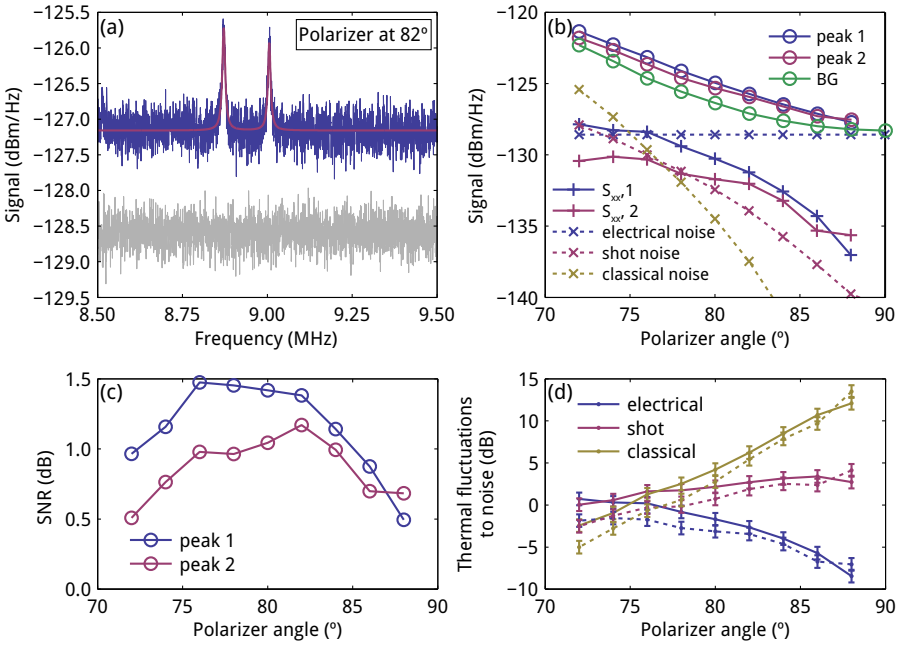


**Figure 6.8:** Mechanical transduction and noise versus polarization. (a): Mechanical trace with the polarizer at an angle $\zeta_{\text{out}} - \zeta_{\text{in}} = 82°$. The two mechanical peaks are the slightly non-degenerate eigenfrequencies of the two beams in the system. The gray trace shows the electrical background noise. (b): Various components of the signal: peak 1 (8.87 MHz) and 2 (9.02 MHz) are the amplitudes of Lorentzian fits to the two mechanical resonances visible in (a). The green line is the total background level of the signal, taken by averaging the power in the trace far from the mechanical resonances. This background level is decomposed into three sources (dashed lines): shot noise (purple), classical laser noise (gold) and electrical noise (blue). (c): The signal-to-noise ratio, comparing the two peaks to the total noise level. (d): The signal-to-noise ratios, comparing the signal to the different noise components (peak 1: solid lines, peak 2: dashed lines). We note that only the shot noise is fundamental; the other two noise sources could be reduced by changing experimental parameters.

### 6.3.4 Crossed-polarizer sensitivity

The scattering signal from the antennas is superimposed on a high background, as can be seen in Figure 6.4c which shows the DC intensity measured at the detector: the scattering from the antenna is not seperately visible due to strong scattering from the edges of the beams, instead appearing as a reduction in transmitted power. The antenna scattering could be low due to damage to the antennas

during the FIB milling process. An alternate explanation is that the antenna does scatter light, but not into the collection NA. This could for instance be due to the the complex dielectric environment created by the nanomechanical beams. To suppress (non-modulated) directly transmitted light and improve the signal-to-noise ratio, all measurements were performed with the structures placed between crossed polarizers, as discussed in Section 2.5. This occurs at the cost of a 3/4 reduction in scattered power: the 45° angle between input light and scatterer leads to a factor 2 reduction in scattered power. The 45° angle between the scattered light and detection polarizer leads to another factor 2 loss, this time in the collection efficiency.

Mechanical transduction spectra shown in Figure 6.8a were then measured for a large range of output polarizer angles, keeping the input polarization fixed. For every angle, a Lorentzian fit was performed to that data (see Figure 6.8a) and the signal to background ratio was determined.

Figure 6.8b shows the amplitudes for the two resonances as a function of polarizer angle (red and blue circles, joined by solid lines). The polarizer angle plotted in this figure is the angle between output- and input polarization $\zeta = \zeta_{\text{out}} - \zeta_{\text{in}}$. This angle is well calibrated. The angle $\zeta_{\text{in}}$ between antenna and input light is harder to determine, and will be extracted from the data. The background offset included in the Lorentzian fit is the total noise power detected. This noise power is plotted as the green circles in Figure 6.8b.

Figure 6.8c shows the signal-to-noise ratio as a function of the polarization angle. We find that the highest signal-to-noise, or lowest imprecision, is obtained not at $-\zeta_{\text{in}} = \zeta_{\text{out}} = 45°$, but with the output polarizer rotated to $\zeta_{\text{out}} \approx 35°$ (80° in the plot).

In this section, we will use the noise imprecision analysis developed in Chapter 2 to model this optimum polarizer angle. We start by rewriting Equation (2.105) as

$$S_{\text{xx}}^{\text{imp}} = S_{\text{PP}}^{\text{noise}}(\Omega)\frac{\mathcal{T}^2}{P_{\text{out}}^2}\frac{1}{(\partial\mathcal{T}/\partial x)^2}, \tag{6.2}$$

replacing $P_{\text{in}}$ with $P_{\text{out}}/\mathcal{T}$, with $\mathcal{T}$ the transmittance, to reflect the fact that we directly measure the output power. As discussed in Sections 2.4 and 2.5, we will assume we can neglect the phase noise contribution to the laser classical noise.

There are three main factors in this equation. The first factor is the noise power spectral density, composed of three three different noise contributions and their scaling with $P_{\text{out}}$:

$$S_{\text{PP}}^{\text{noise}}(\Omega) = 2\,\text{NEP}^2 + \hbar\omega P_{\text{out}} + \text{RIN}^2 P_{\text{out}}^2. \tag{6.3}$$

The second factor is $\mathcal{T}^2/P_{\text{out}}^2$. As in this experiment the scattered power is much smaller than the directly transmitted power, we will assume that the scattering and extinction contributions to $\mathcal{T}$ are negligible compared to the directly transmitted light (the light that has had no interaction with the scatterer). The third factor represents all mechanical transduction contributions: the properties of the scatterer and the optomechanical coupling rate $G$.

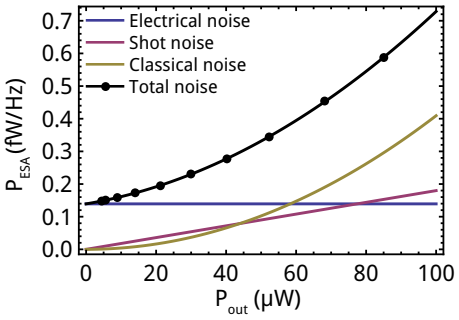


**Figure 6.9:** Noise contributions, in electrical power in 1 Hz bandwidth on the electronic spectrum analyzer, as a function of output power (dots), determined as the offset values of the Lorentzian fits as shown in Figure 6.7a and b. The three different noise sources as determined by fits of the first factor of Equation (6.2) are also plotted (colored lines).

As we also record the transmitted DC power, we can also plot the noise spectral density shown in Equation (6.3) as a function of $P_{\text{out}}$. These data are shown in Figure 6.9 (black dots). We can then calculate the magnitude of the different noise contributions by performing a second-order polynomial fit to the noise power as a function of $P_{\text{out}}$. The different noise contributions to the optical power spectral density $S_{\text{PP}}$ can then be determined from the fit results. The constant term (blue line in Figure 6.9) represents the laser-power independent electrical noise, $S_{\text{PP}}^{\text{el}} = 2\text{NEP}^2$, with NEP the noise-equivalent-power. The linear term (purple line) represents the shot noise, $S_{\text{PP}}^{\text{SN}} = \hbar\omega P_{\text{out}}$, and the quadratic term (gold line) represents the laser classical noise, $S_{\text{PP}}^{\text{class}} = \text{RIN}^2 P_{\text{out}}^2$, where RIN is the laser's relative intensity noise.

As we know both $S_{\text{PP}}^{\text{SN}}$, the absolute magnitude of the shot noise in the optical power spectral density, and the detected light power $P_{\text{out}}$, we can also calibrate the electronic transduction of the system, $P_{\text{ESA}} = g^2 S_{\text{PP}}$, where $P_{\text{ESA}}$ is the electronic power on the spectrum analyzer, finding that $g^2 = 1.444 \times 10^7$ [W] / [Hz]. This matches very well with the transduction calculated from the specifications for the photodiode, amplifier and spectrum analyzer, which predicts $g^2 = 1.413 \times 10^7$ [W] / [Hz].

We can now also plot the different noise terms as a function of polarizer angle. This is shown in Figure 6.8b (crosses with dashed lines), allowing comparison of the different noise sources to the mechanical signals ('+' signs with solid lines). Several interesting trends are observed. The electrical noise is independent of polarizer angle; the laser-related shot noise and classical noise contributions decrease with increasing angle due to the reduced light intensity on the detector.

In Figure 6.8d, we calculate the signal-to-noise ratio for the thermally-driven mechanical signals compared to the different noise sources for the two mechanical resonances. This shows that by using crossed polarizers, the effect of classical

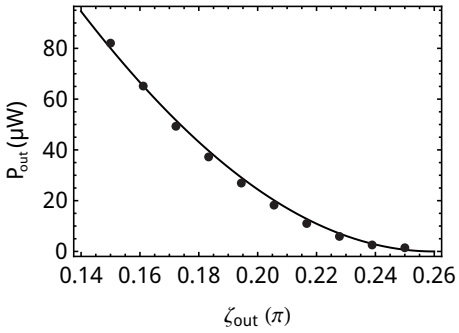


**Figure 6.10:** Detected power $P_{\text{out}}$ as a function of output polarizer angle $\zeta_{\text{out}}$ (blue dots). A fit is performed to find several parameters: $P_{\text{out}} = \mathscr{T} P_{\text{in}}$, assuming that the contribution of the scatterer can be neglected. We find $P_{\text{in}} = 700$ μW, $\zeta_{\text{in}} = -42.8°$. We use NA = 0.45, based on the measurement of the scattering width shown in Figure 6.4c.

noise is strongly suppressed, for increasing polarizer angle, due to the reduced laser intensity. However, the lower total transmittance $\mathscr{T}$ increases the relative contribution of the electrical noise. The optimum signal-to-noise is then observed for polarizer angles in the range 75–80°.

Next, we calculate the total transmittance $\mathscr{T}$. As discussed earlier, we will assume that due to the low scattering the transmittance is dominated by light that has not interacted with the scatterer. We plot the power detected $P_{\text{out}}$ as a function of polarizer angle $\zeta_{\text{out}}$ in Figure 6.10. From this fit, we obtain the angle for the input polarization as $\zeta_{\text{in}} = -42.8°$ and an input power $P_{\text{in}} \approx 700$ μW.

The conversion factor $g^2$ and the known thermal occupation as given in Equation (6.1) can be used to convert the noise power at each polarizer angle to an imprecision $S_{xx}^{\text{imp}}$ as shown in Equation (6.2). The various noise imprecision contributions, along with the total imprecision, are shown in Figure 6.11 as a function of output polarizer angle $\zeta_{\text{out}}$. We find reasonable agreement with the measured imprecisions by using a combination of values $G = 2\pi \times 0.38$ THz/nm, $\Delta = -0.78\gamma$, $Q_{\text{opt}} = 10$ and albedo $\mathscr{A} = 0.03$. These values are in line with several observations: the low albedo matches with the non-visibility of antenna scattering in Figure 6.4c, and the detuning of the laser relative to the antenna resonance being smaller than one linewidth agrees with the data shown in Figure 6.6.

The increasing imprecision with output angle $\zeta_{\text{out}}$ for the electrical noise and the decreasing imprecision for the classical noise are reproduced. However, the measured shot noise imprecision decreases with angle while the calculation predicts an increase. The origin of this discrepancy is unknown. The overall trend in the imprecision is represented by the model.

With the data currently available, and due to the unexplained low albedo, it is not possible to determine all the transduction parameters independently. Having

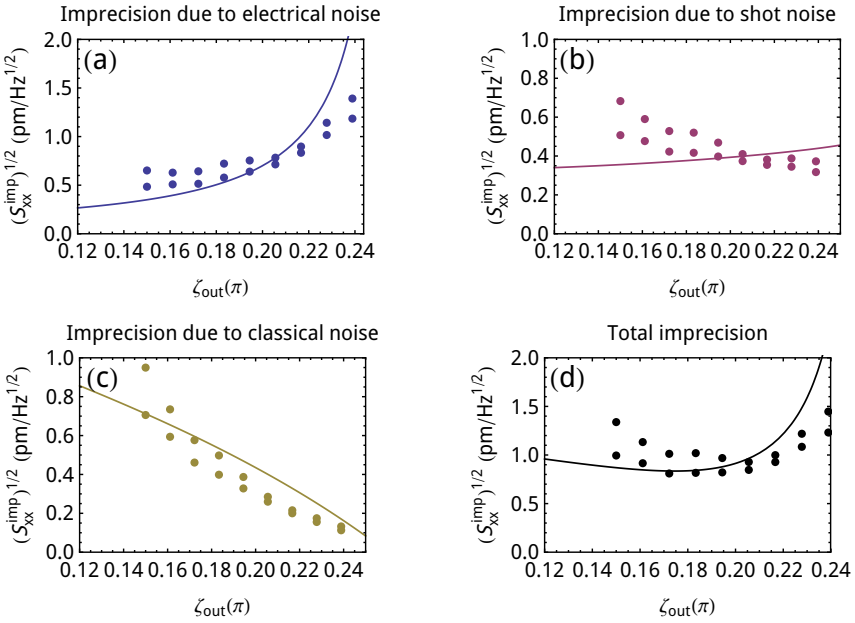


**Figure 6.11:** Imprecision due to electrical noise (a), shot noise (b) and classical noise (c), and total imprecision (d) as a function of output polarizer angle, derived from the analysis in Section 6.3.4. The lines are calculated using parameters: $G = 2\pi \times 0.38$ THz/nm, $Q_{opt} = 10$, detuning $\Delta/\gamma = -0.78$, and a very low albedo $\mathscr{A} = 0.03$.

a separate measurement of the scattering spectrum of a single dimer nanoantenna on beams would allow determination of $\Delta, Q_{opt}$ and $\mathscr{A}$, allowing determination of $G$ through the mechanical transduction measurements shown here. To improve the overall sensitivity, improving the albedo of the antenna would be the first major topic for future work on this experiment.

### 6.3.5 Vacuum optomechanical coupling rate $g_0$

So far in this thesis, we have used the optomechanical frequency shift per unit displacement

$$G \equiv \frac{\partial \omega}{\partial x} \tag{6.4}$$

as a key parameter to express the optomechanical coupling strength. Another quantity of interest is the frequency shift for a displacement equal to the zero-point displacement fluctuations of the mechanical oscillator:

$$g_0 \equiv G \cdot x_{zpf}, \tag{6.5}$$

known as the *vacuum optomechanical coupling rate* [143]. The oscillator's zero-point displacement fluctuations have an average amplitude

$$x_{\mathrm{zpf}} = \sqrt{\frac{\hbar}{2m_{\mathrm{eff}}\Omega_m}}. \tag{6.6}$$

In other words, $g_0$ expresses the coupling strength between one photon and one phonon. This definition for the coupling strength simplifies the comparison between different optomechanical experiments, as it eliminates some of the ambiguities in defining $G$, such as at which position on the oscillator to define the displacement $x$.

For the geometry here, we estimate a coupling rate

$$g_0 \approx 2\pi \times 75\,\mathrm{MHz}, \tag{6.7}$$

using $G = 2\pi \times 1$ THz/nm as extracted from the FDTD simulations shown in Figure 6.2a and an effective mass of 160 fg, based on the dimensions of the mechanical oscillator. We note that this result for $g_0$ is a very large number compared to current optomechanical experiments, exceeding the strongest reported coupling rates in photonic crystal cavities [35, 36] by more than an order of magnitude. In fact, in this case $g_0$ is even larger than the mechanical frequency $\Omega_{\mathrm{m}}$ by a factor 8. Of course, we do note that this strength is achieved in the presence of an optical loss rate many orders of magnitude larger than the mechanical frequency $\Omega_{\mathrm{m}}$.

## 6.4 Force & mass sensing

Mechanical oscillators can not only be used to detect motion, but also to detect for instance external forces or mass changes. In this section, we will calculate the sensitivity of the oscillators shown in this chapter for force and mass sensing, and demonstrate that the low effective mass makes these oscillators sensitive measurement devices.

### 6.4.1 Force sensing

One of the applications of (nano)mechanical resonators is as force sensors [9, 144–146]. Force couples to the spectral displacement density through the mechanical susceptibility, as shown in Section 2.2.1:

$$S_{\mathrm{FF}}(\Omega) = \frac{S_{\mathrm{xx}}(\Omega)}{\left|\chi_{\mathrm{xx}}(\Omega)\right|^2}. \tag{6.8}$$

In a way, by measuring thermal fluctuations, we are operating our device as a force sensor, measuring the thermal Langevin force. In Figure 6.12, we show (blue data points) the force sensitivity as a function of frequency for the system under

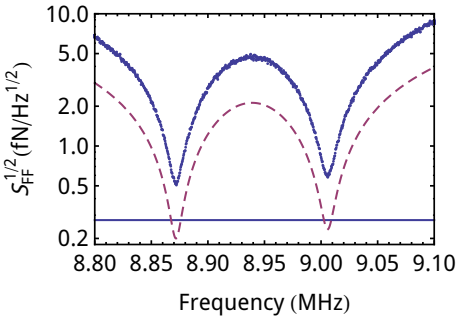


**Figure 6.12:** Force imprecision level. Data points: force imprecision obtained from data shown in Figure 6.7, converted to $S_{FF}^{imp}$ using Equation (6.8). Blue line: thermal Langevin force from Equation (6.10). Purple dashed line: shot noise force imprecision level $S_{FF}^{SN}$ (Equation (6.11)).

study in this chapter, obtaining a (single-sided) force imprecision on resonance $\sqrt{S_F^{imp}(\Omega_m)} = 930$ aN/$\sqrt{\text{Hz}}$.

This approaches the fundamental limit to force sensitivity given by the stochastic thermal Langevin force [146]:

$$S_{FF}^{th}(\Omega) = -2\frac{k_B T}{\Omega}\frac{1}{\text{Im}\chi_{xx}(\Omega)}, \tag{6.9}$$

which for high-$Q$ harmonic oscillators near resonance approximates to the single-sided force spectral density ($S_X = 2S_{XX}$)

$$S_F^{th}(\Omega) \approx 4 m_{eff} k_B T \Gamma_m. \tag{6.10}$$

For our resonator, $\left(S_F^{th}\right)^{1/2} = 420$ aN/$\sqrt{\text{Hz}}$ (blue line in Figure 6.12), implying that with 1 second of averaging, a force of 420 aN could be resolved, which is within an order of magnitude of the best room temperature system reported [126].

In this experiment, we are limited by the electrical and classical noise contributions, as discussed in Section 6.3.4, leading to the observed force sensitivity of 930 aN/$\sqrt{\text{Hz}}$. While these noise contributions can be reduced through technical means, the shot noise contribution is intrinsic to the light used in the measurement and can not be reduced by increasing the power. We therefore also plot the force imprecision due to shot noise:

$$S_{FF}^{SN} = \frac{S_{xx}^{SN,imp}}{\left|\chi_{xx}(\Omega)\right|^2}. \tag{6.11}$$

This is plotted in Figure 6.12 as the purple dashed line. Adding this imprecision to the thermal force limit in Equation (6.9) would give the force sensitivity for a

shot-noise-limited detection. Figure 6.12 shows that on resonance, the shot noise imprecision is lower than the thermal Langevin force imprecision: a shot-noise limited measurement would reach the thermal limit.

We have also calculated the force sensitivity for the high-albedo scatterer as discussed in Section 2.5 using the mechanical parameters of the nanobeams shown in this chapter. In this case, the force sensitivity is limited by thermal noise over a 5 MHz bandwidth around the mechanical resonance frequency $\Omega_\mathrm{m}$. This implies that the force sensitivity could be improved by using smaller beams with a lower thermal occupation.

### 6.4.2 Mass sensing

Another application of nanomechanical oscillators is mass sensing, as reviewed by Ekinci *et al.* in [1, 147]. By placing the oscillator in a flow of particles, molecules or atoms, some of these will accrete on the oscillator. This changes the mass of the oscillator, which changes its eigenfrequency. This frequency shift can then be measured by monitoring the amplitude of the oscillator, while it is driven on resonance. Very high sensitivities have been shown, with record sensitivities down to the zeptogram [97] and recently yoctogram [148] scale, with the latter experiment using carbon nanotubes as mechanical resonators at millikelvin temperatures.

Note that the position of accretion is important: depending on the mode shape, this can lead to an effective mass for the object to be weighed. In this paragraph, we will assume any mass changes are at the point of maximum mode displacement, leading to $m_\mathrm{eff,test} = m_\mathrm{phys,test}$: the effective mass of any accreting mass is equal to its physical mass.

The basic strategy for testing for mass is to drive the oscillator to improve the signal over the (thermally driven) noise level. One way to drive our plasmonic mechanical resonator would be to drive it using a (pump) laser beam modulated at the mechanical frequency, using thermal heating to cause a bending moment in the beam.

From Ekinci *et al.* [147], we have the following expression for the detectable change in mass $\delta M$:

$$\delta M \approx 2 m_\mathrm{eff} \sqrt{\frac{E_\mathrm{th}}{E_\mathrm{c}}} \sqrt{\frac{\Delta f}{Q \Omega_\mathrm{m}}}, \tag{6.12}$$

where the ratio of the drive energy to the thermal energy, $E_\mathrm{c}/E_\mathrm{th}$, is the effective dynamic range available. The drive energy can be expressed as $E_\mathrm{c} = m_\mathrm{eff}\Omega_\mathrm{m}^2 \langle x_\mathrm{c}^2 \rangle$, and the measurement bandwidth is $\Delta f$, which must be at least smaller than $\Gamma_\mathrm{m}$. We will assume the two beams have different frequencies, so we can restrict our analysis to one beam. There are two factors limiting the drive amplitude: the geometrical proximity of the neighbouring beam and the onset of nonlinearities in the mechanical restoring force at large deflections. As we assume that we can drive the two beams independently, we can drive the beam to an amplitude $x_\mathrm{c}$ equal to the gap between the two beams, so $\max(x_\mathrm{c}) = 30$ nm. To stay in the linear regime,

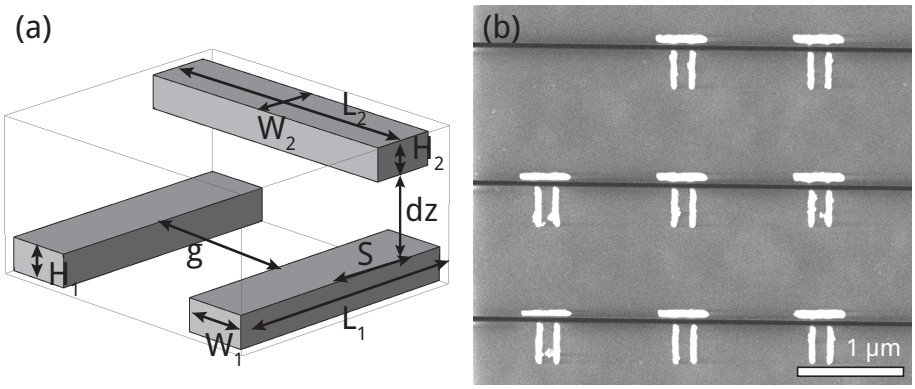


**Figure 6.13:** (a): Sketch of PIT geometry studied in this section, indicating relevant size parameters. (b): SEM image of PIT antennas fabricated on freestanding beams.

Ekinci *et al.* derive a limit $x_c < 0.53t$, where $t$ is the thickness of the beam in the direction of motion. This limit is based on a power expansion of the potential energy of the beam, where the contributions of order higher than quadratic (the Hooke's law contribution) are limited to be less than 10%. As our beams have an in-plane width of 120 nm, this condition is met. We can then determine a minimum detectable mass change of $\delta M = 10$ fg in a bandwidth of 1 Hz for our mechanical resonator at room temperature.

We note is that when driving the beam over this large displacement range, the optomechanical coupling rate $G$ will vary with position $x$, resulting in a different $G$ when driving the beam over a large amplitude than the static $G$.

The mass sensitivity can be improved by using smaller beams. These have lower effective mass and higher frequencies as $\delta M$ scales as $\sqrt{\frac{1}{Q\Omega_m^3}}$. As our plasmon transducer is still much smaller than the beams we currently study, using smaller beams is a feasible option for improving mass sensitivity.

## 6.5 Plasmonically induced transparency for transduction of motion

The transduction model developed in Chapter 2 and the experiments shown here are not limited to dipole–dipole coupled dimers: there are many other possible configurations of nanoscale scatters. These can show Fano interference between two modes, typically a high-$Q$ subradiant and a low-$Q$ superradiant mode [77, 149–156].

In this section, we will discuss a scatterer with near-field coupling between a dipolar and a quadrupolar scatterer, known as a 'dolmen' or '$\pi$' structure, which has

been shown to exhibit 'plasmonically induced transparency' (PIT) [150–152, 157, 158]. This effect bears resemblance to electromagnetically induced transparency [159], where in this case near-field coupling between the dipole and quadrupole modes takes the role of the strong coupling laser field in EIT, which couples two electronic levels. In the implementation we discuss, a nonradiative quadrupole, composed of two metal bars, is near-field coupled to a scattering dipole, composed of one bar. A transparency dip appears in the dipole's scattering due to interference between the incident light and light that scatters back from the quadrupole antenna. This geometry is sketched in Figure 6.13a.

Because the quadrupole is to first approximation nonradiative, it exhibits strongly reduced radiation damping compared to the dipole, and therefore has a narrower linewidth. Making the narrow linewidth of the quadrupole resonance visible using the high cross section of the dipole resonance could potentially offer benefits for transduction of motion.

We will study two motion transduction schemes using PIT: changing the coupling strength $\kappa$ between the dipole and quadrupole, which changes the depth of the PIT dip, and changing the detuning $\delta$ between the dipole and quadrupole resonance frequency, leading to a change of the frequency of the dip.

### 6.5.1 Changing coupling strength $\kappa = \bar{\kappa} + Fx$

Figure 6.13a shows a sketch of the plasmonic resonators we will use for calculations in this section and indicates all relevant size parameters. Figure 6.13b shows an SEM image of a PIT antenna we fabricated on freestanding beams.

The polarizability of the system can be expressed as [150, 160]

$$\alpha(\omega) = \frac{2\omega\Omega_{\mathrm{Q}} f}{\kappa^2 - 4\omega^2\Omega_{\mathrm{D}}\Omega_{\mathrm{Q}}}, \tag{6.13}$$

with $\kappa$ the dipole–quadrupole coupling strength, and where $\Omega_{\mathrm{D}}$ and $\Omega_{\mathrm{Q}}$ express the properties of the dipole and quadrupolar elements respectively:

$$\Omega_{\mathrm{D}} = \omega - \omega_0 + \mathrm{i}\gamma_{\mathrm{D}}/2 \tag{6.14}$$

$$\Omega_{\mathrm{Q}} = \omega - \omega_0 + \delta + \mathrm{i}\gamma_{\mathrm{Q}}/2, \tag{6.15}$$

including a possible detuning $\delta$ between the dipole and quadrupole resonance frequency. For $\kappa = 0$, Equation (6.13) reduces to the polarizability for a single dipole. The coupling strength can be tuned by changing $S$: the horizontal distance between the centers of the dipole and quadrupole. Due to symmetry, there is no coupling at $S = 0$, and we expect the strongest coupling when $S \approx L_1/2$, close to the geometry sketched in Figure 6.13a.

We modeled the PIT system using FDTD simulations, sweeping $S$, using parameters as in [67, 160], $L_1 = 315$ nm, $L_2 = 355$ nm, $H_1 = H_2 = 40$ nm, $W_1 = W_2 = 80$ nm, $d_z = 30$ nm and $g = 220$ nm. The resulting calculated scattering cross section $C_{\mathrm{ext}}$ is shown in Figure 6.14, for $S$ ranging from 0 to 130 nm in steps of 10 nm. We see that

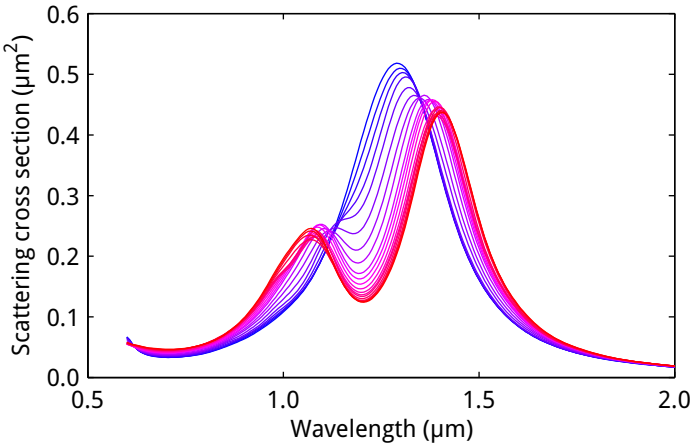


**Figure 6.14:** Finite-difference-time-domain simulations of a coupled dipole–quadrupole antenna PIT system, showing the calculated scattering cross section. For different curves, the offset between the dipole and quadrupole was changed: $S = 0$ for the blue line, $S \approx L_1/2 = 130$ nm for the red line. The transparency dip is detuned from the dipole resonance: $\delta \approx -20$ THz.

the coupling at small $S$ is indeed very small, increasing to create a 75% transparency window when $S$ approaches 120 nm.

Next, we performed fits of the PIT-polarizability to the simulated data, first fitting center frequency $\omega_0$, oscillator strength $f$ and intrinsic loss $\gamma_{i,\mathrm{D}}$ of the dipolar scatterer for the $S = 0$ simulation, using the radiation damping equation

$$\gamma_{\mathrm{D}} = \gamma_{i,\mathrm{D}} + \frac{f\omega^2}{6\pi\epsilon_0 c^3}, \tag{6.16}$$

shown earlier as Equation (2.61), to describe the damping for the dipolar scatterer. We find $f = 0.56$, $\omega_0 = 2\pi \times 228$ THz and $\gamma_i = 2\pi \times 8.5$ THz. Using these values, we then perform fits to the remaining simulations, to find $\gamma_{\mathrm{Q}} = 2\pi \times 18$ THz and $\delta = -2\pi \times 20$ THz.

We now determine the dependence of $\kappa$ on $x$, to model the motion transduction by changing the offset $S$ between the dipole and quadrupole. We express $\kappa(x)$ as a quadratic fit to the quadrupole offset $S$: $\kappa(x) = 2\pi(0.2432x - 6.72 \times 10^{-4}x^2)$, with $x$ in nm, with $\kappa$ in units of $2\pi$ THz/nm. We constrain the fit to have $\kappa(x = 0) = 0$: due to symmetry, the coupling at $S = 0$ must be $\kappa = 0$. Note that while $\kappa$ is expressed as a frequency, it actually changes the scattering amplitude and not the center frequency, as the coupling parameter $G$ does.

We can, using the same framework as in Chapter 2, find the $\mathrm{Im}(\alpha)$ and $|\alpha|^2$ terms, as well as their derivatives, after which we can express the imprecision levels for this plasmonic transducer. We will also define a 'good' PIT antenna, with $\gamma_i = 0$, $\gamma_{\mathrm{Q}} = 2\pi \times 5$ THz and $\delta = 0$.

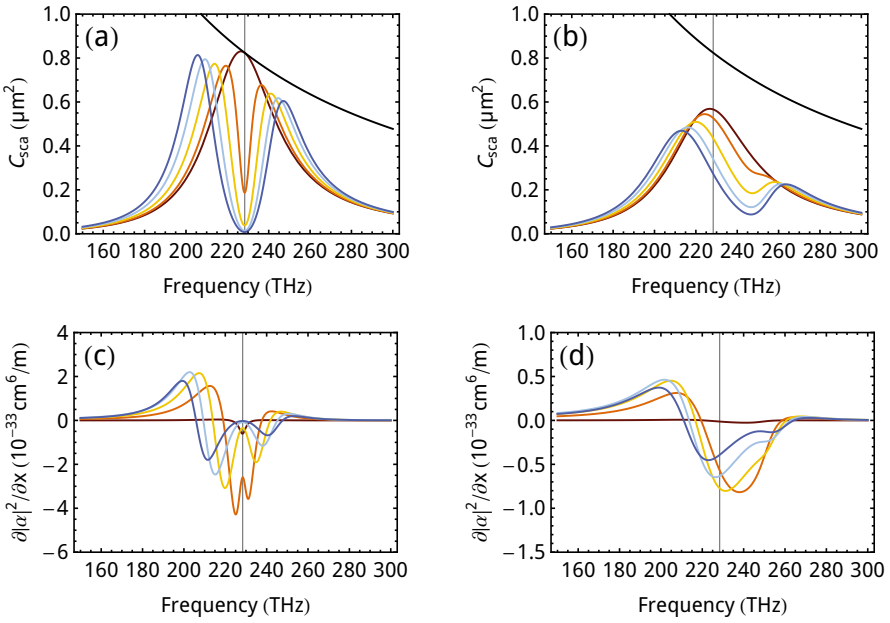


**Figure 6.15:** Scattering and change in scattering for PIT antennas. The left column is for a 'good' PIT scatterer, the right column for a 'bad' PIT scatterer (parameters in main text). Different color curves indicate changing offset $S$. Red line: $S = 0$, then in 30 nm steps to the blue line with $S = 120$ nm.

In Figure 6.15, the top two graphs plot the scattering cross section $C_{\text{sca}}$ for the 'good' and 'bad' PIT scatterer, and the bottom two graphs plot $\partial|\alpha|^2/\partial x$, the change in $|\alpha|^2$, which is proportional to $C_{\text{sca}}$. These plots are shown for five different offsets between the dipole and quadrupole: $S = 0, 30, 60, 90, 120$ nm, with colors from red to blue.

We can then find the maximum value of $\left|\partial|\alpha|^2/\partial x\right|$. At this frequency, the motion transduction will be the strongest. Due to the strong coupling in the good PIT scatterer, the frequency of this maximum value is offset from the center of the dip. In the bad PIT scattering case, the maximum value is also offset due to the detuning $\delta$ included in the model.

Figure 6.16 shows the imprecision calculation for the calculated PIT scatterer. The lowest imprecision found for the good scatterer is 1.5 fm/$\sqrt{\text{Hz}}$ , 3 times larger than the imprecision found for the dimer scatterer discussed in Section 2.5. Interestingly, the maximum sensitivity is not obtained for the quadrupole-offset position $S$ which has the maximum coupling, but a position much closer to the center of the quadrupole antenna. The fact that $S_{\text{good}} \approx 20$ nm is smaller than $S_{\text{bad}} \approx 45$ nm, we attribute to an effective overcoupling in $\kappa$ for the good scatterer.

The transduction method for these PIT antennas is very different from that of

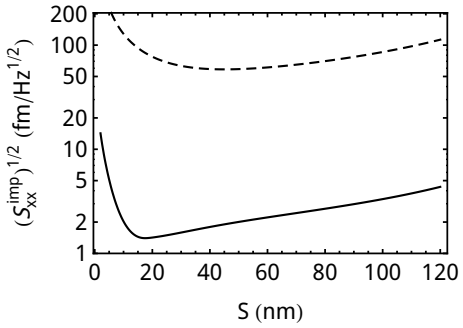


**Figure 6.16:** Imprecision for motion transduction using a PIT scatterer. Noise parameters are as given in Table 2.3. The good scatterer (solid line) uses NA = 1 and polarizer angle $\zeta_{\mathrm{in}} = \zeta_{\mathrm{out}} = 0$. The bad scatterer (dashed line) uses NA = 0.4. and $-\zeta_{\mathrm{in}} = \zeta_{\mathrm{out}} = 0.2\pi$. For both scatterers, the input power $P_{\mathrm{in}} = 500$ μW. As in the dipole-dipole scatterer, shown in Figure 2.14, the good scatterer has a significantly higher sensitivity.

the dipole–dipole antennas. In the latter, the coupling leads to a frequency shift, which we probe on the side of the resonance. For the PIT antennas, the mechanical configuration change also alters the coupling between plasmonic elements, but in this case this leads to a change in the depth of a transparency window.

One important factor to note is that this analysis assumes that the quadrupole antenna does not couple to plane waves, and therefore does not show radiative damping. However, tightly focused fields created by high-NA objectives have higher-order components. Therefore, light tightly focused onto a quadrupole could excite this quadrupole, reducing the PIT effect.

We find that using plasmonically induced transparency in dipole–quadrupole coupled antennas does not offer an immediate boost in sensitivity over the dipole–dipole dimer antennas discussed earlier. However, it is interesting that a completely different scheme can offer very similar sensitivities.

### 6.5.2 Changing dipole–quadrupole detuning

A higher sensitivity can be obtained by changing not the coupling strength $\kappa$ but the frequency detuning $\delta$ between the quadrupole resonance $\Omega_{\mathrm{Q}}$ and the dipole resonance $\Omega_{\mathrm{D}}$. We will investigate the sensitivity obtainable by modulating the quadrupole resonance frequency. We rewrite $\delta$, the detuning between the quadrupole and dipole resonance, as $\delta = \bar{\delta} + G\delta x$, leading to an expression for the quadrupole term in Equation (6.13):

$$\Omega_{\mathrm{Q}} = \omega - \omega_0 + \bar{\delta} + G\delta x + \mathrm{i}\gamma_{\mathrm{Q}}/2. \tag{6.17}$$

Changing the quadrupole resonance frequency has a stronger effect than changing the dipole resonance frequency: the slope in $\mathrm{Im}(\alpha)$ and $|\alpha|^2$ scales not only with

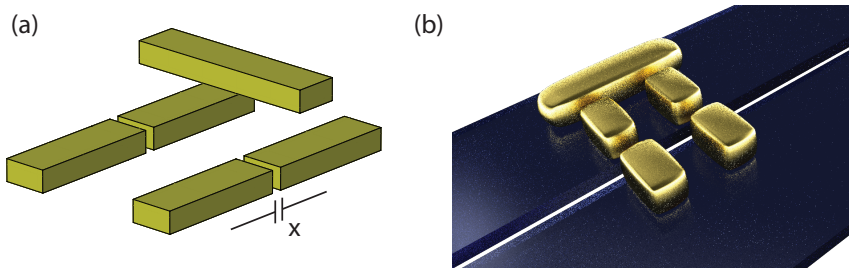


**Figure 6.17:** (a): Sketch of the 5-element plasmonically induced transparency antenna used in this section, indicating gap $x = \bar{x} + \delta x$ between quadrupole elements. All other size parameters are the same as in Figure 6.15, where $L_1$ is the length of one of the quadrupole elements. (b): Artist's impression of possible experimental geometry (image credit: Felipe Bernal).

the frequency shift $G$, but also with the linewidths $\gamma_D$ and $\gamma_Q$. Using the narrow resonance linewidth of the quadrupolar resonance can then boost sensitivity using PIT by a factor proportional to $\gamma_Q/\gamma_D$ over the dipole–dipole coupling shown earlier in this chapter.

To introduce a dependence on mechanical configuration in the quadrupole resonance, we replace the two bars used in the previous section with two pairs of dipole-dipole coupled bars. The two pairs then both have coupling as in the dipole-dipole situation discussed in Chapter 2 and the earlier part of this chapter. A sketch of this geometry is shown in Figure 6.17. We will assume, based on the dipole-dipole calculations shown earlier, $G = 2\pi \times 1$ THz/nm. We can then plot scattering cross sections and change in scattering, using the same parameters as for the 3-element PIT, for a 'good' and 'bad' scatterer. The results are shown in Figure 6.18.

Using the curves plotted in Figure 6.18, we can again determine the optimum frequency for each value of $\delta x$. Using this optimum frequency, we then plot the imprecision for the good and bad 5-element scatterers in Figure 6.19 (black lines). We also plot an equivalent dipole-dipole coupled transducer, by setting $\kappa = 0$ and using the same value for $G$ to change not the quadrupole resonance frequency but the dipole resonance frequency. These imprecisions are plotted as the red lines. We see that for the bad scatterer, the dipole–dipole coupling has lower imprecision. However, for the good scatterer, the dipole-quadrupole shows lower imprecision, with a 10.2 dB reduction in $S_{xx}^{imp}$ relative to the best dipole–dipole imprecision shown in Section 2.6.

Comparing the results to those for the 3-element PIT shown in Figure 6.16, we see that changing the quadrupole resonance improves sensitivity over changing the PIT coupling strength, improving sensitivity by almost an order of magnitude.

We note that it should be fairly straightforward to fabricate such a 5-element scatterer. Using the fabrication technique outlined in Section 3.3, we can fabricate

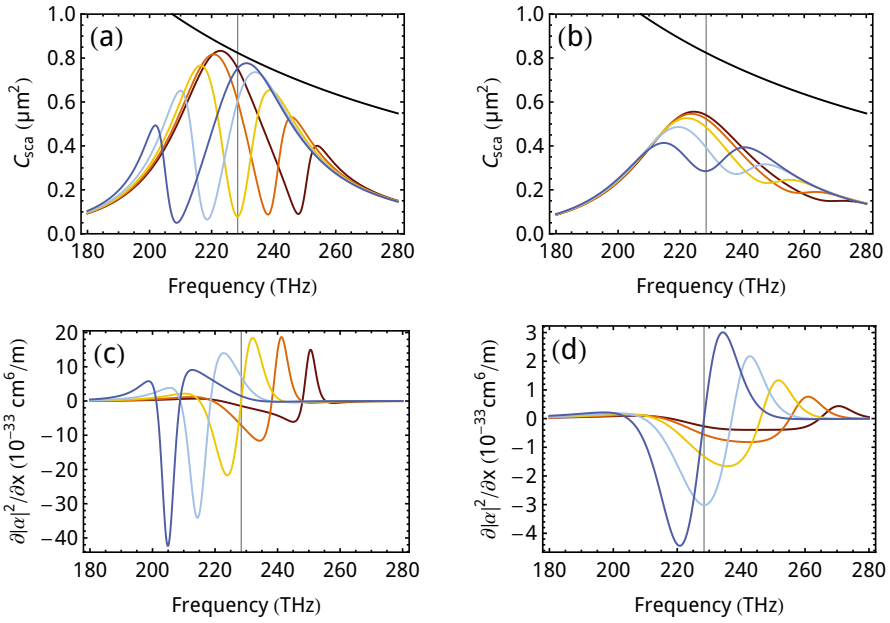


**Figure 6.18:** Scattering and change in scattering for PIT antennas. The left column is for a 'good' PIT scatterer, the right column for a 'bad' PIT scatterer (parameters in main text). Different color curves indicate changing gap between quadrupole elements $x$. Red line: $\delta = -20$ THz, then in 10 THz steps to the blue line with $\delta = 20$ THz.

two double-length rods on a silicon nitride membrane, and then use focused ion beam milling to separate these, creating the quadrupole antenna and releasing the beams. The simplest solution is to redesign the geometry such that the dipole element is placed in the same plane as the quadrupole bars, as was shown by Zhang *et al.* in [150]. This geometry is sketched in Figure 6.17b.

Keeping the geometry studied in this section, the dipole bar can be fabricated by depositing a spacer layer followed by a second EBL step, as outlined by Liu *et al.* [67]. Another possibility might be to fabricate the dipole bar on the other side of the membrane, using the silicon nitride as a spacer layer. This would require careful optimization of the spacings, taking into account the dielectric environment of silicon nitride beams and surrounding gaps.

In this section, we have shown a possible extension to the dipole scattering model introduced in Chapter 2. Using narrow-linewidth quadrupolar resonances can enhance the sensitivity of motion transduction over that of dipole–dipole coupled dimer dipolar resonators, if care is taken to optimize the motion transduction geometry.

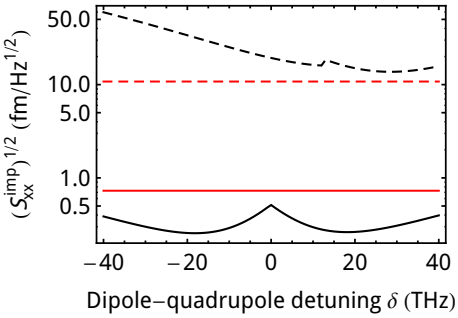


**Figure 6.19:** Imprecision curves for good and bad 5-element PIT scatterers (black lines) and for good and bad dipole–dipole scatterers (red lines). The good scatterers (solid lines) uses $\mathrm{NA} = 1$ and polarizer angle $\zeta_{\mathrm{in}} = \zeta_{\mathrm{out}} = 0$. The bad scatterers (dashed lines) uses $\mathrm{NA} = 0.4$. and $-\zeta_{\mathrm{in}} = \zeta_{\mathrm{out}} = 0.18\pi$. For both scatterers, the input power $P_{\mathrm{in}} = 500$ μW. For the dipole–dipole scatterers, the coupling strength $\kappa = 0$ and the coupling strength $G$ changes $\omega_{\mathrm{D}}$ and not the detuning between the dipolar and quadrupolar resonance. The kink at $x = 0$ for the good scatterer and at $x \approx 20$ nm for the bad scatterer is due to the optimum side-of-PIT-detuning changing from the blue side of the dip to the red side of the dip.

## 6.6 Conclusion

In conclusion, we have for the first time used single plasmonic antennas to probe thermally driven mechanical motion at the nanoscale. Motion was measured with a spectral density of 800 fm/$\sqrt{\mathrm{Hz}}$ , approaching the thermal limit of the resonator, which has a single-sided force sensitivity of 420 aN/$\sqrt{\mathrm{Hz}}$ and a mass sensitivity of 10 fG in a 1 Hz bandwidth.

For further studies, the signal to noise ratio can be improved in various ways. Much higher mechanical quality factors, up to $Q_m \sim 10^6$, have been reported [35, 125] for similar size silicon nitride beams. It is possible that replacing the FIB milling with dry etching of the silicon nitride beams, at the cost of introducing another lithography step, could improve the mechanical quality factor of the beams in our experiment.

The different modes can also have different quality factors: Sun *et al.* [161] discuss how the differential mode of a doubly clamped double beam resonator has a higher $Q$-factor than the common mode, where both beams move in phase, and that the quality factors for both of these modes are higher than those for non-coupled beams, where only one beam is moving.

At present, we are mainly limited by the low albedo of the plasmonic scatterer. Improving this could greatly improve the sensitivity. Then, with a higher albedo, being able to directly measure the scattering properties of the antenna would allow, through fabrication, optimization of the detuning.

We have shown that we can create a plasmonic transducer for mechanical motion, using deeply subwavelength antennas on nanomechanical beams. We studied the effect of antenna length on the transduction of motion. Using a crossed polarizer technique, we increased the sensitivity of the measurement of motion, and by rotating the detected polarization, we were able to quantify the noise components that limit the sensitivity of this technique. The motion transduction calibration was used to derive results for force and mass sensitivity, showing the benefits of the very low effective mass of the oscillators used in this chapter.

Finally, we adapted the transduction model first shown in Chapter 2 to include not only dipole–dipole coupling but also dipole–quadrupole coupling in a plasmonically induced transparency geometry. We show that an optimum dipole–quadrupole scatterer can show lower imprecision than an optimum dipole–dipole scatterer by reducing radiation losses without compromising the optomechanical frequency shift $G$, leading to a calculated 10 dB reduction in imprecision.

Using plasmonic antennas allows the use of a very simple and flexible free-space measurement technique, and the small size of the antennas ($\lambda/3$ in length, $2.5 \times 10^{-4}\lambda^3$ in volume) will allow integration into even smaller mechanical oscillators than we report here.

# References


[1] K. L. Ekinci and M. L. Roukes, *Nanoelectromechanical systems,* Review of Scientific Instruments **76**, 061101 (2005).

[2] M. Li, H. X. Tang, and M. L. Roukes, *Ultra-sensitive NEMS-based cantilevers for sensing, scanned probe and very high-frequency applications,* Nature Nanotechnology **2**, 114 (2007).

[3] H.-A. Bachor and T. C. Ralph, *A Guide to Experiments in Quantum Optics,* Wiley-VCH, $2^d$ edition, 2004.

[4] A. Dorsel, J. D. McCullen, P. Meystre, E. Vignes, and H. Walther, *Optical bistability and mirror confinement induced by radiation pressure,* Physical Review Letters **51**, 1550 (1983).

[5] T. Corbitt, Y. Chen, E. Innerhofer, H. Müller-Ebhardt, D. Ottaway, H. Rehbein, D. Sigg, S. Whitcomb, C. Wipf, and N. Mavalvala, *An all-optical trap for a gram-scale mirror,* Physical Review Letters **98**, 150802 (2007).

[6] B. S. Sheard, M. B. Gray, C. M. Mow-Lowry, D. E. McClelland, and S. E. Whitcomb, *Observation and characterization of an optical spring,* Physical Review A **69**, 051801 (2004).

[7] A. Schliesser, P. Del'Haye, N. Nooshi, K. J. Vahala, and T. J. Kippenberg, *Radiation pressure cooling of a micromechanical oscillator using dynamical backaction,* Physical Review Letters **97**, 243905 (2006).

[8] O. Arcizet, P.-F. Cohadon, T. Briant, M. Pinard, and A. Heidmann, *Radiation-pressure cooling and optomechanical instability of a micromirror,* Nature **444**, 71 (2006).

[9] J. D. Teufel, T. Donner, M. A. Castellanos-Beltran, J. W. Harlow, and K. W. Lehnert, *Nanomechanical motion measured with an imprecision below that at the standard quantum limit,* Nature Nanotechnology **4**, 820 (2009).

[10] J. Chan, T. P. M. Alegre, A. H. Safavi-Naeini, J. T. Hill, A. Krause, S. Gröblacher, M. Aspelmeyer, and O. Painter, *Laser cooling of a nanomechanical oscillator into its quantum ground state,* Nature **478**, 89 (2011).

[11] E. Verhagen, S. Deléglise, S. Weis, A. Schliesser, and T. J. Kippenberg, *Quantum-coherent coupling of a mechanical oscillator to an optical cavity mode,* Nature **482**, 63 (2012).

[12] C. H. Metzger and K. Karrai, *Cavity cooling of a microlever,* Nature **432**, 1002 (2004).

[13] I. Tittonen, G. Breitenbach, T. Kalkbrenner, T. Müller, R. Conradt, S. Schiller, E. Steinsland, N. Blanc, and N. F. de Rooij, *Interferometric measurements of the position of a macroscopic body: Towards observation of quantum limits*, Physical Review A **59**, 1038 (1999).

[14] P. Verlot, A. Tavernarakis, T. Briant, P.-F. Cohadon, and A. Heidmann, *Backaction amplification and quantum limits in optomechanical measurements*, Physical Review Letters **104**, 133602 (2010).

[15] I. Favero, C. Metzger, S. Camerer, D. König, H. Lorenz, J. P. Kotthaus, and K. Karrai, *Optical cooling of a micromirror of wavelength size*, Applied Physics Letters **90**, 104101 (2007).

[16] T. Antoni, A. G. Kuhn, T. Briant, P.-F. Cohadon, A. Heidmann, R. Braive, A. Beveratos, I. Abram, L. Le Gratiet, I. Sagnes, and I. Robert-Philip, *Deformable two-dimensional photonic crystal slab for cavity optomechanics*, Optics Letters **36**, 3434 (2011).

[17] U. Kemiktarak, M. Metcalfe, M. Durand, and J. Lawall, *Mechanically compliant grating reflectors for optomechanics*, Applied Physics Letters **100**, 061124 (2012).

[18] L. Ding, C. Baker, P. Senellart, A. Lemaitre, S. Ducci, G. Leo, and I. Favero, *Wavelength-sized GaAs optomechanical resonators with gigahertz frequency*, Applied Physics Letters **98**, 113108 (2011).

[19] J. Hofer, A. Schliesser, and T. J. Kippenberg, *Cavity optomechanics with ultrahigh-Q crystalline microresonators*, Physical Review A **82**, 031804 (2010).

[20] T. Carmon, H. Rokhsari, L. Yang, T. J. Kippenberg, and K. J. Vahala, *Temporal behavior of radiation-pressure-induced vibrations of an optical microcavity phonon mode*, Physical Review Letters **94**, 223902 (2005).

[21] T. J. Kippenberg, H. Rokhsari, T. Carmon, A. Scherer, and K. J. Vahala, *Analysis of radiation-pressure induced mechanical oscillation of an optical microcavity*, Physical Review Letters **95**, 033901 (2005).

[22] A. Schliesser, R. Riviere, G. Anetsberger, O. Arcizet, and T. J. Kippenberg, *Resolved-sideband cooling of a micromechanical oscillator*, Nature Physics **4**, 415 (2008).

[23] Y.-S. Park and H. Wang, *Resolved-sideband and cryogenic cooling of an optomechanical resonator*, Nature Physics **5**, 489 (2009).

[24] M. Tomes and T. Carmon, *Photonic micro-electromechanical systems vibrating at X-band (11-GHz) rates*, Physical Review Letters **102**, 113601 (2009).

[25] J. D. Thompson, B. M. Zwickl, A. M. Jayich, F. Marquardt, S. M. Girvin, and J. G. E. Harris, *Strong dispersive coupling of a high-finesse cavity to a micromechanical membrane*, Nature **452**, 72 (2008).

[26] A. Xuereb, R. Schnabel, and K. Hammerer, *Dissipative optomechanics in a Michelson-Sagnac interferometer*, Physical Review Letters **107**, 213604 (2011).

[27] I. Favero and K. Karrai, *Optomechanics of deformable optical cavities*, Nature Photonics **3**, 201 (2009).

[28] G. Anetsberger, O. Arcizet, Q. P. Unterreithmeier, R. Rivière, A. Schliesser, E. M. Weig, J. P. Kotthaus, and T. J. Kippenberg, *Near-field cavity optomechanics with nanomechanical oscillators*, Nature Physics **5**, 909 (2009).

[29] X. Jiang, Q. Lin, J. Rosenberg, K. Vahala, and O. Painter, *High-Q double-disk microcavities for cavity optomechanics*, Optics Express **17**, 20911 (2009).

[30] Q. Lin, J. Rosenberg, X. Jiang, K. J. Vahala, and O. Painter, *Mechanical oscillation and*

*cooling actuated by the optical gradient force*, Physical Review Letters **103**, 103601 (2009).

[31] G. S. Wiederhecker, L. Chen, A. Gondarenko, and M. Lipson, *Controlling photonic structures using optical forces*, Nature **462**, 633 (2009).

[32] A. Ashkin and J. M. Dziedzic, *Feedback stabilization of optically levitated particles*, Applied Physics Letters **30**, 202 (1977).

[33] T. Li, S. Kheifets, and M. G. Raizen, *Millikelvin cooling of an optically trapped microsphere in vacuum*, Nature Physics **7**, 527 (2011).

[34] J. Gieseler, B. Deutsch, R. Quidant, and L. Novotny, *Subkelvin parametric feedback cooling of a laser-trapped nanoparticle*, Physical Review Letters **109**, 103603 (2012).

[35] M. Eichenfield, R. Camacho, J. Chan, K. J. Vahala, and O. Painter, *A picogram- and nanometre-scale photonic-crystal optomechanical cavity*, Nature **459**, 550 (2009).

[36] E. Gavartin, R. Braive, I. Sagnes, O. Arcizet, A. Beveratos, T. J. Kippenberg, and I. Robert-Philip, *Optomechanical coupling in a two-dimensional photonic crystal defect cavity*, Physical Review Letters **106**, 203902 (2011).

[37] A. H. Safavi-Naeini and O. Painter, *Design of optomechanical cavities and waveguides on a simultaneous bandgap phononic-photonic crystal slab*, Optics Express **18**, 14926 (2010).

[38] M. Bagheri, M. Poot, M. Li, W. P. H. Pernice, and H. X. Tang, *Dynamic manipulation of nanomechanical resonators in the high-amplitude regime and non-volatile mechanical memory operation*, Nature Nanotechnology **6**, 726 (2011).

[39] M. Li, W. H. P. Pernice, and H. X. Tang, *Broadband all-photonic transduction of nanocantilevers*, Nature Nanotechnology **4**, 377 (2009).

[40] M. Li, W. H. P. Pernice, and H. X. Tang, *Reactive cavity optical force on microdisk-coupled nanomechanical beam waveguides*, Physical Review Letters **103**, 223901 (2009).

[41] W. H. P. Pernice, M. Li, and H. X. Tang, *Gigahertz photothermal effect in silicon waveguides*, Applied Physics Letters **93**, 213106 (2008).

[42] W. H. P. Pernice, M. Li, and H. X. Tang, *Theoretical investigation of the transverse optical force between a silicon nanowire waveguide and a substrate*, Optics Express **17**, 1806 (2009).

[43] H. Raether, *Surface plasmons*, volume 111, Springer, 1988.

[44] P. Drude, *Zur Elektronentheorie der Metalle*, Annalen der Physik **306**, 566 (1900).

[45] C. F. Bohren and D. Huffman, *Absorption and scattering of light by small particles*, Wiley Science Paperback Series, Wiley, 1983.

[46] J. Homola, S. S. Yee, and G. Gauglitz, *Surface plasmon resonance sensors: review*, Sensors and Actuators B: Chemical **54**, 3 (1999).

[47] K. A. Willets and R. P. Van Duyne, *Localized surface plasmon resonance spectroscopy and sensing*, Annual Review of Physical Chemistry **58**, 267 (2007).

[48] J. N. Anker, W. P. Hall, O. Lyandres, N. C. Shah, J. Zhao, and R. P. Van Duyne, *Biosensing with plasmonic nanosensors*, Nature Materials **7**, 442 (2008).

[49] K. M. Mayer and J. H. Hafner, *Localized surface plasmon resonance sensors*, Chemical Reviews **111**, 3828 (2011).

[50] P. Zijlstra and M. Orrit, *Single metal nanoparticles: optical detection, spectroscopy and*

*applications*, Reports on Progress in Physics **74**, 106401 (2011).

[51] H. Yuan, S. Khatua, P. Zijlstra, M. Yorulmaz, and M. Orrit, *Thousand-fold enhancement of single-molecule fluorescence near a single gold nanorod*, Angewandte Chemie International Edition **52**, 1217 (2013).

[52] S. Kim, J. Jin, Y.-J. Kim, I.-Y. Park, Y. Kim, and S.-W. Kim, *High-harmonic generation by resonant plasmon field enhancement*, Nature **453**, 757 (2008).

[53] Z. Fang, Y.-R. Zhen, O. Neumann, A. Polman, F. J. García de Abajo, P. Nordlander, and N. J. Halas, *Evolution of light-induced vapor generation at a liquid-immersed metallic nanoparticle*, Nano Letters **13**, 1736 (2013).

[54] E. C. Garnett, W. Cai, J. J. Cha, F. Mahmood, S. T. Connor, M. Greyson Christoforo, Y. Cui, M. D. McGehee, and M. L. Brongersma, *Self-limited plasmonic welding of silver nanowire junctions*, Nature Materials **11**, 241 (2012).

[55] K. Okamoto and S. Kawata, *Radiation force exerted on subwavelength particles near a nanoaperture*, Physical Review Letters **83**, 4534 (1999).

[56] G. Volpe, R. Quidant, G. Badenes, and D. Petrov, *Surface Plasmon Radiation Forces*, Physical Review Letters **96**, 238101 (2006).

[57] M. Righini, A. S. Zelenina, C. Girard, and R. Quidant, *Parallel and selective trapping in a patterned plasmonic landscape*, Nature Physics **3**, 477 (2007).

[58] A. N. Grigorenko, N. W. Roberts, M. R. Dickinson, and Y. Zhang, *Nanometric optical tweezers based on nanostructured substrates*, Nature Photonics **2**, 365 (2008).

[59] C. Chen, M. L. Juan, Y. Li, G. Maes, G. Borghs, P. Van Dorpe, and R. Quidant, *Enhanced optical trapping and arrangement of nano-objects in a plasmonic nanocavity*, Nano Letters **12**, 125 (2012).

[60] Y. Pang and R. Gordon, *Optical trapping of 12 nm dielectric spheres using double-nanoholes in a gold film*, Nano Letters **11**, 3763 (2011).

[61] N. J. Halas, S. Lal, W.-S. Chang, S. Link, and P. Nordlander, *Plasmons in strongly coupled metallic nanostructures.*, Chemical Reviews **111**, 3913 (2011).

[62] H. T. Miyazaki and Y. Kurokawa, *Squeezing visible light waves into a 3-nm-thick and 55-nm-long plasmon cavity*, Physical Review Letters **96**, 097401 (2006).

[63] S. P. Burgos, R. de Waele, A. Polman, and H. A. Atwater, *A single-layer wide-angle negative-index metamaterial at visible frequencies*, Nature Materials **9**, 407 (2010).

[64] S. Enoch, R. Quidant, and G. Badenes, *Optical sensing based on plasmon coupling in nanoparticle arrays*, Optics Express **12**, 3422 (2004).

[65] T. Atay, J.-H. Song, and A. V. Nurmikko, *Strongly interacting plasmon nanoparticle pairs: from dipole-dipole interaction to conductively coupled regime*, Nano Letters **4**, 1627 (2004).

[66] S. S. Aćimović, M. P. Kreuzer, M. U. González, and R. Quidant, *Plasmon near-field coupling in metal dimers as a step toward single-molecule sensing*, ACS Nano **3**, 1231 (2009), PMID: 19385661.

[67] N. Liu, M. Hentschel, T. Weiss, A. P. Alivisatos, and H. Giessen, *Three-dimensional plasmon rulers*, Science **332**, 1407 (2011).

[68] A. N. Cleland, *Foundations of nanomechanics: from solid-state theory to device applications*, Springer, 2002.

[69] W. Weaver, S. Timoshenko, and D. Young, *Vibration Problems in Engineering*, A Wiley-

Interscience publication, John Wiley & Sons, 1990.

[70] A. Gillespie and F. Raab, *Thermally excited vibrations of the mirrors of laser interferometer gravitational-wave detectors*, Physical Review D **52**, 577 (1995).

[71] M. Pinard, Y. Hadjar, and A. Heidmann, *Effective mass in quantum effects of radiation pressure*, The European Physical Journal D - Atomic, Molecular, Optical and Plasma Physics **7**, 107 (1999).

[72] M. Eichenfield, J. Chan, A. H. Safavi-Naeini, K. J. Vahala, and O. Painter, *Modeling dispersive coupling andlosses of localized optical andmechanical modes in optomechanicalcrystals*, Optics Express **17**, 20078 (2009).

[73] R. B. Karabalin, L. G. Villanueva, M. H. Matheny, J. E. Sader, and M. L. Roukes, *Stress-induced variations in the stiffness of micro- and nanocantilever beams*, Physical Review Letters **108**, 236101 (2012).

[74] Y.-J. Su, C.-F. Qian, M.-H. Zhao, and T.-Y. Zhang, *Microbridge testing of silicon oxide/silicon nitride bilayer films deposited on silicon wafers*, Acta Materialia **48**, 4901 (2000).

[75] S. Bose, S. Schmid, T. Larsen, S. S. Keller, P. Sommer-Larsen, A. Boisen, and K. Almdal, *Micromechanical string resonators: analytical tool for thermal characterization of polymers*, ACS Macro Letters **3**, 55 (2014).

[76] A. A. Clerk, M. H. Devoret, S. M. Girvin, F. Marquardt, and R. J. Schoelkopf, *Introduction to quantum noise, measurement, and amplification*, Reviews of Modern Physics **82**, 1155 (2010).

[77] M. Frimmer, T. Coenen, and A. F. Koenderink, *Signature of a Fano resonance in a plasmonic metamolecule's local density of optical states*, Physical Review Letters **108**, 077404 (2012).

[78] L. Novotny and B. Hecht, *Principles of Nano-Optics*, Cambridge University Press, 2006.

[79] M. Frimmer, *Spontaneous emission near resonant optical antennas*, PhD thesis, University of Amsterdam, 2012.

[80] J. H. Hodak, A. Henglein, and G. V. Hartland, *Coherent excitation of acoustic breathing modes in bimetallic core-shell nanoparticles*, The Journal of Physical Chemistry B **104**, 5053 (2000).

[81] A. L. Tchebotareva, M. A. van Dijk, P. V. Ruijgrok, V. Fokkema, M. H. S. Hesselberth, M. Lippitz, and M. Orrit, *Acoustic and optical modes of single dumbbells of gold nanoparticles*, ChemPhysChem **10**, 111 (2009).

[82] P. Zijlstra, A. L. Tchebotareva, J. W. M. Chon, M. Gu, and M. Orrit, *Acoustic oscillations and elastic moduli of single gold nanorods*, Nano Letters **8**, 3493 (2008).

[83] N. Del Fatti, C. Voisin, F. Chevy, F. Vallée, and C. Flytzanis, *Coherent acoustic mode oscillation and damping in silver nanoparticles*, The Journal of Chemical Physics **110**, 11484 (1999).

[84] P. V. Ruijgrok, P. Zijlstra, A. L. Tchebotareva, and M. Orrit, *Damping of acoustic vibrations of single gold nanoparticles optically trapped in water*, Nano Letters **12**, 1063 (2012).

[85] E. Duval, A. Boukenter, and B. Champagnon, *Vibration eigenmodes and size of microcrystallites in glass: observation by very-low-frequency Raman scattering*, Physical Review Letters **56**, 2052 (1986).

[86] M. Fujii, Y. Kanzawa, S. Hayashi, and K. Yamamoto, *Raman scattering from acoustic*

*phonons confined in Si nanocrystals*, Physical Review B **54**, R8373 (1996).

[87] M. Nisoli, S. De Silvestri, A. Cavalleri, A. M. Malvezzi, A. Stella, G. Lanzani, P. Cheyssac, and R. Kofman, *Coherent acoustic oscillations in metallic nanoparticles generated with femtosecond optical pulses*, Physical Review B **55**, R13424 (1997).

[88] T. D. Krauss and F. W. Wise, *Coherent acoustic phonons in a semiconductor quantum dot*, Physical Review Letters **79**, 5102 (1997).

[89] G. Zumofen, N. M. Mojarad, V. Sandoghdar, and M. Agio, *Perfect reflection of light by an oscillating dipole*, Physical Review Letters **101**, 180404 (2008).

[90] M. Agio, G. Zumofen, N. M. Mojarad, and V. Sandoghdar, *Coupling light to a localized surface plasmon-polariton*, in *Society of Photo-Optical Instrumentation Engineers (SPIE) Conference Series*, volume 7395, 2009.

[91] G. Zumofen, N. M. Mojarad, and M. Agio, *Light scattering by an oscillating dipole in a focused beam*, Nuevo Cimento C **31**, 475 (2009).

[92] N. Mojarad, G. Zumofen, V. Sandoghdar, and M. Agio, *Metal nanoparticles in strongly confined beams: transmission, reflection and absorption*, Journal of the European Optical Society - Rapid publications **4** (2009).

[93] T. C. Zhang, J. P. Poizat, P. Grelu, J. F. Roch, P. Grangier, F. Marin, A. Bramati, V. Jost, M. D. Levenson, and E. Giacobino, *Quantum noise of free-running and externally-stabilized laser diodes*, Quantum and Semiclassical Optics: Journal of the European Optical Society Part B **7**, 601 (1995).

[94] T. J. Kippenberg, A. Schliesser, and M. L. Gorodetsky, *Phase noise measurement of external cavity diode lasers and implications for optomechanical sideband cooling of GHz mechanical modes*, New Journal of Physics **15**, 015019 (2013).

[95] A. H. Safavi-Naeini, J. Chan, J. T. Hill, S. Gröblacher, H. Miao, Y. Chen, M. Aspelmeyer, and O. Painter, *Laser noise in cavity-optomechanical cooling and thermometry*, New Journal of Physics **15**, 035007 (2013).

[96] S. S. Verbridge, J. M. Parpia, R. B. Reichenbach, L. M. Bellan, and H. Craighead, *High quality factor resonance at room temperature with nanostrings under high tensile stress*, Journal of Applied Physics **99**, 124304 (2006).

[97] Y. T. Yang, C. Callegari, X. L. Feng, K. L. Ekinci, and M. L. Roukes, *Zeptogram-scale nanomechanical mass sensing*, Nano Letters **6**, 583 (2006).

[98] D. Karabacak, T. Kouh, C. C. Huang, and K. L. Ekinci, *Optical knife-edge technique for nanomechanical displacement detection*, Applied Physics Letters **88**, (2006).

[99] M. Born and E. Wolf, *Principles of optics: electromagnetic theory of propagation, interference and diffraction of light*, Cambridge University Press, 1999.

[100] M. Aspelmeyer, T. J. Kippenberg, and F. Marquardt, *Cavity optomechanics*, ArXiv e-prints (2013).

[101] J. F. Ziegler, M. Ziegler, and J. Biersack, ***SRIM*** *- The stopping and range of ions in matter (2010)*, Nuclear Instruments and Methods in Physics Research Section B: Beam Interactions with Materials and Atoms **268**, 1818 (2010), 19th International Conference on Ion Beam Analysis.

[102] J. F. Ziegler, *SRIM website: url:* `http://www.srim.org`, 2014.

[103] J. Dionne, L. Sweatlock, H. Atwater, and A. Polman, *Plasmon slot waveguides: Towards chip-scale propagation with subwavelength-scale localization*, Physical Review B **73**, 035407 (2006).

[104] S. B. Hasan, R. Filter, A. Ahmed, R. Vogelgesang, R. Gordon, C. Rockstuhl, and F. Lederer, *Relating localized nanoparticle resonances to an associated antenna problem*, Physical Review B **84**, 195405 (2011).

[105] S. Gröblacher, J. B. Hertzberg, M. R. Vanner, G. D. Cole, S. Gigan, K. C. Schwab, and M. Aspelmeyer, *Demonstration of an ultracold micro-optomechanical oscillator in a cryogenic cavity*, Nature Physics **5**, 485 (2009).

[106] A. H. Safavi-Naeini, J. Chan, J. T. Hill, T. P. M. Alegre, A. Krause, and O. Painter, *Observation of quantum motion of a nanomechanical resonator*, Physical Review Letters **108**, 033602 (2012).

[107] P.-L. Yu, T. P. Purdy, and C. A. Regal, *Control of material damping in high-Q membrane microresonators*, Physical Review Letters **108**, 083603 (2012).

[108] R. Lifshitz, E. Kenig, and M. C. Cross, *Collective dynamics in arrays of coupled nonlinear resonators in "Fluctuating Nonlinear Oscillators"*, chapter 11, Oxford University Press, 2012.

[109] I. Mahboob, M. Mounaix, K. Nishiguchi, A. Fujiwara, and H. Yamaguchi, *A multimode electromechanical parametric resonator array*, Scientific Reports **4**, 4448 (2014).

[110] P. S. Waggoner and H. G. Craighead, *Micro-and nanomechanical sensors for environmental, chemical, and biological detection*, Lab on a Chip **7**, 1238 (2007).

[111] R. Datar, S. Kim, S. Jeon, P. Hesketh, S. Manalis, A. Boisen, and T. Thundat, *Cantilever sensors: nanomechanical tools for diagnostics*, MRS Bulletin **34**, 449 (2009).

[112] J. L. Arlett, E. B. Myers, and M. L. Roukes, *Comparative advantages of mechanical biosensors*, Nature Nanotechnology **6**, 203 (2011).

[113] I. Bargatin, E. B. Myers, J. S. Aldridge, C. Marcoux, P. Brianceau, L. Duraffourg, E. Colinet, S. Hentz, P. Andreucci, and M. L. Roukes, *Large-scale integration of nanoelectromechanical systems for gas sensing applications*, Nano Letters **12**, 1269 (2012).

[114] A. S. Sadek, R. B. Karabalin, J. Du, M. L. Roukes, C. Koch, and S. C. Masmanidis, *Wiring nanoscale biosensors with piezoelectric nanomechanical resonators*, Nano Letters **10**, 1769 (2010).

[115] P. A. Truitt, J. B. Hertzberg, C. C. Huang, K. L. Ekinci, and K. C. Schwab, *Efficient and sensitive capacitive readout of nanomechanical resonator arrays*, Nano Letters **7**, 120 (2007).

[116] M. Yue, J. C. Stachowiak, H. Lin, R. Datar, R. Cote, and A. Majumdar, *Label-free protein recognition two-dimensional array using nanomechanical sensors*, Nano Letters **8**, 520 (2008), PMID: 18179277.

[117] S. C. Jun, X. M. H. Huang, M. Manolidis, C. A. Zorman, M. Mehregany, and J. Hone, *Electrothermal tuning of Al-SiC nanomechanical resonators*, Nanotechnology **17**, 1506 (2006).

[118] T. Larsen, S. Schmid, L. G. Villanueva, and A. Boisen, *Photothermal analysis of individual nanoparticulate samples using micromechanical resonators*, ACS Nano **7**, 6188 (2013).

[119] S. Schmid, K. Wu, P. E. Larsen, T. Rindzevicius, and A. Boisen, *Low-power photothermal probing of single plasmonic nanostructures with nanomechanical string resonators*, Nano Letters **14**, 2318 (2014).

[120] S. Yamada, S. Schmid, T. Larsen, O. Hansen, and A. Boisen, *Photothermal infrared*

*spectroscopy of airborne samples with mechanical string resonators*, Analytical Chemistry **85**, 10531 (2013).

[121] P. Holscher, H.and Milde, U. Zerweck, L. M. Eng, and R. Hoffmann, *The effective quality factor at low temperatures in dynamic force microscopes with Fabry-Pérot interferometer detection*, Applied Physics Letters **94**, 223514 (2009).

[122] K. Usami, A. Naesby, T. Bagci, B. M. Nielsen, J. Liu, S. Stobbe, P. Lodahl, and E. S. Polzik, *Optical cavity cooling of mechanical modes of a semiconductor nanomembrane*, Nature Physics **8**, 168 (2012).

[123] M. Zalalutdinov, A. Zehnder, A. Olkhovets, S. Turner, L. Sekaric, D. Ilic, B.and Czaplewski, J. M. Parpia, and H. G. Craighead, *Autoparametric optical drive for micromechanical oscillators*, Applied Physics Letters **79**, 695 (2001).

[124] C. Metzger, M. Ludwig, C. Neuenhahn, A. Ortlieb, I. Favero, K. Karrai, and F. Marquardt, *Self-induced oscillations in an optomechanical system driven by bolometric backaction*, Physical Review Letters **101**, 133903 (2008).

[125] S. Schmid, K. D. Jensen, K. H. Nielsen, and A. Boisen, *Damping mechanisms in high-Q micro and nanomechanical string resonators*, Physical Review B **84**, 165307 (2011).

[126] K. Yasumura, T. Stowe, E. Chow, T. Pfafman, T. Kenny, B. Stipe, and D. Rugar, *Quality factors in micron- and submicron-thick cantilevers*, Journal of Microelectromechanical Systems **9**, 117 (2000).

[127] P. Mohanty, D. A. Harrington, K. L. Ekinci, Y. T. Yang, M. J. Murphy, and M. L. Roukes, *Intrinsic dissipation in high-frequency micromechanical resonators*, Physical Review B **66**, 085416 (2002).

[128] W. A. Phillips, *Two-level states in glasses*, Reports on Progress in Physics **50**, 1657 (1987).

[129] L. G. Remus, M. P. Blencowe, and Y. Tanaka, *Damping and decoherence of a nanomechanical resonator due to a few two-level systems*, Physical Review B **80**, 174103 (2009).

[130] Y. Tsaturyan, A. Barg, A. Simonsen, L. G. Villanueva, S. Schmid, A. Schliesser, and E. S. Polzik, *Demonstration of suppressed phonon tunneling losses in phononic bandgap shielded membrane resonators for high-Q optomechanics*, Optics Express **22**, 6810 (2014).

[131] P.-L. Yu, K. Cicak, N. S. Kampel, Y. Tsaturyan, T. P. Purdy, R. W. Simmonds, and C. A. Regal, *A phononic bandgap shield for high-Q membrane microresonators*, Applied Physics Letters **104**, (2014).

[132] M. Sato, B. E. Hubbard, A. J. Sievers, B. Ilic, D. A. Czaplewski, and H. G. Craighead, *Observation of locked intrinsic localized vibrational modes in a micromechanical oscillator array*, Physical Review Letters **90**, 044102 (2003).

[133] M. Spletzer, A. Raman, H. Sumali, and J. P. Sullivan, *Highly sensitive mass detection and identification using vibration localization in coupled microcantilever arrays*, Applied Physics Letters **92**, (2008).

[134] D. Galayko, A. Kaiser, B. Legrand, L. Buchaillot, C. Combi, and D. Collard, *Coupled-resonator micromechanical filters with voltage tuneable bandpass characteristic in thick-film polysilicon technology*, Sensors and Actuators A: Physical **126**, 227 (2006).

[135] C.-C. Nguyen, *MEMS technology for timing and frequency control*, IEEE Transactions on Ultrasonics, Ferroelectrics and Frequency Control **54**, 251 (2007).

[136] B. E. DeMartini, J. F. Rhoads, M. A. Zielke, K. G. Owen, S. W. Shaw, and K. L. Turner, *A single input-single output coupled microresonator array for the detection and identification of multiple analytes*, Applied Physics Letters **93**, (2008).

[137] S.-B. Shim, M. Imboden, and P. Mohanty, *Synchronized oscillation in coupled nanomechanical oscillators*, Science **316**, 95 (2007).

[138] E. Buks and M. L. Roukes, *Electrically tunable collective response in a coupled micromechanical array*, Journal of Microelectromechanical Systems **11**, 802 (2002).

[139] H. Okamoto, A. Gourgout, C.-Y. Chang, K. Onomitsu, I. Mahboob, E. Y. Chang, and H. Yamaguchi, *Coherent phonon manipulation in coupled mechanical resonators*, Nature Physics **9**, 480 (2013).

[140] S. Zou and G. C. Schatz, *Narrow plasmonic/photonic extinction and scattering line shapes for one and two dimensional silver nanoparticle arrays*, The Journal of Chemical Physics **121**, 12606 (2004).

[141] E. M. Hicks, S. Zou, G. C. Schatz, K. G. Spears, R. P. Van Duyne, L. Gunnarsson, T. Rindzevicius, B. Kasemo, and M. Käll, *Controlling plasmon line shapes through diffractive coupling in linear arrays of cylindrical nanoparticles fabricated by electron beam lithography*, Nano Letters **5**, 1065 (2005).

[142] K. Y. Fong, W. H. P. Pernice, M. Li, and H. X. Tang, *High Q optomechanical resonators in silicon nitride nanophotonic circuits*, Applied Physics Letters **97**, (2010).

[143] M. L. Gorodetsky, A. Schliesser, G. Anetsberger, S. Deleglise, and T. J. Kippenberg, *Determination of the vacuum optomechanical coupling rate using frequency noise calibration*, Optics Express **18**, 23236 (2010).

[144] D. Smith, *Limits of force microscopy*, Review of Scientific Instruments **66**, 3191 (1995).

[145] H. J. Mamin and D. Rugar, *Sub-attonewton force detection at millikelvin temperatures*, Applied Physics Letters **79**, 3358 (2001).

[146] E. Gavartin, P. Verlot, and T. J. Kippenberg, *A hybrid on-chip optomechanical transducer for ultrasensitive force measurements*, Nature Nanotechnology **7**, 509 (2012).

[147] K. L. Ekinci, Y. T. Yang, and M. L. Roukes, *Ultimate limits to inertial mass sensing based upon nanoelectromechanical systems*, Journal of Applied Physics **95**, 2682 (2004).

[148] J. Chaste, A. Eichler, J. Moser, G. Ceballos, R. Rurali, and A. Bachtold, *A nanomechanical mass sensor with yoctogram resolution*, Nature Nanotechnology **7**, 301 (2012).

[149] M. Hentschel, D. Dregely, R. Vogelgesang, H. Giessen, and N. Liu, *Plasmonic oligomers: The role of individual particles in collective behavior*, ACS Nano **5**, 2042 (2011).

[150] S. Zhang, D. A. Genov, Y. Wang, M. Liu, and X. Zhang, *Plasmon-induced transparency in metamaterials*, Physical Review Letters **101**, 047401 (2008).

[151] N. Verellen, Y. Sonnefraud, H. Sobhani, F. Hao, V. V. Moshchalkov, P. Van Dorpe, P. Nordlander, and S. A. Maier, *Fano resonances in individual coherent plasmonic nanocavities*, Nano Letters **9**, 1663 (2009).

[152] N. Liu, L. Langguth, T. Weiss, J. Kästel, M. Fleischhauer, T. Pfau, and H. Giessen, *Plasmonic analogue of electromagnetically induced transparency at the Drude damping limit*, Nature Materials **8**, 758 (2009).

[153] N. Liu, T. Weiss, M. Mesch, L. Langguth, U. Eigenthaler, M. Hirscher, C. Sönnichsen, and H. Giessen, *Planar metamaterial analogue of electromagnetically induced transparency for plasmonic sensing*, Nano Letters **10**, 1103 (2010).

[154] S. N. Sheikholeslami, A. Garcia-Extarri, and J. A. Dionne, *Controlling the interplay of electric and magnetic modes via Fano-like plasmon resonances*, Nano Letters **11**, 3927 (2011).

[155] W. S. Chang, J. B. Lassiter, P. Swanglap, H. Sobhani, S. Khatua, P. Nordlander, N. J. Halas, and S. Link, *A plasmonic Fano switch*, Nano Letters **12**, 4977 (2012).

[156] R. Hokari, Y. Kanamori, and K. Hane, *Comparison of electromagnetically induced transparency between silver, gold, and aluminum metamaterials at visible wavelengths*, Optics Express **22**, 3526 (2014).

[157] Z. Ye, S. Zhang, Y. Wang, Y. Park, T. Zentgraf, G. Bartal, X. Yin, and X. Zhang, *Mapping the near-field dynamics in plasmon-induced transparency*, Physical Review B **86**, 155148 (2012).

[158] C. Forestiere, L. Dal Negro, and G. Miano, *Theory of coupled plasmon modes and Fano-like resonances in subwavelength metal structures*, Physical Review B **88**, 155411 (2013).

[159] M. Fleischhauer, A. Imamoglu, and J. P. Marangos, *Electromagnetically induced transparency: Optics in coherent media*, Reviews of Modern Physics **77**, 633 (2005).

[160] R. Taubert, M. Hentschel, and H. Giessen, *Plasmonic analog of electromagnetically induced absorption: simulations, experiments, and coupled oscillator analysis*, Journal of the Optical Society of America B **30**, 3123 (2013).

[161] X. Sun, J. Zheng, M. Poot, C. W. Wong, and H. X. Tang, *Femtogram doubly clamped nanomechanical resonators embedded in a high-q two-dimensional photonic crystal nanocavity*, Nano Letters **12**, 2299 (2012).

# Summary

In this thesis, we investigate the interaction between light, confined to the nanoscale in the form of surface plasmon polaritons, and the motion of micro- and nanomechanical oscillators. Taken together, these form plasmonic optomechanical systems. The strong field confinement and local field enhancement around plasmonic antennas make them extremely sensitive transducers of mechanical motion to scattered optical fields. Due to the strong field gradients in the plasmonic near field the optomechanical coupling constant $G \equiv \frac{\partial \omega_c}{\partial x}$ can exceed 1 THz/nm, which is well beyond that of other existing mechanical transduction geometries.

Another advantage of plasmonic antennas is that they are addressable from free space. This, together with the high $G$'s that are attainable, makes a plasmonic motion transducer very simple: focused light from a lens can be used to excite the resonance, and the high $G$ obviates the need for a Fabry-Pérot cavity to boost sensitivity, while the limited optical quality factor implies a high optical bandwidth, eliminating the need for complex schemes to stabilize the laser to the optical resonance. The high overlap between the plasmonic mode and the mechanical mode, which is responsible for the high coupling strength, also allows integrated measurements on truly nanoscale resonators. Finally, the small size and free-space addressability of plasmonic antennas allows parallel transduction of multiple mechanical oscillators with a single laser beam.

In Chapter 2, we develop a theoretical framework for analyzing plasmonic optomechanics. We first derive expressions for the eigenfrequencies and thermal occupation of doubly clamped nanobeams. We give expressions for these occupations in terms of spectral densities. Next, we calculate coupling rates for spherical metallic nanoparticles, showing that strong coupling is achievable, and derive the radiative loss rate. To measure the motion of individual nanobeams, we will place plasmonic particles on these beams. Addressing these plasmonic resonators optically will require tightly confined optical fields. We therefore incorporate focusing in our model, and show how a dipolar scatterer placed at this focus will modulate the transmittance, defining the transmittance in terms of the numerical aperture of the focusing lens and the polarizability $\alpha$ of the scatterer.

To suppress the contribution of directly transmitted light (that has not interacted with the scatterer) relative to the scattered and extincted contributions, we expand the equations for transmittance to allow different angles for input polarization and output analyzer relative to the scatterer.

A transmittance measurement will not only include modulation due to the mechanical modulation of the beams supporting the antenna, but also various noise contributions. We calculate the strength of these noise contributions, and express them as contributions to the displacement imprecision. Next, we show the resulting imprecision for several plasmonic scatterers. We also model the transmittance of these scatterers when applied to several mechanical resonators that have been shown in the literature.

Chapter 3 describes the vacuum microscopy setup we developed to measure plasmonic nanomechanical transduction. We also describe the fabrication methods used to create plasmonic antennas on nanomechanical structures, using a combination of metal deposition, electron-beam lithography and focused ion beam milling.

In Chapter 4, we describe a plasmonic transducer consisting of two gold-coated silicon nitride beams. The narrow gold-coated slot between the two beams creates a very short (100 nm length) metal-insulator-metal waveguide. The index mismatch between this waveguide and the surrounding vacuum creates a Fabry-Pérot cavity, introducing resonances. The resonance frequency of this MIM cavity is dependent on the spacing between the beams. We show how this system transduces motion, measuring motion with an imprecision $S_{xx}^{imp} = 40\ \mathrm{fm}/\sqrt{\mathrm{Hz}}$ . The metal covering of the beams greatly reduces direct transmission of light, effectively forming a darkfield geometry, which improves the measurement sensitivity. Finally, we discuss the effects of input polarization, ambient pressure, and the length of the beams on the sensitivity of the measurement.

Chapter 5 demonstrates how the transduction scheme shown in Chapter 4 can be used to read out the motion of multiple beams, arranged in parallel arrays of beams. In these parallel arrays, the motion of each beam is transduced by the slots on either side of the beam. Parallel measurement of the motion of all 8 nanomechanical beams is obtained by tuning the width of the plasmonic slots. As the metal also absorbs light, the beams are heated. This heating changes the mechanical properties of the beams, which can be used to tune the resonance frequencies of the beams. This can then be used to tune the resonance frequency of different beams to match, leading to mechanical coupling between the beams mediated by the substrate, which appears as avoided crossings in the thermally tuned spectra. When studying the out-of-plane mechanical mode, the heating causes a bilayer thermal stress in the beams. At high enough input powers, this leads to parametric amplification of the out-of-plane motion of the beams. Finally, we show that by reducing the metal coverage of the beams, we can improve the mechanical quality factor of the beams from 500–1000 up to 7000.

In Chapter 6, we introduce a plasmonic resonator with extremely small plasmonic modal volume: an antenna consisting of two dipole-dipole coupled gold

bars. We place each element of this antenna on an individual silicon nitride beam (10.5 μm × 120 nm × 100 nm), obtaining a low effective mass of 160 fg. Due to low scattering, we use crossed polarizers to measure the mechanical transduction of this plasmonic antenna with 800 fm/$\sqrt{\text{Hz}}$ imprecision. We discuss force and mass sensing using this platform, finding that the low effective mass makes this a sensitive geometry, with a force sensitivity of 420 aN/$\sqrt{\text{Hz}}$ and a mass sensitivity of 10 fg/$\sqrt{\text{Hz}}$. Finally, we model the use of a dipole–quadrupole coupled antenna, where we use the narrow quadrupolar linewidth in a scatterer showing plasmonically induced transparency to improve sensitivity.

To conclude, we have shown that plasmonic nanostructures can be used to transduce thermally driven nanomechanical motion to optical signals. Plasmonic antennas show very high coupling rates, combined with small physical sizes and sub-wavelength mode volumes. These properties make plasmonics an interesting platform for motion transduction, allowing free space coupling and parallel transduction of nanoscale mechanical motion.

# Samenvatting

Dit proefschrift onderzoekt de interactie tussen licht, gevangen op de nanoschaal in de vorm van oppervlakteplasmonpolaritonen, en de beweging van micro- en nanomechanische oscillatoren. De grote veldconcentratie en lokale veldversterking vlakbij plasmonische antennes zorgen er voor dat deze antennes ultragevoelig mechanische beweging om kunnen zetten in (verstrooide) lichtvelden. Als gevolg van de sterke veldgradiënten in het nabije veld van een plasmonische antenne is de optomechanische koppelingsconstante $G \equiv \frac{\partial \omega_c}{\partial x}$ (de frequentieverschuiving van de optische resonantie per eenheid van verplaatsing) groter dan 1 THz/nm, wat veel groter is dan die van alle tot nog toe bekende optomechanische transductiegeometrieën.

Een ander voordeel van plasmonische antennes is dat ze vanuit het verre veld met een lichtbundel aangeslagen kunnen worden. Dit maakt, samen met de grote $G$-waardes die bereikt kunnen worden, dat een plasmonische bewegingssensor een relatief simpel ontwerp kan hebben. Licht kan met een lens op de antenne gefocusseerd worden en door de hoge $G$ is er geen Fabry-Pérot etalon nodig om de gevoeligheid te vergroten. Omdat een plasmonische resonantie een grote lijnbreedte heeft, is de intrinsieke frequentiestabiliteit van de lasers die we gebruiken groot genoeg om de lasers niet actief aan de resonantie te hoeven stabiliseren. De combinatie van kleine afmetingen en vrije-veld excitatie maken het mogelijk om met een enkele laserbundel de beweging van meerdere mechanische oscillatoren parallel uit te lezen.

In hoofdstuk 2 wordt een theoretisch raamwerk voor plasmonische optomechanica afgeleid. Als eerste worden uitdrukkingen voor de eigenfrequenties van nanobruggen en hun beweging ten gevolge van de stochastische Langevin-kracht afgeleid. Vervolgens berekenen we de koppelingssterktes voor bolvormige metalen nanodeeltjes in de dipolaire limiet, waarbij we laten zien dat sterke koppeling mogelijk is, en bepalen we de grootte van de stralingsdemping. Om de beweging van nanobruggen uit te lezen, hebben we plasmonische antennes op deze bruggen geplaatst. Het uitlezen van deze antennes vereist sterk gefocusseerd licht. We rekenen de elektrische veldsterkte in het focus van een microscoopobjectief uit en laten zien hoe een dipolaire verstrooier in dit focus de transmissie van licht beinvloedt,

waarbij we de doorlaatbaarheid uitdrukken als functie van de openingshoek van de focusserende lens en de polariseerbaarheid $\alpha$ van de verstrooier.

Om de hoeveelheid rechtstreeks doorgelaten licht (dat dus geen interactie met de verstrooier heeft gehad) te verminderen, kan een polarisatiefilter voor de detector geplaatst worden. Om het effect hiervan te bepalen, brengen we in de analyse ook de polarizatiehoek van het licht in rekening, om verschillende ingangs- en uitgangspolarisaties mogelijk te maken.

Een dergelijke verstrooiingsmeting zal niet alleen modulatiecomponenten bevatten ten gevolge van de mechanische modulatie van de nanobruggen waar de antenne op rust, maar ook modulaties ten gevolge van een aantal verschillende bronnen van optische en elektrische ruis. We rekenen de relatieve sterkte van deze componenten uit en drukken deze uit als meetimprecisies. Als laatste berekenen we de totale meetimprecisie voor een aantal mogelijke strukturen, gebruikmakend van zowel berekende lijnbreedtes en koppelingsconstantes voor verschillende plasmonische verstrooiers als van verschillende literatuurwaardes voor nanomechanische resonatoren.

In hoofdstuk 3 beschrijven we de vacuümmicroscoop die we op AMOLF ontwikkeld hebben om plasmonische nanomechanische resonatoren uit te lezen. Vervolgens beschrijven we ook een aantal fabricagemethodes die we gebruiken om de structuren te maken. Hierbij maken we gebruik van metaaldepositie, elektronenbundel-lithografie en gefocusseerde-ionenbundel frezen.

Hoofdstuk 4 omschrijft een plasmonische sensor die bestaat uit twee met goud bedekte nanobruggen van siliciumnitride. De smalle spleet tussen de twee goudlagen vormt een zeer korte (100 nm) metaal-diëlectricum-metaal (MIM) golfgeleider. Deze vormt een Fabry-Pérot trilholte, waardoor resonanties onstaan. De resonantiefrequentie van deze MIM-holte hangt af van de afstand tussen de bruggen. We laten zien hoe dit systeem thermisch aangedreven beweging van de bruggen detecteert met een meetimprecisie van $S_{xx}^{imp} = 40\ \mathrm{fm}/\sqrt{\mathrm{Hz}}$ . Omdat de bruggen volledig met goud bedekt zijn, is al het licht dat we in transmissie detecteren door de MIM-holte geperst. Dit betekent dat er geen achtergrondsignaal is, wat de gevoeligheid verbetert. Als laatste bespreekt dit hoofdstuk de effecten van de omgevingsdruk, de lengte van de bruggen en van veranderingen in de polarisatie van het inkomende licht op de amplitude van het signaal.

In hoofdstuk 5 demonstreren we hoe het in hoofdstuk 4 beschreven mechanisme gebruikt kan worden om de beweging van vele bruggen parallel uit te lezen. We maken reeksen van parallele bruggen, waarin de beweging van elke brug door de twee spleten aan weerszijden van elke brug wordt omgezet in modulaties in het doorgelaten licht. Als de spleten precies even groot zijn, hebben ze exact dezelfde gevoeligheid. Beweging in het vlak wordt dan niet gedetecteerd: als de ene spleet breder wordt, wordt de andere precies evenveel kleiner en verdwijnt de netto gevoeligheid. Door de breedte van de spleten zorgvuldig te veranderen kan de beweging van de 8 bruggen wèl parallel uitgelezen worden.

Omdat het metaal op de bruggen ook licht absorbeert, warmen de bruggen op, waardoor de mechanische eigenschappen van de bruggen veranderen. Met

dit effect kunnen de resonanties van de verschillende bruggen verstemd worden. Als we twee naast elkaar gelegen bruggen naar dezelfde frequentie verstemmen, zien we de mechanische koppeling tussen de bruggen, die door het substraat loopt, optreden als een 'avoided crossing'. De bruggen hebben ook een mechanische trilling uit het vlak. Omdat goud en siliciumnitride verschillende thermische uitzettingscoëfficienten hebben, levert een opwarming een buigspanning uit het vlak op. Wanneer er genoeg licht geabsorbeerd wordt, kan de uit-het-vlak beweging parametrisch versterkt worden, wat leidt tot zeer grote bewegingsamplitudes. Ten slotte laten we zien dat we door bruggen te maken met alleen goud in het midden van de brug, de mechanische kwaliteitsfactor $Q$ toeneemt van 500–1000 tot ongeveer 7000.

In hoofdstuk 6 maken we de kleinst mogelijke plasmonische bewegingssensor, bestaande uit twee dipool–dipool gekoppelde gouden staafjes, met een totale lengte van 485 nanometer. Elk van deze staafjes plaatsen we op een losse siliciumnitride brug (10,5 micrometer lang, met een doorsnede van $100 \times 120$ nanometer), wat leidt tot een effectieve massa van 160 femtogram. Omdat de verstrooiing van deze antenne heel laag is, gebruiken we twee gekruiste polarisatiefilters om de mechanische transductie te meten, waarbij we een imprecisie van 800 fm/$\sqrt{\text{Hz}}$ bereiken. Omdat de massa van het systeem zo laag is, kan de sensor gebruikt worden om krachten te meten met een gevoeligheid van 420 aN/$\sqrt{\text{Hz}}$ en veranderingen in massa met een gevoeligheid van 10 fg/$\sqrt{\text{Hz}}$. Ten slotte berekenen we de gevoeligheid die bereikt zou kunnen worden met dipool–quadrupool antennes. Omdat een quadrupoolantenne een veel lagere stralingsdemping heeft, heeft deze een smallere lijnbreedte. We berekenen dan dat door de resonanties van de dipool- en quadrupoolantennes zorgvuldig af te stemmen 'plasmon-geïnduceerde-transparantie' optreedt. Door nu de resonantiefrequentie van de quadrupoolantenne geometrie-afhankelijk te maken, berekenen we een lagere imprecisie voor het dipool–quadrupool systeem dan voor het dipool–dipool systeem.

Dit proefschrift laat zien dat oppervlakteplasmonpolaritonen gebruikt kunnen worden om thermisch aangedreven nanomechanische beweging te detecteren. De sterke koppeling, kleine fysieke afmetingen en sub-golflengte modevolumes maken plasmonen een interessant platform voor transductie van beweging, met eenvoudige uitlezing en de mogelijkheid tot het parallel uitlezen van meerdere oscillatoren.

# List of publications

This thesis is based on the following publications:

- *Dipolar scattering for motion transduction*, R. Thijssen, T. J. Kippenberg, A. Polman, and E. Verhagen, *in preparation.* **(Chapter 2, § 2.3–2.6 and Chapter 6, § 6.5)**
- *Plasmon nanomechanical coupling for nanoscale transduction*, R. Thijssen, E. Verhagen, T. J. Kippenberg, and A. Polman, Nano Letters **13**, 3293–3297 (2013). **(Chapter 4)**
- *Parallel transduction of nanomechanical motion using plasmonic resonators*, R. Thijssen, T. J. Kippenberg, A. Polman, and E. Verhagen, *submitted.* **(Chapter 5)**
- *Plasmonic dimer antenna nano-optomechanical transducers*, R. Thijssen, T. J. Kippenberg, A. Polman, and E. Verhagen, *in preparation.* **(Chapter 6)**

Other publications by the author:

- *Spatially resolved excitation of Rydberg atoms and surface effects on an atom chip*, Atreju Tauschinsky, Rutger M. T. Thijssen, S. Whitlock, H. B. van Linden van den Heuvell, and R. J. C. Spreeuw, Physical Review A, **81**, 063411 (2010).
- *Localized excitation of antennas on waveguides*, F. Bernal, R. Thijssen, B. Brenny, T. Coenen, A. Polman, and A. F. Koenderink, *in preparation.*

# Acknowledgements

Ruim vier jaar heb ik aan dit proefschrift gewerkt. Het volbrengen van mijn promotieonderzoek, van allereerste concept tot en met het drukken van een boek, was niet mogelijk geweest zonder de hulp van een grote groep mensen. Die wil ik hier graag danken voor hun steun en hulp.

Allereerst zijn daar natuurlijk mijn promotor en copromotores. Albert, ik heb veel van je geleerd, en je vertrouwen en optimisme waren belangrijk voor dit project. Naast de directe begeleiding heb ik veel geleerd van de mogelijkheden om onder jouw leiding andere onderzoeksinstellingen in Europa en de VS te zien, en om met allerlei onderzoeksgroepen in contact te komen. Tobias, allereerst natuurlijk mijn dank dat je samen met Albert op het idee kwam om jullie vakgebieden, de optomechanica en de plasmonica, te combineren. Zonder die avond in München had dit boek hier niet gelegen. Verder stond je, hoewel 1000 kilometer verder, altijd klaar met inzichten en reviews van manuscripten. Ewold, zonder jou hulp de laatste twee jaar van mijn onderzoek was dit proefschrift een stuk dunner geweest. Ik wil je graag danken voor je hulp, zowel bij fundamentele inzichten over de natuurkunde als bij concrete problemen in het lab.

Ik heb veel gehad aan mijn collegas in de Photonic Materials groep. In the first year of my research, Robb and James helped me find my way in the lab and the cleanroom. Ernst Jan, Pierpaolo, Toon, Claire, Ruben, Jorik, Marie Anne, Benjamin, Bonna, Julia, and Mark, thanks for all the discussion, help and company over the course of the last four years. Petra en Karelia, dank voor jullie secretariële ondersteuning. Bas, het was een bijzonder leuke ervaring jouw afstudeeronderzoek te mogen begeleiden.

De afgelopen twee jaar is Ewold bezig geweest met het opstarten van de Photonic Forces groep, waardoor het aantal optomechanici op AMOLF sterk is toegenomen. Rick, Freek, Hugo, Ruud, Aloys, het was me een genoegen om met jullie samen te werken, en ik wens jullie veel succes met jullie projecten.

Eén van de redenen dat het werken op AMOLF nooit eenzaam was is de grote mate van interactie met de overige leden van het Center for Nanophotonics. Ik wil jullie dan ook allemaal danken voor de discussies, zowel bij de koffie als bij de colloquia en postersessies.

Zonder een grote hoeveelheid technische ondersteuning was dit project niet mogelijk geweest. Als eerste wil ik graag Hans, Dimitri, Andries en Johan noemen voor het mogelijk maken van een geweldige cleanroom en elektronenmicroscopielab, waardoor het maken van mijn experimentele structuren mogelijk werd.

Het maken van meetsamples was één aspect van mijn projekt, maar zonder een meetopstelling heb je daar weinig aan. Iliya heeft een prachtige vacuümkamer ontworpen, die vervolgens door Ricardo en Wim uit een massief blok aluminium gefreesd is. Ik ben nog altijd diep onder de indruk van jullie vakmanschap.

Ik wil graag Femius en Marko danken voor het gebruik van de FTIR-microscoop waarmee een deel van de metingen in hoofdstuk 6 uitgevoerd zijn.

Duncan, Idsart, Sjoerd, en Luc hebben me geholpen met allerhande elektronica: het uitzoeken van spectrum analyzers, het solderen van vacuumdoorvoeren, hulp bij het schrijven van LabView-software en nog vele andere kleine dingen.

Wiebe en Jan hebben een schier oneindige reeks COMSOL-updates geïnstalleerd, waarvoor mijn dank, en samen met de hele ICT-afdeling ervoor gezorgd dat lab-, bureau- en rekencomputers altijd werkten.

Tatiana en Andre stonden in het magazijn altijd klaar om bestellingen uit te voeren, leveranciers na te bellen, en om zo nu en dan eens een pakketje naar de VS te versturen.

Bij kleine en minder kleine problemen in het lab waren Hinco, Tarik, Iliya, Hans en Wim altijd bereid om te helpen, wat het werken een stuk makkelijker heeft gemaakt.

Ook op grafisch gebied heb ik dankbaar gebruik gemaakt van de kunde van anderen: AMOLF's huisfotograaf Henk-Jan voor de foto's in hoofdstuk 3, mijn moeder Anneke voor foto's in hoodstuk 3 en bij het CV achterin dit proefschrift, en mijn broer Barthold voor de renders van dubbele bruggen in hoofdstuk 4, en natuurlijk voor al zijn werk aan de omslag van dit boek.

En dan zijn er nog de uren buiten AMOLF. Erik, Ernst Jan, Bart: dank voor de gezelligheid op C-386. Ik heb veel gehad aan het 'buitenspelen' op Nereus; een stuk langs de Amstel fietsen geeft een hoop ruimte, dus mijn dank aan mijn medecoaches en alle roeiers die ik heb mogen coachen. Als laatste wil ik mijn ouders en mijn broers Barthold en Steven danken voor hun onvoorwaardelijke steun. I couldn't have done it without you.

# About the author

Rutger Thijssen was born in New York City on July 9, 1984. He received his high school diploma from the 'Gemeentelijk Gymnasium' in Hilversum in 2001. After studying history at the University of Durham for one year, he studied physics and astronomy at the University of Amsterdam, graduating with a thesis on electromagnetically induced transparency in ultracold rubidium gas under the supervision of dr. Robert Spreeuw. In 2010, he started a PhD project at the FOM Institute AMOLF, in the group of prof. dr. Albert Polman, co-supervised by prof. dr. T. J. Kippenberg and dr. E. Verhagen, studying plasmonic antennas and their utilization as transducers of nanoscale motion. When he isn't at AMOLF, Rutger enjoys sailing, rowing and bicycling.


The work described in this thesis was performed at the FOM-Institute AMOLF, Science Park 104, 1098 XG Amsterdam, The Netherlands.